ANNUAL REPORT 2005

Optoelectronics Department

UNIVERSITÄT ULM · SCIENDO · DOCENDO · CURANDO

University of Ulm

Contents

1:	Abdel-Sattar Gadallah	2:	Hendrik Roscher	3:	Sükran Kilic
4:	Steffen Lorch	5:	Peter Unger	6:	Michael C. Riedl
7:	Ferdinand Scholz	8:	Jürgen Mähnß	9:	Hildegard Mack
10:	Josef Theisz	11:	Gerlinde Meixner	12:	Rudolf Rösch
13:	Philipp Gerlach	14:	Barbara Neubert	15:	Frank Demaria
16:	Andrea Kroner	17:	Wolfgang Schwarz	18:	Rainer Michalzik
19:	Peter Brückner	20:	Joachim Hertkorn	21:	Fernando Rinaldi
22:	Martin Stach	23:	Christine Bunk	24:	Georgi Stareev
25:	Sarad B. Thapa				

Missing in the picture

26:	Rainer Blood	27:	Karl J. Ebeling	28:	Daniel Hofstetter
29:	Ihab Kardosh	30:	Susanne Menzel	31:	Johannes M. Ostermann

Optoelectronics Department University of Ulm

Albert-Einstein-Allee 45, D-89081 Ulm, Germany
URL: http://www-opto.e-technik.uni-ulm.de
Fax: +49–731/50–2 60 49
Phone: +49–731/50–

Head of Department			
Prof. Dr.	Peter Unger	–2 60 54	peter.unger@uni-ulm.de
Deputy Head			
Prof. Dr.	Ferdinand Scholz	–2 60 52	ferdinand.scholz@uni-ulm.de
President of the University of Ulm			
Prof. Dr.	Karl Joachim Ebeling	–2 60 51	karl.ebeling@uni-ulm.de
Senior Research Assistant			
Dr.-Ing.	Rainer Michalzik	–2 60 48	rainer.michalzik@uni-ulm.de
Cleanroom Management			
Dr.-Ing.	Jürgen Mähnß	–2 60 53	juergen.maehnss@uni-ulm.de
Secretaries			
	Christine Bunk	–2 60 50	christine.bunk@uni-ulm.de
	Sükran Kilic	–2 60 51	suekran.kilic@uni-ulm.de
	Hildegard Mack	–2 60 59	hildegard.mack@uni-ulm.de
Guest Scientist			
Dr.	Daniel Hofstetter	–2 60 51	daniel.hofstetter@uni-ulm.de
M. Tech.	Manmohan S. Shishodia*	–2 60 36	manmohan.shishodia@uni-ulm.de
Research Staff			
Dipl.-Ing.	Peter Brückner	–2 60 35	peter.brueckner@uni-ulm.de
Dipl.-Phys.	Frank Demaria	–2 60 46	frank.demaria@uni-ulm.de
M.Sc.	Abdel-Sattar Gadallah	–2 60 36	abdel-sattar.gadallah@uni-ulm.de
Dipl.-Ing.	Philipp Gerlach	–2 60 37	philipp.gerlach@uni-ulm.de
Dipl.-Ing.	Eckart Gerster*	–2 60 57	eckart.gerster@uni-ulm.de
Dipl.-Ing.	Frank Habel*	–2 64 52	frank.habel@uni-ulm.de
Dipl.-Ing.	Joachim Hertkorn	–2 61 95	joachim.hertkorn@uni-ulm.de
Dipl.-Ing.	Ihab Kardosh	–2 60 36	ihab.kardosh@uni-ulm.de
Dr.-Ing.	Christoph Kirchner*	–2 60 35	christoph.kirchner@uni-ulm.de
Dipl.-Ing.	Andrea Kroner	–2 60 38	andrea.kroner@uni-ulm.de
Dipl.-Ing.	Steffen Lorch	–2 60 39	steffen.lorch@uni-ulm.de
Dipl.-Ing.	Barbara Neubert	–2 64 54	barbara.neubert@uni-ulm.de
Dipl.-Phys.	Johannes M. Ostermann	–2 60 38	johannes-michael.ostermann@uni-ulm.de
Dipl.-Ing.	Michael C. Riedl	–2 60 36	michael.riedl@uni-ulm.de
Dipl.-Phys.	Fernando Rinaldi	–2 60 46	fernando.rinaldi@uni-ulm.de
Dipl.-Ing.	Hendrik Roscher	–2 60 44	hendrik.roscher@uni-ulm.de

Dipl.-Ing.	Wolfgang Schwarz	–2 60 38	wolfgang.schwarz@uni-ulm.de
Dipl.-Ing.	Martin Stach	–2 60 37	martin.stach@uni-ulm.de
Dr.-Ing.	Georgi Stareev	–2 64 53	georgi.stareev@uni-ulm.de
Dipl.-Ing.	Sarad Bahadur Thapa	–2 61 95	sarad.thapa@uni-ulm.de
Technical Staff			
	Rainer Blood	–2 60 44	rainer.blood@uni-ulm.de
	Gerlinde Meixner	–2 60 41	gerlinde.meixner@uni-ulm.de
	Susanne Menzel	–2 60 41	susanne.menzel@uni-ulm.de
	Josef Theisz	–2 60 30	josef.theisz@uni-ulm.de

* Member has left the department meanwhile

Preface

2005 was again a rather successful year for the Optoelectronics Department. Research concentrated on optical interconnect systems, vertical-cavity surface-emitting lasers (VCSELs), GaN-based electronic and optoelectronic devices, and optically pumped semiconductor disk lasers.

The VCSELs and Optical Interconnects Group headed by Rainer Michalzik has demonstrated a monolithically integrated transceiver chip for bidirectional optical data transmission and the novel concept of an integrated vertical-cavity laser-based optical trap for applications in biophotonics. Other achievements include 760 nm wavelength VCSELs with record performance, 10 Gbit/s operation of redundant two-dimensional VCSEL arrays, polarization-stable grating relief VCSELs, and complex-coupled integrated DFB–EAM–SOA chips operating at 1.3 μm wavelength. In the GaN Electronics and Optoelectronics Group headed by Ferdinand Scholz, research has been started on AlN, the ultimate nitride semiconductor, which may be attractive for high voltage electronics. Longer wavelength nitride optoelectronics may benefit from our work on semipolar LED structures on GaN stripe facets. In the High-Power Semiconductor Laser Group headed by Peter Unger, a semiconductor disk laser emitting at a wavelength of 975 nm has been realized exhibiting an optical output power of more than 5 W with a differential efficiency of 67 % which corresponds to a differential quantum efficiency of 74 %.

In 2005, the first Ph.D. student who had completed one of our international Master Courses joined our Department. Six members of the Department, namely Eckart Gerster, Christoph Eichler, Thomas Eduard Kibler, Manfred Mundbrod-Vangerow, Torsten Sven Schaal, and Sven-Silvius Schad received their Ph.D. degrees. Rainer Michalzik has served as the Guest Editor of the 2005 Special Issue on Semiconductor Optoelectronics of IEE Proceedings Optoelectronics. In December 2006, Ferdinand Scholz will organize the annual DGKK Workshop on III-V epitaxy, where we expect about 140 participants.

The Department further intensified the close collaboration with industrial partners. We also appreciate the financial support of national and European research organizations, which contribute the major part of our funding. Numerous publications at international conferences and a large number of articles in respected journals document the strong research activities of the Department. A detailed list can be found at the end of this report.

Peter Unger Ulm, March 2006

High Quality GaN Layers Grown on Slightly Miscut Sapphire Wafers

Peter Brückner

HVPE grown layers typically show a high density of pyramidal structures on the surface. We found that a slight off-orientation of the substrate totally suppresses the development of these structures. Further we found that a misorientation towards the M-plane of GaN features a smoother surface morphology as compared to an off-orientation towards the A-plane. After the improvement of the surface morphology and other properties of the HVPE grown layers, we studied self-separation processes. Our approaches to remove the thick GaN layer from the substrate were the introduction of a low-temperature intermediate layer and a structured dielectric mask.

1. Introduction

The improvement of GaN based electronic and optoelectronic devices, especially for short wavelength optoelectronics, is still limited by the fact that the epitaxial structures have to be grown on substrates like sapphire or SiC, because high quality bulk GaN wafers are still not readily available. The growth on foreign substrates causes a high defect density, which limits the efficiencies and life times of these devices. Therefore, the heteroepitaxial growth by hydride vapour phase epitaxy (HVPE) of thick GaN layers which can be used as quasi-substrates for the device epitaxy has been developed by several groups [1, 2]. On such layers, excellent electronic and optoelectronic devices, in particular laser diodes [3] and light emitting diodes [4] have been fabricated. HVPE grown layers, however, still suffer from several problems. They normally show a quite rough pyramidally shaped surface, thus requiring a polishing step before their use in a following device growth. To reduce the strain of those layers and the bowing, it is necessary to remove the foreign substrate after the HVPE process to get free-standing GaN wafers.

We studied the influence of several growth parameters on the electrical and optical properties and the surface morphology of the HVPE grown layers. Quite recently, several groups have reported that a slight substrate misorientation may improve the GaN layer quality considerably in MOVPE [5, 6]. Our own preliminary experiments showed that the misorientation of the wafer is of major importance also in HVPE [7, 8]. Hence, we have systematically investigated the influence of the substrate miscut on the HVPE grown layer properties by varying angle and direction of the misorientation of the sapphire substrate used.

For a further improvement of GaN-based devices it is necessary to remove the foreign substrate from the HVPE-grown layer. Several groups developed such a process. One possibility is to remove the foreign substrate by laser lift-off (LLO) [9] or by using GaAs as substrate for the HVPE growth, which can be easily removed [10] in a wet chemical process. Another possibility is to use self-separation processes, which make use of the thermal strain between the foreign substrate and the thick GaN layer during cool down from growth temperature to room temperature. Y. Oshima et. al. [11] used a TiN interlayer to generate a well-defined break point. We investigated different approaches towards free-standing GaN by separating our thick HVPE-grown layers in-situ during cooling-down after the epitaxial process. One way is the growth on masked templates, similar as described by Tomita et al. [12], where the geometry and the filling factor can be optimized for best self-separation. Another way was proposed by Zhillyaev et al. who inserted a low-temperature interlayer near the substrate to define the self-separation break point [13]. However, only small pieces of free-standing GaN have been obtained, and no details of their procedure were published.

2. Experimental

The experiments described in this paper have been performed in an Aixtron single wafer HVPE machine with a horizontal quartz reactor. As usual, metallic Ga was transported by HCl gas to the substrate, whereas ammonia was used as nitrogen precursor. The Ga source was kept at 850° C, while the substrate zone was heated to 1050−1070° C. A freely adjustable mixture of nitrogen and hydrogen could be used as carrier gas to influence the strain state during growth, thus controlling the cracking behaviour of the grown layer [14]. This enabled the growth of 140 µm thick crack-free layers directly on GaN templates on sapphire without the necessity of any strain compensating layer. The reactor pressure can be adjusted between 200 and 950 mbar.

All layers have been grown on GaN templates deposited by MOVPE to avoid the effort of developing a nucleation process in HVPE. The templates with a GaN thickness of approx. 1.5 µm were grown in a single wafer MOVPE reactor with an AlN nucleation layer [15]. Besides the different misorientations, the templates showed very similar properties [8]. By growing on quarters of 2 inch templates, up to four different samples could be overgrown simultaneously in one HVPE run on a rotating susceptor. The wafer misorientation was varied, moreover the two main misorientation directions versus A-plane and M-plane were studied. All layers have been characterized by standard tools like optical microscopy, high resolution x-ray diffraction, low-temperature photoluminescence and atomic force microscopy.

3. Discussion

3.1 Influence of the miscut direction

As described in earlier publications, a careful optimization of the process parameters is necessary to improve the surface quality and the properties of the HVPE grown layers. Basic studies [7, 8] brought the wafer miscut into our focus. These publications describe the improvement of the surface quality by using templates with a slight off-orientation of

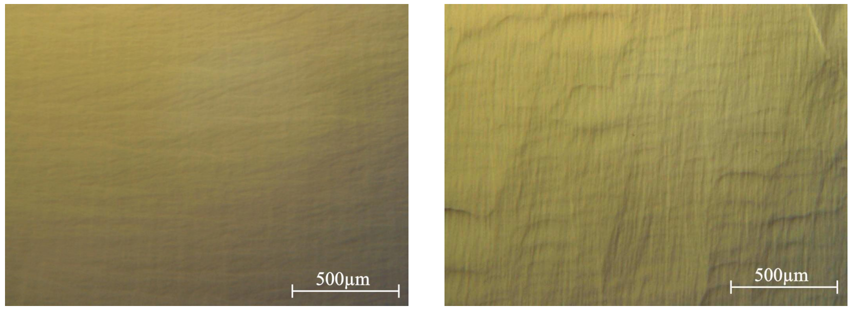

Fig. 1: Optical interference contrast micrographs of the two HVPE-grown layers on templates with different miscut direction. The off-orientation of the sapphire was 0.5° towards the A-plane (left) and 0.6° towards the M-plane (right).

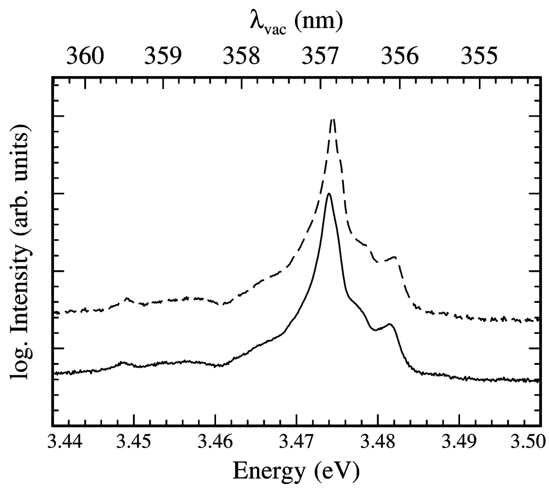

Fig. 2: Low-temperature (T = 4.2 K) photoluminescence spectra of the 80 μm thick HVPE grown layers on sapphire, grown in the same HVPE run with 0.5° misorientation towards the A-plane (dashed line) and 0.6° towards the M-plane (solid line, x10 to separate the two spectra).

the c-direction of the used sapphire substrate. These experiments exhibited an optimum off-orientation from the c-plane of approximately 0.3°. No clear difference was observed between samples using this fixed misorientation angle towards the a- and m-orientation.

After the availability of sapphire wafers with higher off-orientation angles in both directions, the influence of the miscut on the surface morphology could now be clarified. We studied the growth on exact, 0.3°, 0.6° and 1° miscut sapphire wafers in both directions. The results of these studies confirmed that the optimum off-orientation of the used template is approximately 0.3°, as described in Ref. [7]. For lower values, the typical rough pyramidally shaped surface could not be suppressed. By using a substrate off-orientation of 1°, the surface morphology changed towards a rough line shaped surface.

Figure 1 (left and right) presents two optical interference contrast micrographs of 80 μm thick HVPE layers directly grown on the templates with the two perpendicular miscut orientations. The sample with the sapphire off-orientation towards the A-plane (fig. 1 left) showed a much better surface morphology compared to the other sample (fig. 1

(a) 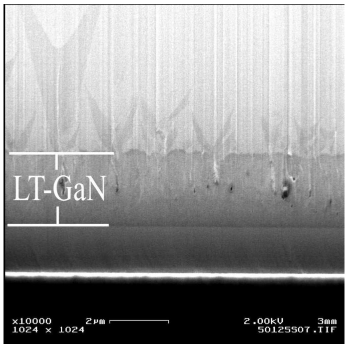

(b) 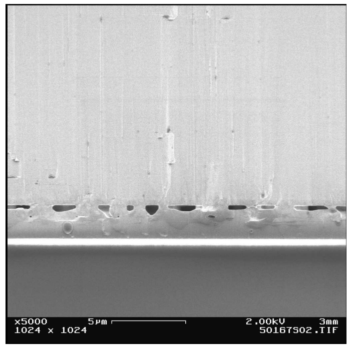

(c) 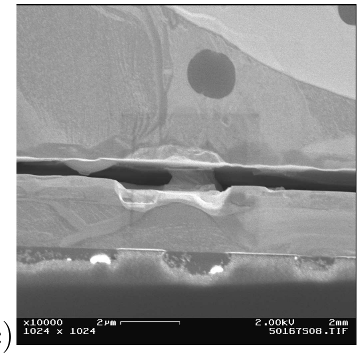

Fig. 3: Scanning electron microscopy pictures of the cross-section of HVPE grown layers. The cavernous layers were generated by a low temperature interlayer grown directly on the GaN-template and subsequent standard growth of HVPE-GaN. The interlayer was deposited at a temperature of 800° C (a) and at 700° C (b, c).

right). This may be attributed to the different dangling bonds of the steps compared to the other miscut direction, as pointed out by Tachibana el al. [16] describing studies on GaInN quantum well structures grown by MOVPE. Nevertheless, both samples showed excellent material quality. We measured Hall mobilities of approx. $780\,\mathrm{cm^2/Vs}$ with carrier densities in the lower $10^{16}\,\mathrm{cm^{-3}}$ range at room temperature. The photoluminescence spectra (Fig. 2) of both HVPE-grown layers showed an extremely narrow line of the bound exciton transition with a half width below 900 μeV. No yellow luminescence was detectable.

3.2 Self-separation of thick layers

We studied self-separation processes which make use of the thermal strain during cool-down. We investigated different approaches to generate well defined break points where the separation process can occur. The first approach was to deposit a low-temperature interlayer to define the break point as described by Zhilyaev et al. [13]. The low-temperature interlayer was deposited directly on a GaN template (1.5 μm MOVPE-GaN on c-plane sapphire) in HVPE. This layer caused a contrast in the scanning electron micrograph, see Fig. 3 a). By a further reduction of the deposition temperature of the LT-GaN interlayer a cavernous layer developed, see Fig. 3 b) and c). On the SEM picture in Fig. 3 c) it is clearly visible that the connection between the seed layer and the thick HVPE grown layer is made only by small pillars. These pillars break easily during cool down and separate the thick layer from the seed layer. Unfortunately, the connectivity of this cavernous layer was rather inhomogeneous (compare figs. 3 b and c) yielding in the separation of only small pieces of the GaN layer. However, self-separated layers exhibited a photoluminescence spectrum which is comparable to MOVPE-grown templates. They featured no yellow luminescence, clearly visible free excitons and a half-width of the donor bound exciton transition of less than 2.6 meV at 20 K.

We found, that the uniformity of the break point over the whole wafer could be better defined with a dielectric mask. In contrast to the method described by Tomita et. al. [12], our process starts with the deposition of a dielectric mask on a GaN layer on sapphire.

This mask was structured with a periodic pattern with standard lithography and laterally overgrown (like an ELO-process) in a MOVPE system providing a high quality template [17] for the final HVPE growth. The important parameter which influences the separation process is the filling factor (ratio between the openings and the mask area), which can be easily changed by the design of the used mask. This defines the connection strength between the seed layer and the thick HVPE-grown layer.

The first experiments were done one a periodic stripe mask with a filling factor of approximately 0.27. Unfortunately, our maximum layer thickness in these experiments was limited to about 330 μm because of parasitic depositions in our HVPE reactor. Nevertheless, the layer showed self-separation and fairly large freestanding GaN samples could be achieved (fig. 4a). These layers exhibited a very low defect density in the mid $10^6\,\mathrm{cm}^{-2}$ range as evaluated by high temperature etching [18]. Extremely narrow lines of two bound exciton transitions with a halfwidth below 670 μeV were observed confirming the low background impurity concentration of our samples (see Hall results described above). The donor bound exciton at 3.471 eV is assigned to O_{Ga} donors and the other peak at 3.472 eV to Si_{Ga}, which may be partly caused by the used SiN mask. Moreover, strong signals of several free exciton states could be found (fig. 4b).

3.3 Summary

It was demonstrated, that an off-orientation of the sapphire towards the a-plane results in a better surface morphology. Layers grown on off-oriented templates showed an excellent PL-spectrum with narrow linewidths. We described different approaches for self-separation processes. One possibility is to grow a low-temperature interlayer directly on the seed layer. This process could be easily integrated directly in the process, but it is difficult to control its uniformity over the whole wafer. As an alternative, we investigated the growth on patterned substrates, where the mask defines the breakpoint. By using this process we were able to get quite large samples of free standing GaN with excellent optical and electrical properties.

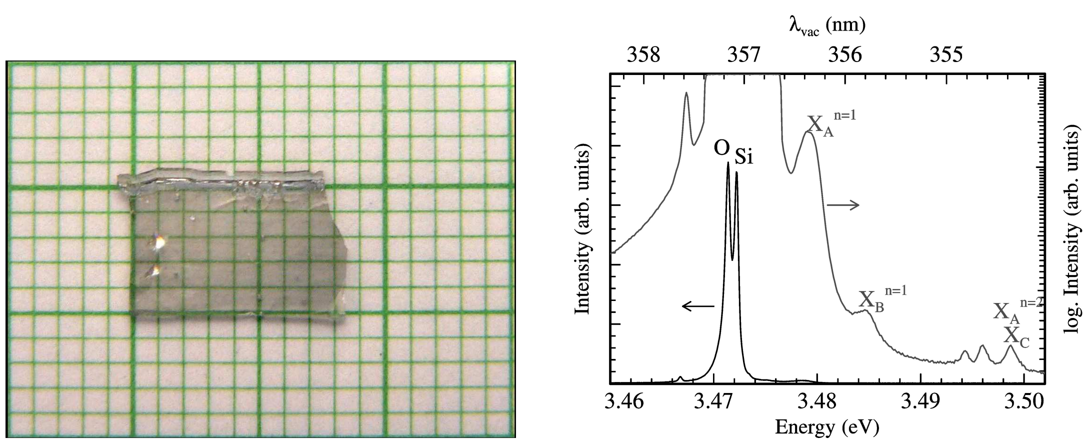

Fig. 4: Picture of a 330 μm thick HVPE-grown self-separated layer (1 square is equal to $1\,\mathrm{mm}^2$). Low-temperature (T = 4.2 K) photoluminescence spectra of the layer.

References

[1] S. S. Park, I.-W. Park and S. H. Cho, *Jpn. J. Appl. Phys.* 39, L1141, 2000.

[2] X. Xu, R.P. Vaudo, C. Loria, A. Salant, G.R. Brandes and J. Chaudhuri, *J. Crystal Growth* 246, 223, 2002.

[3] M. Kuramoto, C. Sasaoka, Y. Hisanaga, A. Kimura, A. A.Yamaguchi, H. Sunakawa, N. Kuroda, M. Nido, A. Usui and M. Mizuta, *Jpn. J. Appl. Phys.* 38, L184, 1999.

[4] X. A. Cao, S. F. LeBoeuf, M. P. D'Evelyn, S. D. Arthur, J. Kretchmer, C. H.Yan and Z. H.Yang, *Appl. Phys. Lett.* 84, 4313, 2004.

[5] D. Lu, D. I. Florescu, D. S. Lee, V.Merai, J. C. Ramer, A. Parekh and E. A. Armour, *J. Crystal Growth* 272, 353, 2004.

[6] T.Yuasa, Y. Ueta, Y. Tsuda, A. Ogawa, M. Taneya, K. Takao, *Jpn. J. Appl. Phys.* 38, L703, 1999.

[7] P. Brückner, F. Habel and F. Scholz, ICNS6, Bremen 2005, poster contribution, submitted to phys. stat. sol.

[8] F. Scholz, P. Brückner, F. Habel, M. Peter and K. Köhler, *Appl. Phys. Lett.* 87, 181902, 2005.

[9] C.R. Miskys, M.K. Kelly, O. Ambacher and M. Stutzmann, *phys. stat. sol c* 1, 1627, 2003.

[10] K. Matoki, T. Okahisa, N. Matsumoto, M. Matsushima, H. Rimura, H. Kasai, K. Takemoto, K. Uematsu, T. Hirano, M. Nakayama, M. Nakahata, M. Ueno, D. Hara, Y. Kumagai, A. Koukitu and H. Seki, *Jpn. J. Appl. Phys.* 40, L140, 2001.

[11] Y. Oshima, T. Eri, M. Shibata, H. Sunakawa, K. Kobayashi, T. Ichihashi and A. Usui, *Jpn. J. Appl. Phys.* 42, L1, 2003.

[12] K. Tomita, T. Kachi, S. Nagai, A. Kojima, S. Yamasaki and M.Koike, *phys. stat. sol a* 194, 563, 2002.

[13] Yu. V. Zhillyaev, A. V. Nasanow, S. D. Raevxki, S. N. Rodin, M. P. Shcheglov and V. Yu. Davydov, *phys. stat. sol a* 195, 122, 2003.

[14] F. Habel, P. Brückner, J.-D. Tsay,W.-Y. Liu, F. Scholz, D. Schmitz, A. Alam and M. Heuken, *phys. stat. sol c* 2, 2049, 2005.

[15] B. Kuhn, F. Scholz, *phys. stat. sol a* 188, 629, 2001.

[16] K. Tachibana, H. Nago and S. Nunoue, ICNS6, Bremen 2004, oral presentation.

[17] F. Habel, P. Brückner, F. Scholz, *J. Crystal Growth* 272, 515, 2004.

[18] F. Habel and M. Seyboth, *phys. stat. sol c* 0, 2448, 2003.

Structural and Spectroscopic Properties of AlN Layers Grown by MOVPE

Sarad Bahadur Thapa

The effects on surface morphology and crystal quality of undoped bulk AlN layers, grown on c-plane sapphire substrates, due to the changes in growth conditions in LP-MOVPE are discussed here. The optimized growth process has led to an almost flat surface morphology with a significantly reduced number of hexagonal pits and good crystalline quality having a rms value of roughness of 0.4 nm and a FWHM value of the X-ray rocking curve for the (0002) reflection of 200 arcseconds. These excellent data were further confirmed by a strong donor-bound exciton luminescence signal with a FWHM of approx. 25 meV. Besides the structural and spectroscopic properties of AlN bulk layers, the HRXRD and TEM studies of AlN/GaN superlattice structure are reported here.

1. Introduction

Due to its wide direct band gap (approx. 6 eV) and the associated outstanding chemical and thermal stability, the realization of high-quality AlN epitaxial layers can widely extend the application field of III-V nitride materials. AlN could be a very promising material for high-temperature high-power applications, e.g. high-power field effect transistors, and opto-electronic devices, particularly UV diodes. Furthermore, AlN/GaN superlattice structures can be used in optical devices operating at telecommunication wavelengths by exploiting intersubband transitions between bound quantum well states [1].

However, the growth of AlN having excellent crystalline quality, smooth surface morphology, and good electrical and optical properties - as required for device fabrication - is always a big challenge. One major problem during the epitaxial growth of AlN is the parasitic reaction between ammonia and the metalorganic aluminum source TMAl (trimethylaluminum), which can be minimized by reducing the reactor pressure and upstream positioning of the substrate on the susceptor [2]. To obtain good crystalline quality and smooth surface morphology of AlN layers, many experiments have been carried out in low-pressure metal organic vapor phase epitaxy (LP-MOVPE) by changing the growth parameters. The effects of the variation of some basic growth parameters on the surface morphology, crystal quality, growth rate and consequently on the cathodoluminescence spectra are reported here.

2. Experiment

Undoped layers of AlN, approximately 500 nm thick, were grown on three different orientations of c-plane sapphire substrates, namely exactly oriented (on-axis), 0.3° miscut towards m-plane (off-axis to m-plane), and 0.3° miscut towards a-plane (off-axis to a-plane). The growth process was carried out in an AIXTRON AIX 200 RF LP-MOVPE system using a low temperature AlN nucleation layer. The growth conditions have been varied with respect to the N_2-H_2 carrier gas composition, total flow, V-III ratio, and the growth temperature. The reactor pressure was kept constant at 35 mbar, the lower limit of our system.

The surface morphology was analyzed by using atomic force microscopy (AFM) and scanning electron microscopy (SEM). High-resolution X-ray diffraction (HRXRD) rocking curve measurements for the (0002) reflection were carried out to examine the crystal quality of bulk AlN epitaxial layers. Low-temperature cathodoluminescence provided information about the spectroscopic properties.

Meanwhile, AlN/GaN (4 nm / 4 nm) superlattice structures (21 periods) were grown on 500 nm thick $Al_{0.5}Ga_{0.5}N$ buffer layers and covered with a 40 nm thick $Al_{0.5}Ga_{0.5}N$ cap. The growth interruption time was kept 5 s after each layer grown of AlN and GaN. The HRXRD measurement of the ω-2θ scan (0002 reflection) was performed to verify the periodicity and transmission electron microscopy (TEM) was used to examine the abruptness of the interfaces of the superlattice structure.

3. Result and Discussion

It is found that, at the same growth conditions, the full width half maximum (FWHM) value of the X-ray rocking curve for the (0002) reflection of undoped AlN layer grown on c-plane sapphire substrate off-axis to m-plane is comparatively narrower than that on on-axis and off-axis to a-plane. This shows c-plane sapphire substrate off-axis to m-plane is a good choice for the AlN epitaxial growth. However, there is no significant impact on the surface morphology and growth rate of AlN epitaxial layers due to the different orientations of substrates.

Before optimization, the surfaces showed either whisker-like features of rough grainy characteristics, or columnar textures. Moreover, the presence of a large number of hexagonal-shaped pits of varying size, depth and diameter, as shown in fig. 1 (left), was observed. Similarly, the crystalline quality (as measured by the FWHM of HRXRD) of the layers was inferior, too.

When increasing the growth temperature, substantial morphological differences on the surface quality of the bulk AlN layer were observed. AFM measurements exhibited a remarkable reduction of the rms value of the surface roughness from 21.5 nm to 1.5 nm when increasing the growth temperature from 1110°C to 1170°C. However, further increase of growth temperature is restricted by the system limitations. Meantime, it is noticed that the surface roughness decreases with the increase of total flow whereas the FWHM value of the X-ray rocking curve for the (0002) reflection decreases with the decrease of V-III ratio as shown in fig. 2. Moreover, it is observed that the growth rate increases with the decrease of N_2-H_2 ratio as illustrated in fig. 3. This result is somewhat contrary to the observations made by other groups [3] in the high-temperature GaN growth. However, the increased amount of N_2 drastically decreases the substrate temperature [4] which may explain the decreasing growth rate.

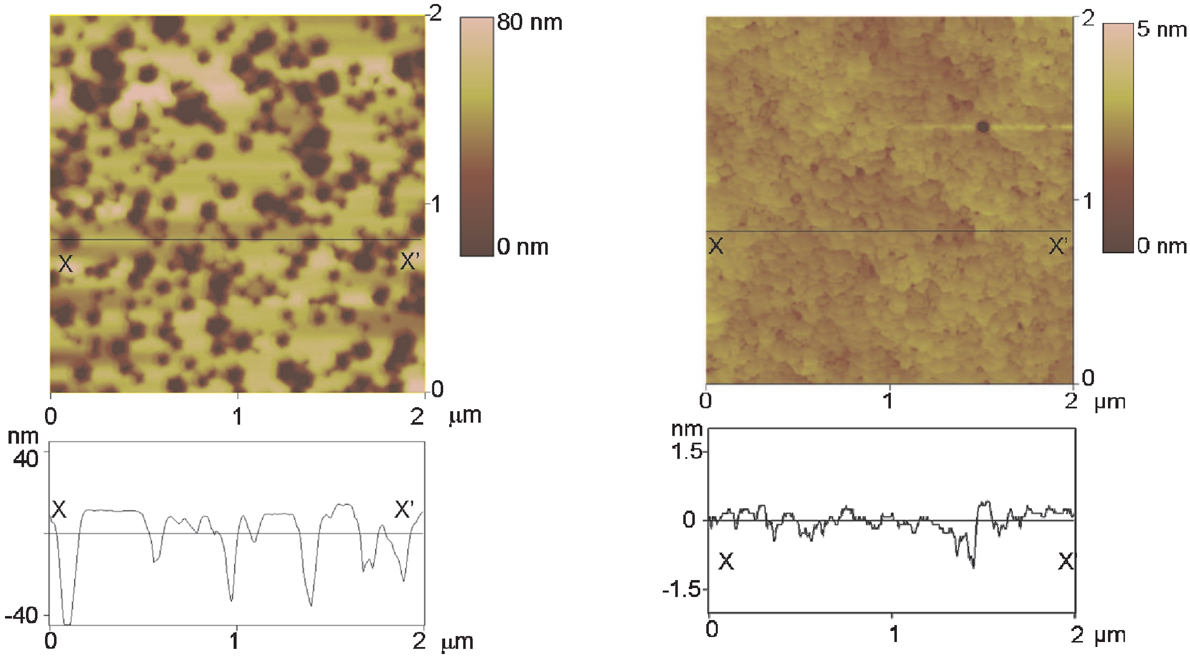

Fig. 1: AFM image of bulk AlN layer before optimization(left). Many of hexagonal pits are visible on the surface. The rms surface roughness of 2x2 μm scan is 21.5 nm. AFM image of bulk AlN layer after optimization(right). A hexagonal pit formed after the merging of small pits is also shown and the rms surface roughness of 2x2 μm scan is 0.4 nm

Since the suppression of the pre-reactions between the precursors and the surface diffusion of Al atoms during the growth process are the key factors in determining the surface morphology, the growth process was hence optimized by decreasing the ammonia and trimethylaluminum flow rate and apparently lowering the V-III ratio at higher growth temperature. The flow rate of N_2 and H_2 was increased to keep the total flow constant.

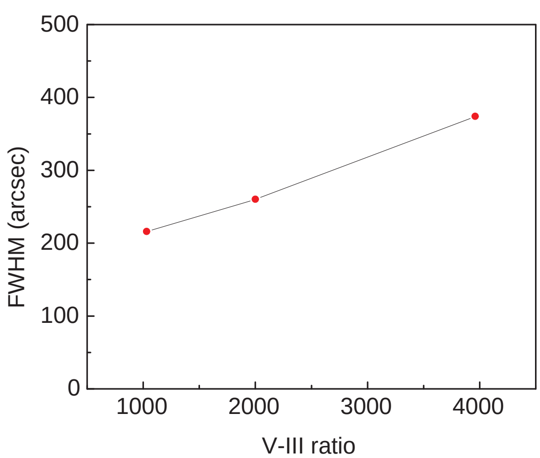

Fig. 2: Change in FWHM value of the X-ray rocking curve for the (0002) reflection with respect to the V-III ratio.

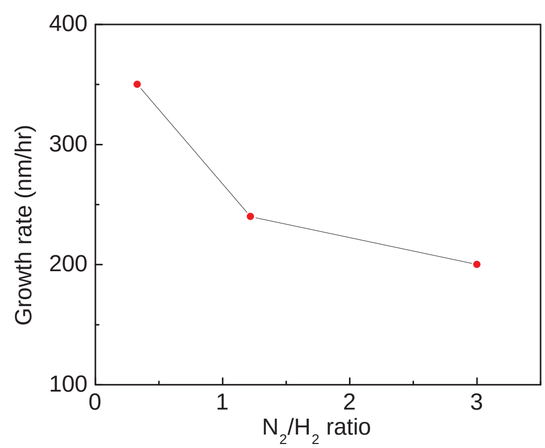

Fig. 3: Change in growth rate with respect to the N_2-H_2 ratio.

As superior CL spectra were ascribed to the samples having lower growth rate, it was customary to keep the N_2-H_2 ratio greater than 1 to maintain the same growth rate. Consequently, the optimized growth process has led to an almost flat surface morphology with a significantly reduced number of hexagonal-shaped pits (approximately $5 \cdot 10^7\,cm^{-2}$) and good crystalline quality. Figure 1 (right) shows the AFM image of a bulk AlN layer after optimization of the growth process. The surface of the AlN layer is a well ordered atomic layer with a measured rms value of the surface roughness of 0.4 nm. The FWHM of the X-ray rocking curve for the (0002) reflection is 200 arcsec. These excellent data were further confirmed by a band edge excitonic emission with a FWHM of 25 meV (fig. 4). The LO phonon replica, shown in the inset of fig. 4, confirm the good optical quality of the bulk AlN epitaxial layers.

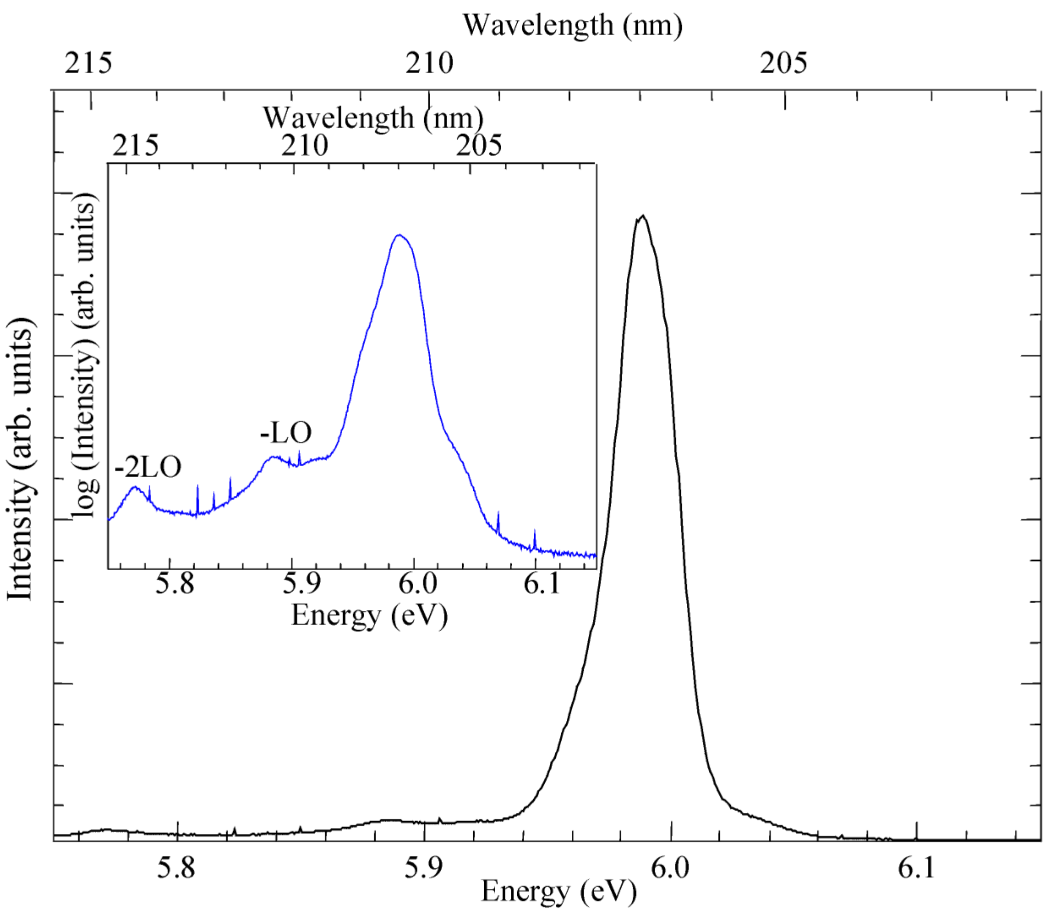

Fig. 4: Low-temperature CL spectra of bulk AlN layer. The LO phonon replica are shown in the inset.

After having obtained the required crystalline quality and surface morphology of bulk AlN layer, AlN/GaN superlattice structure were grown on c-plane sapphire. Figure 5 (left) illustrates the HRXRD measurement of the ω-2θ scan (0002 reflection) of such a structure which shows the superlattice related satellite peaks (SL) confirming the good periodicity of the layers. The defects and the abruptness of the interfaces of the superlattice structure

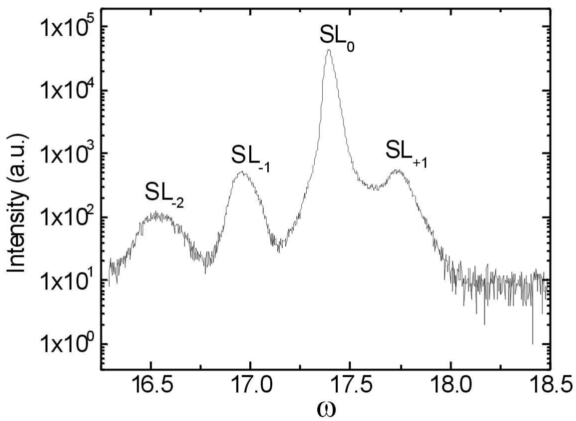

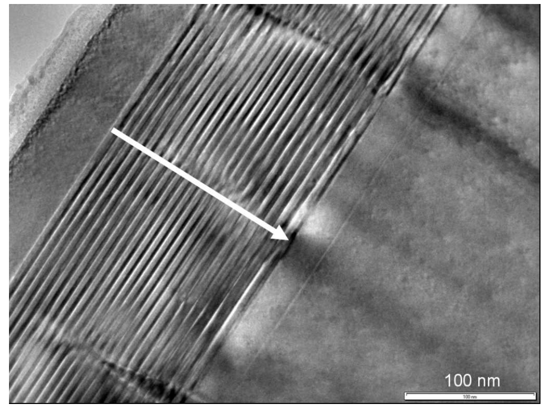

Fig. 5: HRXRD measurement of the ω-2θ scan (0002 reflection) of AlN/GaN superlattice (left). TEM-bright-field image of the superlattice structure (right). The white arrow shows the structure from the cap to buffer layer. Bright and dark layers in superlattice structure are AlN and GaN, respectively

were investigated by transmission electron microscopy (TEM). The TEM-bright-field image of the superlattice structure is shown in fig. 5 (right) where the bright layer is AlN and the dark, GaN. Obviously, the interfaces of AlN on GaN are sharper than those of GaN on AlN and many of the threading dislocations coming through the $Al_{0.5}Ga_{0.5}N$ buffer layer are stopped at the interface between the buffer layer and superlattice structure.

4. Conclusion

Undoped AlN layers, with high crystalline quality and almost flat surface morphology, were grown on 0.3° miscut towards m-plane oriented c-plane sapphire substrate by LP-MOVPE. After optimization, we achieved an rms value of the surface roughness of 0.4 nm and the FWHM of the X-ray rocking curve for the (0002) reflection of 200 arcsec. The low-temperature CL spectra demonstrates the good optical quality of the AlN layer. Consequently, it was possible to grow AlN/GaN superlattice structures having good periodicity and abruptness of the AlN/GaN interfaces.

5. Acknowledgement

Special thanks go to Christoph Kirchner for his contributions to many of the epitaxial growths of AlN heterostructures. I would like to thank G. Prinz, and K. Thonke of Semiconductor Physics Department for CL measurements; S. Groezinger, A. Chuvilin, and U. Kaiser of Materialwissenschaftliche Elektronenmikroskopie for TEM measurements; and A. Minkow of Materials Division for SEM measurements. This work was financially supported by Sofja Kolajewskaja Program of the Alexander von Humboldt foundation and Deutsche Forschungsgemeinschaft.

References

[1] I. Waki, C. Kumtornkittikul, Y. Shimogaki, and Y. Nakano, *Appl. Phys. Lett.*, vol. 82, no. 25, pp. 4465–4467, 2003

[2] C. Kirchner, *Annual Report 2004, Optoelectronics Department, Ulm University.*

[3] R. Steins, H. Hardtdegen, N. Kaluja, M.v.d. Ahe, Y.S. Cho, and Z. Sofer, in Proc. *11th European Workshop on MOVPE*, pp. 341–343, Lausanne, Switzerland, June 5th-8th, 2005

[4] N. Kaluza, R. Steins, Y.S. Cho, Z. Sofer, and H. Hardtdegen, in Proc. *11th European Workshop on MOVPE*, pp. 179–181, Lausanne, Switzerland, June 5th-8th, 2005

Growth Characteristics of GaInN Quantum Wells on Semipolar GaN Facets

Barbara Neubert

Multiple GaInN quantum wells (QWs) were grown on side facets with reduced piezoelectric fields (PFs) of selectively grown GaN stripes oriented along the $\langle 1\bar{1}00\rangle$ and $\langle 11\bar{2}0\rangle$ directions by metalorganic vapor phase epitaxy (MOVPE). The different luminescence wavelengths observed for the QWs on these facets can be explained by the reduced PFs, additionally the QW thickness depends on the facet type. Although stripes running along $\langle 1\bar{1}00\rangle$ and $\langle 11\bar{2}0\rangle$ develop similar triangular or trapezoidal shape, their detailed growth behaviour, electrical and luminescence properties differ significantly pointing to different adsorption/desorption and inter-facet migration processes of In, Ga and the p-type dopant Mg.

1. Introduction

Group III nitrides became very important for the short wavelength region of the visible spectrum for light emitting devices. But due to the polarity of group III nitrides, strong piezoelectric fields are induced in biaxially strained GaInN QWs grown on $\langle 0001\rangle$-oriented GaN [1]. This gives rise to a spatial separation of the electron and hole wave functions what hampers their radiative recombination (quantum confined Stark effect). This effect can be reduced for QWs grown along directions other than the most commonly used $\langle 0001\rangle$ [2], thus potentially leading to improved optical characteristics for light emitting devices. However, when forcing the epitaxial growth into non-piezo-electric directions by using other substrates like r-plane sapphire, usually only poor layer quality can be achieved. Therefore, we have fabricated LED structures on such other crystal planes in-situ on side facets of selectively grown GaN stripes on a masked GaN template on c-plane sapphire. Depending on the mask geometry and the growth parameters, triangularly or trapezoidally shaped GaN stripes developed in the mask openings with $\{11\bar{2}2\}$ side-facets for the $\langle 1\bar{1}00\rangle$-oriented stripes and $\{1\bar{1}01\}$ side-facets for the $\langle 11\bar{2}0\rangle$-oriented stripes, respectively. Integral photo- and electroluminescence measurements showed, that the emission wavelength of the GaInN QWs is different for the different crystal facets and the planar grown reference LED [3]. We conducted now detailed investigations on the growth characteristics of the active region by determining their growth rate and their emission wavelengths, and compared the In content of the two stripe directions.

2. Experiment

All samples under study have been grown by low pressure MOVPE in a single wafer Aixtron system with a horizontal reactor design. A 1.5 µm thick GaN template on c-plane sapphire was covered with 200 nm SiO_2 by plasma enhanced chemical vapor deposition and patterned to stripes along the $\langle 11\bar{2}0\rangle$ and $\langle 1\bar{1}00\rangle$ directions by optical lithography and reactive ion etching to serve as regrowth mask. The dimensions of the mask openings and mask periods ranged from 4 to 8 µm and from 6 to 300 µm, respectively. Here, we studied dimensions of mask openings of 6 µm and mask areas ranging from 2 to 20 µm, respectively, what results in periods ranging from 8 to 26 µm. The parameters of the second epitaxial step have been optimized to grow triangularly or trapezoidally shaped n-doped GaN stripes in the mask openings for both stripe orientations. This leads to $\{11\bar{2}2\}$ side-facets for the $\langle 1\bar{1}00\rangle$-oriented stripes and $\{1\bar{1}01\}$ side-facets for the $\langle 11\bar{2}0\rangle$-oriented stripes, respectively and also $\{0001\}$-facets on top of the trapezoidal structures for both stripe directions. Thereon, we have grown a period of 5 GaInN QWs separated by GaN barriers followed by a p-doped GaN top layer. In order to get an appropriate In incorporation, the QWs as well as the GaN barriers between them were grown at a reduced temperature of 830 °C, whereas all other layers have been grown at standard temperature for GaN of 1020 °C. For comparison the same structure was grown as a planar LED structure on a c-plane template, denoted as planar reference LED structure, whithout any stripe patterning.

We used scanning electron microscopy (SEM) and transmission electron microscopy (TEM) to investigate the thickness and facet properties of the grown structures, further with secondary ion mass spectroscopy (SIMS) we got information about the In content.

3. Results and Discussion

As it is well-known from selective growth of group III arsenides and phosphides [4, 5], the local growth rate of the selectively grown structures increases due to gas phase diffusion of the precursor gases from the masked areas to the growth windows. We have determined the local growth rate by evaluating the volume of the deposited material of single stripes to take into account the different shape of our structures. As the active region is the most interesting part of a LED structure, we concentrated our current studies on this area. For comparison of the different facet types with the planar grown reference LED on the c-plane template, we normalized the volume of the deposited material to the period area, defined as the sum of open and mask area (Fig. 1). We found indeed that this normalized amount of deposited material on the inclined side facets was rather constant for the $\langle 1\bar{1}00\rangle$-oriented stripes and fits to the growth rate of the planar grown reference sample. However, for the stripes oriented along $\langle 11\bar{2}0\rangle$, we found an increased growth rate for the active region (Fig. 1) for triangularly shaped stripes, i. e. for periods ≥ 16 µm. Owing to the limited resolution of our SEM, the GaInN QW thickness was extracted from the thickness of the whole active region by assuming the same growth rates for the QWs and GaN barriers grown under identical conditions, which is appropriate because the In content of these QWs is below 20 %.

When looking closer in particular to trapezoidally shaped stripes (Fig. 2 and 3), it becomes evident that the local growth rate within one stripe varies strongly for different facet types. Similarly as reported by Nishizuka et. al. [6], we found a larger growth rate on the top c-plane facet of the trapezoid for the active region of such stripes at the expense of a lower growth rate on the side facets (Fig. 2 and 4). This is partly due to the increased area of the side facets, which are larger by a factor of $1/\cos\phi$ compared to the respective sample area where ϕ describes the facet angle ($62°$ and $58°$ for $\{1\bar{1}01\}$ and $\{11\bar{2}2\}$ [7], respectively). For our stripes, this results in about a factor of 2 describing fairly well the thickness differences between top and side facets for stripes oriented along the $\langle 1\bar{1}00\rangle$ direction. As described above, this goes with a good fit of the totally deposited material (Fig. 1). However, stripes oriented in the other direction behave strongly different: Here, the top and side facet growth rates differ by a factor of ≈ 4. Besides obviously different adsorption-desorption processes, this seems to be caused by some inter-facet migration of Ga or its adsorbed precursor molecules.

The two stripe directions differ also in the luminescence peak position. Fig. 5 shows the peak emission wavelength of the QWs on the inclined facets depending on the mask geometry of two different selectively grown samples as well as the planar grown reference LED. The emission wavelengths of the top facets of the trapezoidal stripes for periods of 14 µm and less are not shown here. The dotted line and the star-symbols indicate the peak wavelength of the reference LED and the the solid symbols mark the emission wavelengths of QWs grown on the $\{1\bar{1}01\}$ and $\{11\bar{2}2\}$ facets. The QWs on the former facets emit at considerably longer wavelength than those on the latter for all geometries. The two facets are very similar regarding their PFs [2] due to the similar facet angles ϕ.

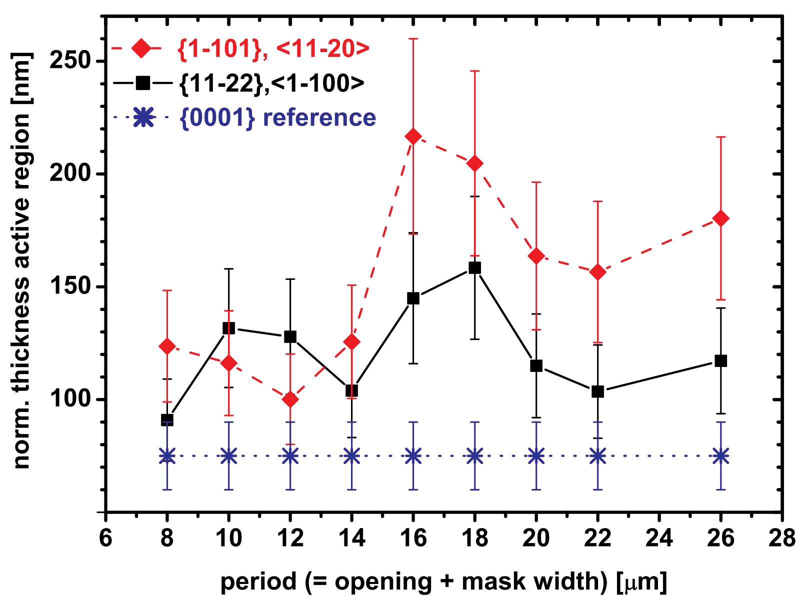

Fig. 1: Grown volume of the active region measured by the cross section area normalized to the period. The investigated stripes are purely triangular for periods ≥ 16 µm.

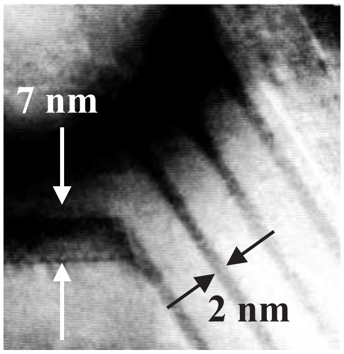

Fig. 2: TEM image of QWs on top and side facets of a stripe with trapezoidal cross section along $\langle 11\bar{2}0\rangle$-direction.

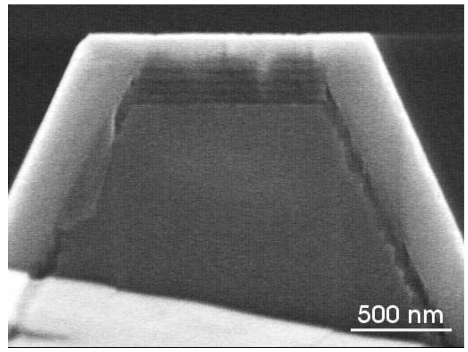

Fig. 3: SEM photograph of a stripe in $\langle 1\bar{1}00\rangle$ direction with trapezoidal cross-section. The Mg-doped GaN cover layer results in a brighter SEM contrast. The 5 QWs are only resolved on the top facet.

Our calculations taking into account the different quantisation and the expected reduced piezoelectric field show that the thickness differences shown in Fig. 4 can explain these PL energy positions only partly. Therefore, we have to assume that additionally, the In incorporation into the QWs is different for both stripe directions. Our calculations describe the experimental data best if we assume about the same In content in the stripes along $\langle 11\bar{2}0\rangle$ as in the reference sample and about 20 % less in the other direction. This may be connected to the different growth rates influencing the In incorporation efficiency [8]. It was also confirmed by SIMS measurements, although here the error bar is quite high.

Finally, the reduced piezoelectric field of the side facets directly results in a shorter wavelength luminescence for both stripe directions compared to the unstructured reference sample (Fig. 5). This is most evident for those stripes where we found the same or even thicker quantum wells on the triangular stripes (large periods in Fig. 4).

The growth behaviour described above for the active region of our LED structures seems to change strongly when growing the Mg doped GaN top layer. As can be seen in Fig. 3, the p-GaN layer (brighter contrast in the SEM image) is much thicker on the inclined facets than on the c-plane top facet. Even for stripes which showed triangular cross-section after completion of the active region, we observed the development of a c-plane top facet consisting of p-doped GaN. Without any doping, the top layer above the side facet QWs is much thicker than with Mg doping. A higher lateral growth rate of Mg doped GaN was also reported by Beaumont et. al. [7], whereas Ren and Dapkus found just the opposite growth behaviour [9]. Like Ren and Dapkus, we found indications for a lower Mg incorporation on the $\{11\bar{2}2\}$ and $\{1\bar{1}01\}$ facets what is mainly concluded from the current-voltage (I-V) characteristics of our LEDs [3]. Further investigations are under way.

4. Conclusion

Concluding our investigations we found a strong blue shift in emission wavelength for GaInN QWs grown on side facets of selectively grown GaN stripes due to the reduced

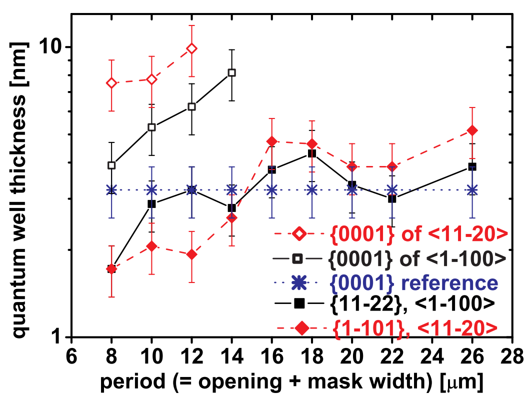

Fig. 4: From thicknesses of active regions calculated QW thicknesses.

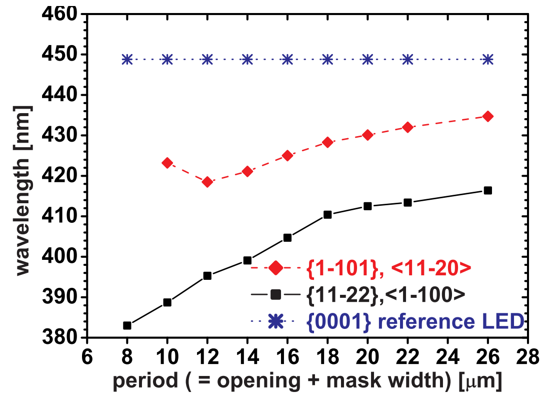

Fig. 5: Room temperature PL emission wavelengths of different inclined facets for increasing periods compared to planar grown LED structures. The investigated stripes are triangular for periods of 16 μm and more.

piezoelectric field on such crystal facets. Strong differences in growth rate, In incorporation and Mg doping behavior were found for the two main stripe directions $\langle 1\bar{1}00\rangle$ and $\langle 11\bar{2}0\rangle$.

Acknowledgments

We like to thank M. Jetter and G. Moutchnik of University in Stutgart for SIMS and M. Beer and J. Zweck of University in Regensburg for TEM measurements.

References

[1] F. Bernardini, V. Fiorentini, and D. Vanderbilt, "Spontaneous polarization and piezoelectric constants of III-V nitrides," *Phys. Rev. B*, vol. 56, no. 16, p. R10024, 1997.

[2] T. Takeuchi, H. Amano, and I. Akasaki, "Theoretical study of orientation dependence of piezoelectric effects in wurtzite strained GaInN/GaN heterostructures and quantum wells," *Jpn. J. Appl. Phys.*, vol. 39, no. 2A, p. 413, 2000.

[3] B. Neubert, F. Habel, P. Brückner, F. Scholz, T. Riemann, and J. Christen, "Electrolumienscence from GaInN quantum wells grown on non-(0001) facets of selectively grown GaN stripe," *Mat. Res. Soc. Symp. Proc.*, vol. 831, p. E11.32.1, 2005.

[4] M. Aoki, H. Sano, M. Suzuki, M. Takahashi, K. Uomi, and A. Takai, "Novel structure MQW electroabsorption modulator/DFB-laser integrated device fabricated by selective area MOCVD growth," *Electron. Lett.*, vol. 27, no. 23, p. 2140, 1991.

[5] C. Caneau, R. Bhat, C.C. Chang, K. Kash, and M.A. Koza, "Selective organometallic vapor phase epitaxy of Ga and In compounds: a comparison of TMIn and TEGa versus TMIn and TMGa," *J. Cryst. Growth*, vol. 132, p. 364, 1993.

[6] K. Nishizuka, M. Funato, Y. Kawakami, Sg. Fujita, Y. Narukawa, and T. Mukai, "Efficient radiative recombination from $\langle 11\bar{2}2 \rangle$-oriented InGaN multiple quantum wells fabricated by the regrowth technique," *Appl. Phys. Lett.*, vol. 85, no. 15, p. 3122, 2004.

[7] B. Beaumont, M. Vaille, G. Nataf, A. Bouillé, J.-C. Guillaume, Ph. Vennéguès, S. Haffouz, and P. Gibart, "Mg-enhanced lateral overgrowth of GaN on patterned GaN/sapphire substrate by selective metal organic vapor phase epitaxy," *MRS Internet J. Nitride Semicond. Res.* , vol. 3, no. 1, p. Art. 20, 1998.

[8] S. Keller, B.P. Keller, D. Kapolnek, A.C. Abare, H. Masui, L.A. Coldren, U.K. Mishra, and S.P. DenBaars, "Growth and characterization of bulk InGaN films and quantum wells," *Appl. Phys. Lett.*, vol. 68, p. 3147, 1996.

[9] D. Ren and P.D. Dapkus, "Anisotropic Mg incorporation in GaN growth on nonpolar templates," *Appl. Phys. Lett.*, vol. 86, no. 12, p. 121901, 2005.

Experimental and Theoretical Study of Transport Properties in n-type $Al_xGa_{1-x}N$/GaN Superlattices

Joachim Hertkorn

In many AlGaN-based devices like FETs, light-emitting diodes or laser diodes the problem of low carrier mobility is omnipresent. In order to minimize the contact area in high power LEDs, high lateral conductivity must be achieved without compromising too much the vertical conductivity. Highly Si- or Mg-doped $Al_xGa_{1-x}N$/GaN-heterostructures are one opportunity to achieve better lateral conductivity in this material system. In a first step heterostructures were modeled by simulation tools. Afterwards such superlattice structures were grown by metal organic vapor phase epitaxy (MOVPE). Finally the results found by experiment were compared to the simulation results.

1. Introduction

Efficient n- and p-type doping of III-nitride semiconductors is imperative for the development of wide band gap electronic and optoelectronic devices. One problem of these devices is that, due to the low mobility of n- and especially p-type carriers in GaN, the resistance of the current guiding layers causes high power dissipation. To address this problem we carry out research on highly Si-doped AlGaN/GaN-hetero- structures. At the interface of these materials a two dimensional electron gas (2DEG) occurs (Fig. 1). In the 2DEG free carriers with much higher mobility compared to GaN:Si-bulk material are accumulated. Thus the lateral conductivity in the superlattice structure is increased compared to standard Si-doped GaN-layers. By increasing the lateral conductivity the contact size of LED's can be reduced what directly leads to higher output efficiencies of the devices. However, by using the AlGaN/GaN superlattice the influence on the vertical resistance of the structure cannot be neglected.

2. Simulation of Si-doped $Al_xGa_{1-x}N$/GaN-heterostructures

The band structures of the superlattices can be simulated with a software tool called *BandEng* [1]. By solving the Schroedinger- and Poisson equations, the band structures of ternary nitride based compound semiconductors are calculated. Therefore superlattice structures made of GaN, AlGaN and InGaN can be analyzed. Beside the band structure the localized carrier density distribution is calculated. Important parameters which are necessary for a realistic simulation are the thickness and the total number of layers, the Al-concentration x and the doping level n in the $Al_xGa_{1-x}N$:Si layer.

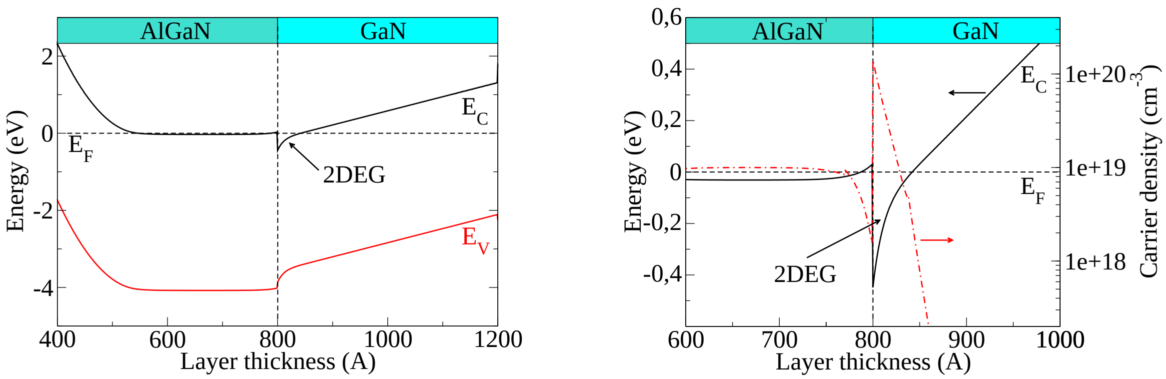

Fig. 1: The band diagram of an $Al_xGa_{1-x}N$ heterostructure, calculated by the *BandEng* software (left). Details of the 2DEG inclusive carrier density distribution (right).

In figure 1 (left) the band diagram of an $Al_xGa_{1-x}N$ heterostructure, with a period length of 80 nm (AlGaN + GaN = 40 nm + 40 nm), a doping level of $1 \cdot 10^{19}\,\mathrm{cm}^{-3}$ (AlGaN:Si) and an Al-concentration of 27 % is shown. The 2DEG at the AlGaN/GaN-surface can be seen clearly. In the picture on the right side the region surrounding the 2DEG is magnified. Additionally the carrier density distribution is plotted. In dependence of the thickness of the AlGaN-layer, the Al-concentration x and the doping level, a carrier concentration even in the AlGaN-layer occurs (Fig. 2).

The mobility of the carriers accumulated in the AlGaN-layer is much lower than in the 2DEG. The simulation results concerning the conductivity shown in this report are based on a mobility for the carriers in AlGaN (n_1) as a function of the doping of about $\mu_1 = 100...50\,\mathrm{cm}^2/\mathrm{Vs}$ ($1 \cdot 10^{18}...10^{19}\,\mathrm{cm}^{-3}$) [2]. The mobility of the 2DEG carriers (n_2) was estimated to $\mu_2 = 1000\,\mathrm{cm}^2/\mathrm{Vs}$. Such, or even higher values have been reported in typical GaN-2DEG-structures [3].

To get the resultant conductivity of a multi heterostructure it is necessary to expect a parallel conduction in a layered system [4]. First the effective carrier concentration

$$n_{\mathrm{eff}} = \frac{(n_1 \cdot \mu_1 + n_2 \cdot \mu_2)^2}{n_1 \cdot {\mu_1}^2 + n_2 \cdot {\mu_2}^2} \quad [\mathrm{cm}^{-2}] \tag{1}$$

and the effective mobility

$$\mu_{\mathrm{eff}} = \frac{n_1 \cdot \mu_1 + n_2 \cdot \mu_2}{n_{\mathrm{eff}}} \quad [\mathrm{cm}^2/\mathrm{Vs}]. \tag{2}$$

are calculated. Finally the resultant specific conductivity

$$\sigma = \mu_{\mathrm{eff}} \cdot n_{\mathrm{eff}} \cdot e \tag{3}$$

of one AlGaN/GaN-Layer is given. If the total thickness of the heterostructure layers is known, the resultant conductivity of the whole superlattice structure can be calculated (Fig. 3). Finally the simulation figured out that the cascading of 12 nm thick AlGaN- and 8 nm GaN-layers is one optimum with respect to lateral conductivity. In figure 2 this is shown in the case of an Al-concentration $x = 25\,\%$. Calculations regarding the vertical conductivity of these structures will be done in future.

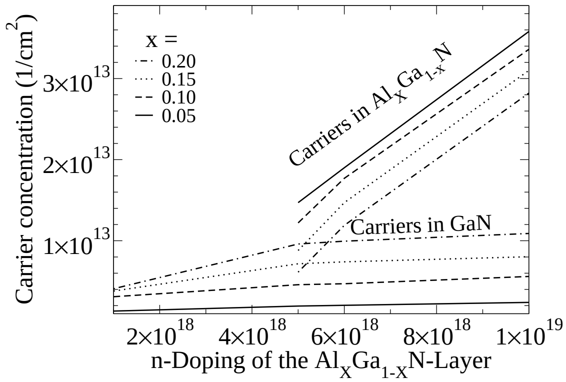

Fig. 2: Accumulation of carriers in the AlGaN-layer as a function of the Al-content x and the Si-doping.

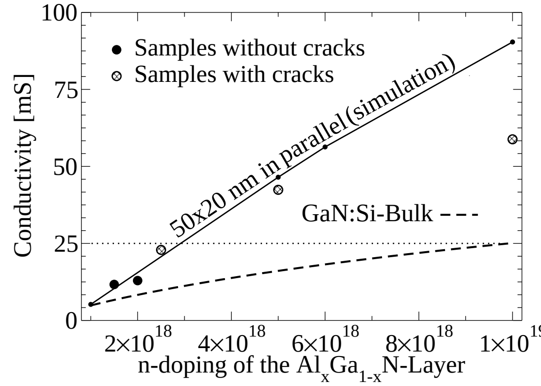

Fig. 3: Comparison of the measured and simulated results (x=25 %)

3. Growth of Superlattices by MOVPE

In our first MOVPE experiments, the superlattice structures were deposited on a 1 μm thick GaN buffer layer. Based on the simulations the AlGaN-layers were made of 15 % and 25 % aluminium, respectively. The AlGaN-barrier was 12 nm, the GaN-interlayer 8 nm thick. The doping varied in between $2 \cdot 10^{18}\,\mathrm{cm}^{-3}$ and $1 \cdot 10^{19}\,\mathrm{cm}^{-3}$. All samples were grown with a reactor pressure of 100 mbar, a temperature of 1125 °C and growth rates in between 500 nm/h and 750 nm/h.

Due to the lattice mismatch of AlGaN and GaN, cracks in the surface were observed, when the total heterostructure layer thickness exceeds 500 nm. The conductivity data measured in these cracked samples (at 1 μm total heterostructure thickness) as well as the simulation results are plotted in figure 3. To reduce the strain we used an AlGaN-layer with the effective Al-content

$$x_{\mathrm{eff}} = \frac{d_{\mathrm{Al}_x\mathrm{Ga}_{1-x}\mathrm{N}} \cdot x}{d_{\mathrm{Al}_x\mathrm{Ga}_{1-x}\mathrm{N}} + d_{\mathrm{GaN}}} \quad . \tag{4}$$

Such a layer leads to an optimized strain compensation and makes it possible to grow at least 1.5 μm thick crack free superlattice structures. Even when there were no cracks in the case of the samples with AlGaN buffer, we observed a reduced electron mobility. This might be due to a reduced surface and material quality leading to increased surface and dislocation scattering, respectively.

This effect could be underlined by growing 5 couples of heterostructures with the same dimensions and doping level on a 2 μm thick GaN-layer. In that case the low temperature (77 K) mobility increased by a factor of 3 to a total value of 3425 cm^2/Vs, which is a sign for reduced dislocation scattering [5].

4. Conclusion

By using simulation software it was possible to determine the band structure of AlGaN/GaN modulation doped heterostructures. Due to the calculated carrier density distribution and estimated values for the electron mobility the lateral conductivity of superlattice structures could be determined. One optimum concerning the lateral conductivity found out by simulation was an AlGaN-layer thickness of $d_{AlGaN} = 12\,nm$, a GaN-layer thickness of $d_{GaN} = 8\,nm$ with an aluminium concentration $x \approx 25\,\%$.

After simulations first structures were grown by MOVPE. The dimensions of the layers were based on the simulation results. By Van-der-Pauw Hall measurement the conductivity was measured and the experimental data was compared to the simulation results. It could be demonstrated that the lateral conductivity can be increased by more than a factor of two compared to GaN-bulk material (Fig. 3).

References

[1] M. Grundmann, University of California, Santa Barbara, (http://my.ece.ucsb.edu/mgrundmann/bandeng.htm).

[2] M. Pophristic, S.P. Guo, and B. Peres, “High-conductivity n-AlGaN with high Al mole fraction grown by metalorganic vapor phase deposition”, *Appl. Phys. Lett.*, vol. 82, p. 4289, June 2003.

[3] M. Miyoshi, T. Egawa, H. Ishikawa, K.I. Asai, T. Shibata, M. Tanaka, and O. Oda, “Nanostructural characterization and two-dimensional electron-gas properties in high-mobility AlGaN/AlN/GaN heterostructures grown on epitaxial AlN/sapphire templates”, *Journal of Applied Physics*, vol. 98, p. 063713, 2005.

[4] S.P. Watkins, H.D. Cheung, G. Knight, G. Kelly, “Effect of interfacial dopant layer on transport properties of high purity InP”, *Appl. Phys. Lett.*, vol. 68, p. 1960, April 1996.

[5] S. Keller, G. Parish, P.T. Fini, S. Heikman, C.-H. Chen, N. Zhang, S.P. Den Baars and U.K. Mishra, “Metalorganic chemical vapor deposition of high mobility AlGaN/GaN heterostructures”, *Journal of Applied Physics*, vol. 86, p. 5850, November 1999.

Advanced Optically-Pumped Semiconductor Disk Lasers With Barrier and Quantum-Well Pumping

Frank Demaria, Michael C. Riedl, Fernando Rinaldi, Steffen Lorch, and Uwe Brauch*

Optically-Pumped semiconductor disk lasers with strain-compensated barrier-pumped InGaAs quantum-well based structures and in-well pumped GaAs quantum-well structures are presented. For the barrier-pumped structure with an emission wavelength of 975 nm, an optical output power of 5.1 W and a differential efficiency of 61 % is achieved. The in-well pumped structure shows a differential efficiency of 67 % and a near diffraction-limited output power of 1 W which was limited by the available optical pump power.

1. Introduction

In recent years, optically-pumped semiconductor disk lasers (OPSDLs) became a matter of particular interest in laser technology research. Common edge-emitting semiconductor lasers with multiple watt output powers suffer from poor spatial beam quality which arises from inevitable filamentation and the lack of transversal mode control. By contrast, due to the small longitudinal extent of their gain region and the adjustable external resonator, OPSDLs are laser sources which efficiently generate near diffraction limited, circular, non-astigmatic, multi-watt laser radiation [1, 2]. Because of the easily accessible high-finesse cavity, these lasers are predestinated for intra-cavity applications like second-harmonic generation of visible laser radiation [1, 3, 4] or intra-cavity spectroscopy [5].

Figure 1 shows the schematic arrangement and composition of an OPSDL. The resonator consists of an epitaxially grown distributed Bragg reflector and an external mirror. The Bragg reflector is designed to provide not only a high reflectivity of more than 99.9 % for the laser mode but also a high reflectivity for the pump beam to benefit from double-pass absorption. The optically active region is composed of a resonant gain structure, consisting of multiple quantum-wells, which are arranged in the antinodes of the laser mode. The quantum-wells are embedded in semiconductor material with a wider band gap. These spacer-layers provide the necessary energy barrier for the confinement of the carriers. Besides that, they also play an important role in the quite common method of barrier pumping. In this case, the generation of carriers by absorption takes place in the spacer-layers, thus spatially separated from the recombination by stimulated emission which is located in the quantum-wells. In a different approach, called in-well pumping, the carriers are straightforwardly generated within the quantum-well [6, 7]. In this report, results from devices following both approaches are presented.

*Institut für Strahlwerkzeuge (IFSW), University of Stuttgart

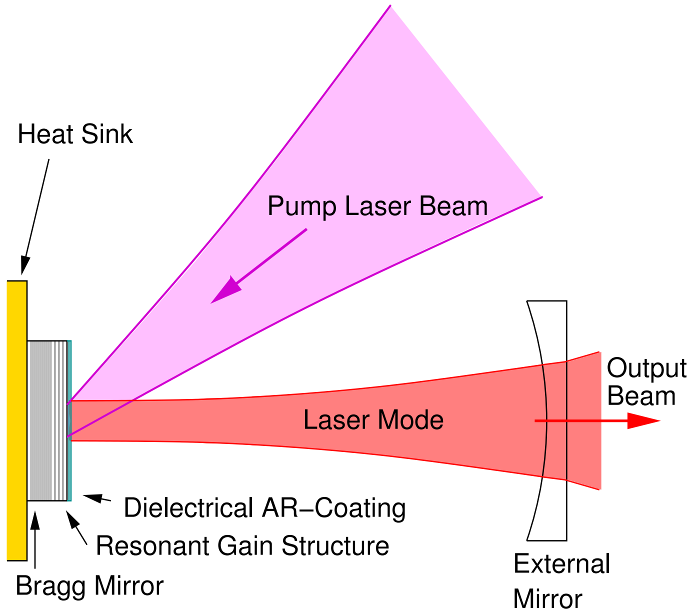

Fig. 1: Arrangement of an optically-pumped semiconductor disk laser. The epitaxially grown semiconductor disk conists of a resonant quantum-well gain structure and a distributed Bragg reflector. It is mounted onto a copper heatsink by indium soldering, its surface is passivated by a dielectrical coating.

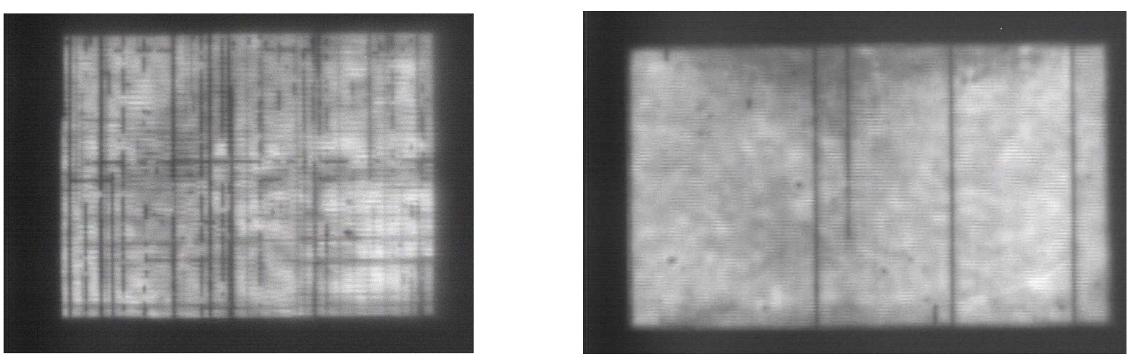

Fig. 2: Luminescence photography of an uncompensated structure (left) with an area of 1.5 mm × 2 mm and a strain-compensated structure with an area of 1.5 mm × 2.5 mm (right).

2. Barrier Pumped Structures

The barrier pumped structure whose results are subsequently presented contains an active region with six compressively-strained $In_{0.16}Ga_{0.84}As$ quantum-wells. One problem in the fabrication of strained multiple quantum-well devices is the accumulation of the elastic energy of the quantum-wells [8]. This leads to metastability and dislocations that result in the presence of dark lines in the spatially resolved photoluminescense photography as shown on the left-hand side of Fig. 2. For mode diameters with several hundreds of micrometers which are necessary for multi-watt output powers, it is inevitable to find such dark-lines within the pumped area resulting in a severe lowering of the efficiency, beam quality, and output power of the device. To overcome that, strain-compensated structures, containing tensilely strained $GaAs_{0.75}P_{0.25}$ layers are utilized [9]. The right-hand side of Fig. 2 shows the photoluminescence photography of such a structure with dark-line-free areas in the millimeter regime. The remaining dark lines can be interpreted as evidence for the presence of residual strain and incomplete strain compensation. Despite that, these devices revealed fairly good performance. Figure 3 shows the output characteristic

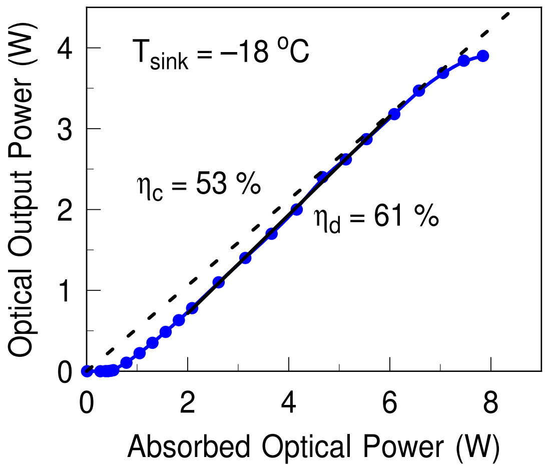

Fig. 3: Output characteristic of a strain-compensated disk laser with an emission wavelength of 974 nm. The maximum slope efficiency η_d is 61 %. At an optical output power of 3.5 W, the optical absorption-to-emisson efficiency η_c is 53 %.

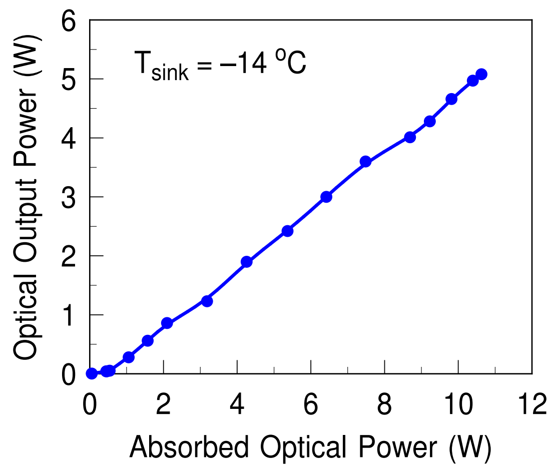

Fig. 4: Output characteristic of the same device as in Fig. 4. By optimization of the pump spot area for every measurement point an optical output power of over 5 W is achieved at a heatsink temperature of -14 °C.

of such a device with a differential efficiency η_d of 61 %. With an output wavelength of 975 nm and a pumping wavelength of 805 nm, the referring differential quantum efficiency is 74 %. The optical conversion efficiency η_c reaches its maximum of 53 % at an output power of 3.5 W. As customary, in Fig. 3 the optical output power is plotted over the absorbed optical power. From a physical point of view this makes quite sense, as only the absorbed fraction of the pump beam can contribute to the generation of carriers and heat. On the other hand this covers the fact that the actual optical power of the incident pump beam is considerably higher. The design of the structure presented here has been also optimized with respect to that. This has been done by means of a dielectrical coating to provide low reflectivities for the lasing mode as well as for the pump beam and by a Bragg mirror which exhibits not only a high reflectivity for the laser mode but also 93 % reflectivity for the pump beam. This design features led to absorptions from 85 % to 90 %. At an optical output power of 3.5 W the incident power was 7.6 W, from which a fraction of 1 W was reflected. From that, an absorption efficiency of 87 % and an optical power efficiency with respect to thee incident pump power of 46 % can be deduced.

In the measurement presented in Fig. 4, the pump-spot area was increased with increasing pump powers. By that way, a better heat flux and better cooling made an optical output power of 5.1 W possible. For every measurement point in the graph, the resonator geometry was optimized. In both measurements the disk laser chip was soldered with indium onto a simple copper heat-spreader which in turn was screwed to an actively peltier-cooled heatsink. The highest efficiencies and output powers have been achieved for a heat-sink temperature of -18 °C and -14 °C, respectively, with an external mirror reflectivity of 98 %. The mirrors radius of curvature was -100 mm. The pump beam was provided by fiber-coupled broad-area laser diodes, the pump angle was 23° with respect to the resonator's optical axis.

3. In-Well Pumped Structures

In-well pumping allows a considerably smaller energy difference between the pump radiation and the emitted laser-mode. This results in a smaller correspondig quantum-defect. Generally, the quantum-defect leads inevitably to a constant thermal dissipation loss which limits the lasers efficiency. Thus, higher efficiencies can be predicted for in-well pumping. As a disadvantage, in comparison to barrier pumping, the constructive requirements for in-well pumped structures are more demanding. The lower absorptance of the quantum-wells and the smaller sprectral acceptance have to be taken into account. Resonant pumping is a quite effective way to increase the absorptance, this in turn requires deliberately choice of the quantum-wells positions, the design of a microcavity in the disk, and the exact choice of the pump-wavelength and pump-angle. In contrast to barrier

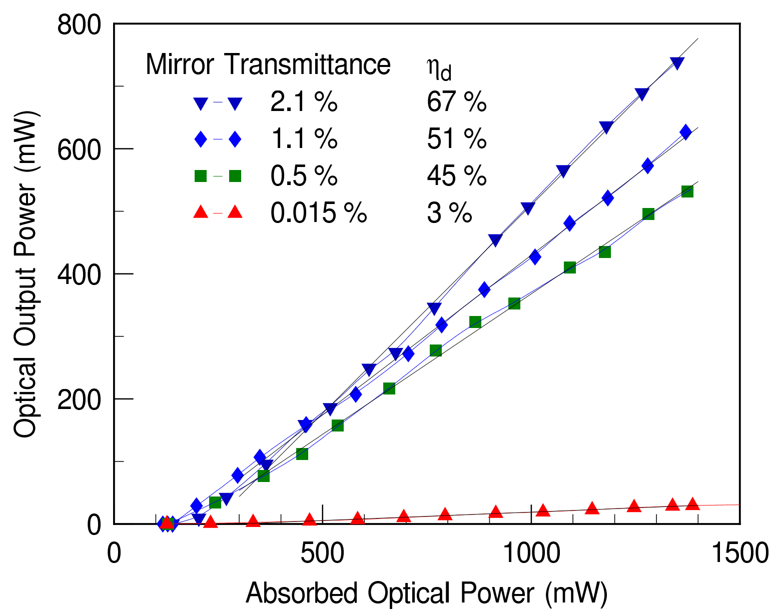

Fig. 5: Optical output characteristics of an in-well pumped disk laser. The structure is pumped at 833 nm under an angle of 70 ° with an s-polarized beam. The measurement was performed at a heatsink-temperature of 20 °C, where the laser emission wavelength was 865 nm.

pumped structures, the dielectrical coating has to be designed to provide a well-suitable reflectivity to form an adequate microcavity for the pump beam. Figure 5 presents output characteristic measurements for such a structure with 12 quantum-wells which have been performed at the *Institut für Strahlwerkzeuge (IFSW)* at the *University of Stuttgart*. For a 98 %-reflectivity outcoupling mirror, a differential efficiency of 67 % and a maximum conversion efficiency of 55 % were achieved. The pumping beam of 833 nm was provided

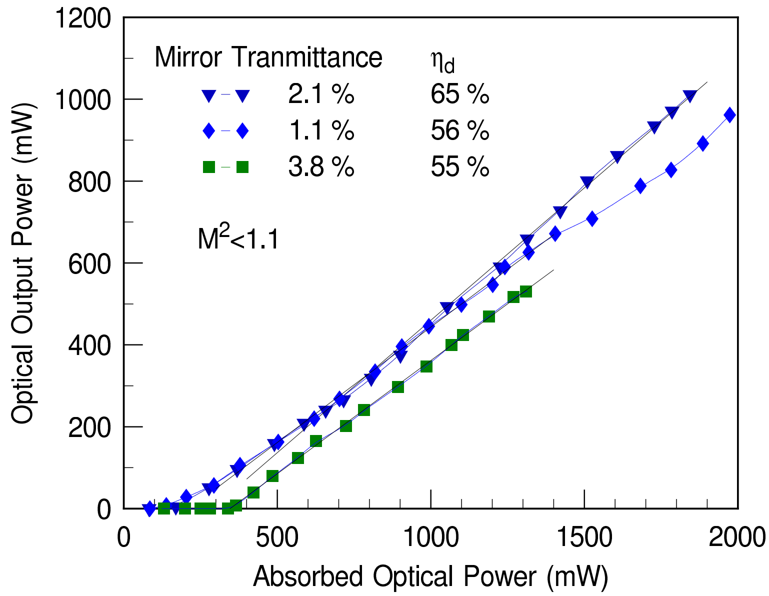

Fig. 6: Optical output characteristics of the same sturcture as in Fig. 5 with optimized pump-absorption. At the maximum optical output power of 1 W, a diffraction number $M^2 < 1.1$ was measured.

by a titanium-sapphire laser. Its incident angle was 70° to the normal, s-polarzation was chosen. Under these conditions, the calculated reflectivity of the input mirror, formed by the surface of the semiconductor and a 3-layer dielectrical coating is 76.4 %. For this value, quite effective absorption of 45 % takes place. With increasing input powers, the structure is heated up and the pump-resonance wavelength shifts to longer wavelengths. In the measurement represented in Fig. 6, this was taken into account by adjusting the pump-lasers wavelength. As a result, an absorption of 55 % and an output power of 1 W with a diffraction number of $M^2 < 1.1$ was achieved. The emission wavelength of 865 nm was 10 nm higher than intended. From that, the differential quantum efficiency is calculated as 70 %. All the measurements took place at a temperature of 20 °C.

4. Conclusion

A barrier pumped semiconductor disk lasers with 5.1 W optical output power, a differential efficiency of 61 % and a quantum efficiency of 74 % at a wavelength of 975 nm was presented. An antireflective coating and a Bragg mirror design which provides also high reflectivities for the pump beam leads to high pump-radiation absorptance values between 85 % and 90 %.

The potential of in-well pumping was demonstrated by the 865 nm laser emission of a resonance-pumped structure with 12 quantum-wells. Its output characteristics revealed a high differential efficiency of 67 % and a differential quantum efficiency of 70 % at room temperature. The nearly diffraction-limited beam with a maximum optical output power of 1 W and a diffraction-number of $M^2 < 1.1$ was limited in output power by the available optical pump power. No thermal roll-over was observed.

References

[1] J. Chilla, S. Butterworth, J. Charles, A. Capra, M. Reed, and L. Spinelli, "High power optically pumped semiconductor lasers," *Proc. SPIE*, vol. 5332, pp. 143–150, 2004.

[2] S. Lutgen, T. Albrecht, P. Brick, W. Reill, J. Luft, and L. Spinelli, "8-W high-efficiency continuous-wave semiconductor disk laser at 1000 nm," *Appl. Phys. Lett.*, vol. 82, no. 21, pp. 3620–3622, 2003.

[3] E. Schiehlen, M. Golling, and Peter Unger, "Diode-pumped semiconductor disk laser with intracavity frequency doubling using lithium tiborate (LBO)," *IEEE Photon. Technol. Lett.*, vol. 14, no. 6, pp. 777–779, 2002.

[4] E. Gerster, I. Ecker, S. Lorch, C. Hahn, S. Menzel, and P. Unger, "Orange-emitting frequency-doubled AsAsSb/GaAs semiconductor disk laser," *J. Appl. Phys.*, vol. 94, no. 12, pp. 7397–7401, 2003.

[5] A. Garnache, A. Kachanov, F. Stoeckel, and R. Houdre, "Diode-pumped broadband vertical-external-cavity surface-emitting semiconductor laser applied to high-sensitivity intracavity absorption spectroscopy ," *J. Opt. Soc. Am. B*, vol. 17, pp. 1589–1598, 2000.

[6] S.-S. Beyertt, M. Zorn, T. Kübler, H. Wenzel, M. Weyers, A. Giesen, G. Tränkle, and U. Brauch, "Optical in-well pumping of a semiconductor disk laser with high optical efficiency," *IEEE J. Quantum Electron.*, vol. 41, no. 12, pp. 1439–1449, 2005.

[7] A. Giesen, "Results and scaling laws of thin disk lasers," *Proc. SPIE*, vol. 5332, pp. 143–150, 2004.

[8] I. J. Fritz, S. T. Picraux, L. R. Dawson, and T. J. Drummond, "Dependence of critical layer thickness on strain for $In_xGa_{1-x}As/GaAs$ strained-layer superlattices," *Appl. Phys. Lett.*, vol. 46, no. 10, pp. 967–969, 1985.

[9] D. C. Houghton, M. Davies, and M. Dion, "Design criteria for structurally stable, high strained multiple quantum well devices," *Appl. Phys. Lett.*, vol. 64, no. 4, pp. 505–507, 1993.

Applications of Optical Coatings

Steffen Lorch

Optical coatings have a wide range of applications in optoelectronics. Especially semiconductor edge-emitting lasers need coatings for adjusting the facet reflectivity and for passivation. Two applications on edge emitters will be presented here. First, the passivation to increase the level of the COMD (Catastrophically Optical Mirror Damage) will be discussed. The second application is the manipulation of the fast-axis far field by coatings with strong incident-angle dependent facet reflectivities.

1. Introduction

In optoelectronics, optical coatings are needed for a lot of functions. Especially semiconductor edge-emitting lasers are normally not used without coatings. After cleaving the laser, the created resonator has two facets with equal facet reflecitvities. The facets are coated to change their reflectivity. The output facet normally is coated with an antireflective (AR), the rear facet with an multi-layer high-reflective (HR) coating. With such an AR/HR coating, it is achived that nearly the whole power is transmitted through the output facet. The ratio of the output power of both facets P_{AR} and P_{HR} is dependent on the facet reflectivities R_{AR} and R_{HR} and can be calculated with [1]

$$\frac{P_{\mathrm{AR}}}{P_{\mathrm{HR}}} = \frac{\sqrt{R_{\mathrm{HR}}}\,(1 - R_{\mathrm{AR}})}{\sqrt{R_{\mathrm{AR}}}\,(1 - R_{\mathrm{HR}})} \,. \tag{1}$$

Not only the adjustment of the reflectivities is an important function of coatings, but also the passiavation of the laser facets. At high output power, the facets can be destroyed by the Catastrophically Optical Mirror Damage (COMD). With a coating, the facets are passivated and the maximum COMD level is increased. Also the far-field distribution can be manipulated with coatings that have highly angle-dependent reflecitvities.

2. COMD

For the application of lasers, life time is an important factor. The life time and the maximum output power are influenced by the degradation of the laser facet. The most important factor of the facet degradation is the Catastrophically Optical Mirror Damage (COMD). Due to surface states, facet oxidation, and change in the tension of the quantum wells, the band gap is reduced at the surface. Because of this reduction, more light is absorbed, carriers are generated, and recombine nonradiativly. This creates heat in the facet region which results in further band-gap reduction. This feedback loop ends at a temperature that melts the semicoductor material and the facet is destroyed. In Fig. 1, SEM pictures of facets of ridge-waveguide lasers are shown; on the left-hand side, a cleaved facet with no damage, in the middle, a cleaved facet with a COMD defect, and on the right-hand side, a coated facet also with a COMD defect.

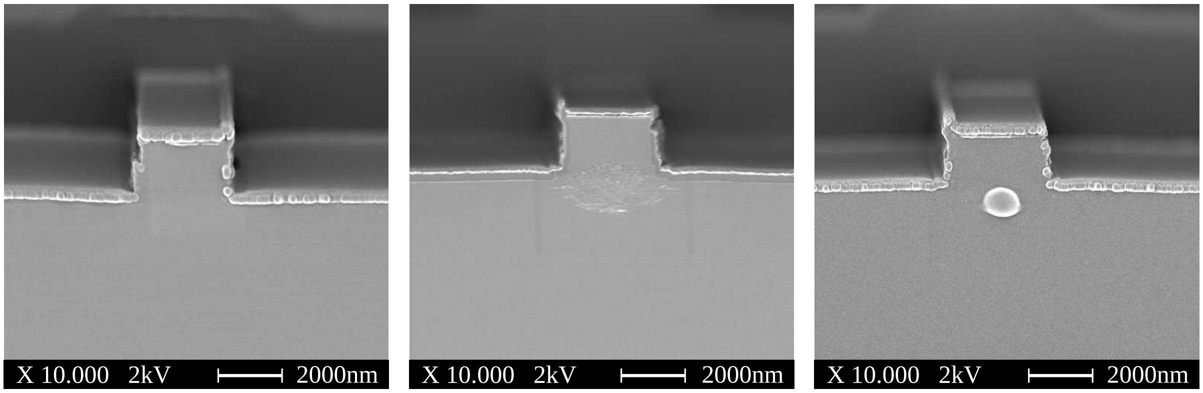

Fig. 1: SEM pictures of the output facets of ridge-waveguide edge-emitting lasers. Left is a cleaved facet, middle a cleaved facet with COMD, and right coated facet with COMD.

The maximum COMD level depends on the light power that is responsible for the absorption. This power is not the measurable power outside the laser P_{out}, it is the power that reaches the facet from the inside, which is the internal power P_{int} plus the reflected power P_{refl}. Thus the internal power depends on the facet reflectivity and can be calculated by [2]

$$\frac{P_{\mathrm{int}}}{P_{\mathrm{out}}} = \frac{1+R}{1-R} \,. \tag{2}$$

To examine the influence of coatings on the COMD level, laser bars with ridge-waveguide lasers and different ridge widths between 2.5–6.0 μm have been used. The laser bars have been coated with one layer of 80 nm Al_2O_3 on both facets. With such a thickness, the facet reflectivity decreases from $R = 0.3$ to $R^* = 0.17$ which results in a shift in the laser threshold current of $I^*_{\mathrm{th}} = 1.18 \cdot I_{\mathrm{th}}$ and an internal power of $P_{\mathrm{int}} = 1.4 \cdot P_{\mathrm{out}}$. The coatings have been realized with an ion-beam sputter deposition system using an ion-beam current of $I_{\mathrm{B}} = 60\,\mathrm{mA}$ and an ion energy of $U_{\mathrm{B}} = 1000\,\mathrm{V}$. To achieve a high maximum output power, the laser facets can be pre-cleaned by an ion beam. To determine the optimum ion energy, different pre-cleaning processes ($t = 20\,\mathrm{s}$) with subsequent coating have been performed. In Fig. 2, L–I-curves are shown. The laser with cleaved facets shows an increase of the power with increasing current until the power drops at 220 mW. This is the point where COMD takes place. For the laser with both facets coated, the maximum power can be increased to 300 mW. The highest maximum output power of 380 mW shows the laser with the pre-cleaning process before coating.

In Fig. 3, all results are shown. To compare the lasers with different ridge widths, one has to switch from the output power to the power density. For the lasers with the cleaved facets a maximum output power density of approximately 8 MW/cm^2 can be achieved.

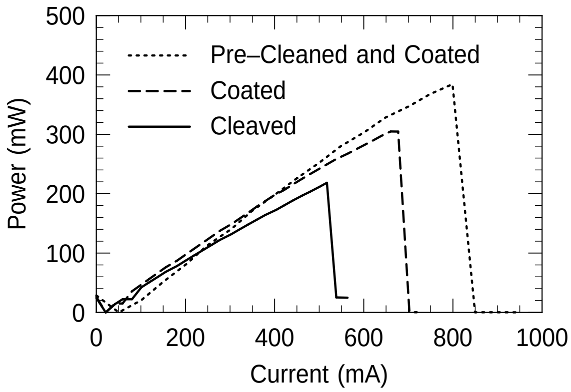

Fig. 2: *L–I*-Curves until COMD for different laser facet preparation.

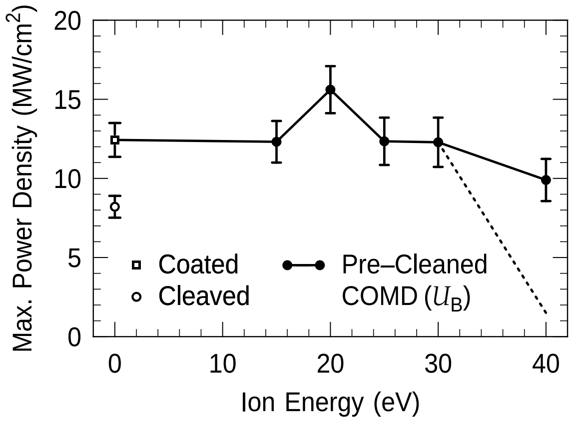

Fig. 3: Power density for the COMD level dependent of the ion energy of the pre-cleaning process.

With a coating on both facets and no pre-cleaning process, the value can be increased to 12 MW/cm^2. The curve in Fig. 3 shows the maximum power density dependent of the ion energy of the pre-cleaning process. It can be seen that there is no significant change in the values for low energies. The sputter energy is not high enough to remove the oxide from the facets. At 20 eV, the best value is achieved with a power density of approximately 16 MW/cm^2. With higher ion energies, the values decrease again due to the higher damaging on the facets by the ions. Above 30 eV, nearly all lasers have been destroyed, only a few have shown lasing behavior. So an optimum for the pre-cleaning ion energy has been found to be 20 eV. In Tab. 1, the results of the passivation experiments are compiled. For that, the internal maximum power densities should be used do get reasonable values to be compared. With coatings on the facets, the COMD level can be increases by 14.5 %. Using a pre-cleaning process with an ion energy of 20 eV and a coating the COMD level reaches 43.4 % higher power densities compared to the cleaved lasers.

(MW/cm^2)	P_{out}/A	P_{int}/A	Advance
Cleaved facet	8.2 ± 0.7	15.2 ± 1.3	—
Coated facet	12.4 ± 1.1	17.4 ± 1.5	14.5 %
Pre-Cleaned (20 eV)	15.6 ± 1.5	21.8 ± 2.1	43.4 %

Tab. 1: Summary of the results of the passivation coatings on laser facets to increase the COMD level.

There are a lot of other methodes combined with coatings to increase the COMD level. The cleaving of the facets can be done in vacuum to prevent oxidation [3]. The guiding of the mode can be changed to reach lower power densities on the facet [4]. The pretreatment of the facets can be done in different ways [5]–[9]. A new and promising methode is to clean the surface with an ion beam and to passivate the surface with a nitrogen plasma (Nitrel-Process [10]).

3. Manipulation of the fast-axis far field

Another application of coatings is the manipulation of the fast-axis far field. This can be done, if the coating has a reflectivity that is strongly dependent on the incident angle [11]. The intensity distribution of a laser beam in any plane can be calculated by a Fourier transformation from the spatial distribution to the angular distribution [12]. The spatial distribution in the near field is Gaussian-like and so the angular distribution has to be Gaussian-like too. Due to the much higher far-field angle in the fast axis of an edge-emitting laser, the manipulation of the far-field distribution is much higher in this direction, so the s-polarisation should be taken into account. In Fig. 4, the facet reflectivity over the incident angle is shown. For a cleaved facet, the reflectivity of 0.3 does not change significantly with the angle. The dashed curve shows a reflectivity that decreases strongly with incident angle (wide), the dotted curve in contrast shows the opposite, with increasing angle the facet reflectivity increases (narrow).

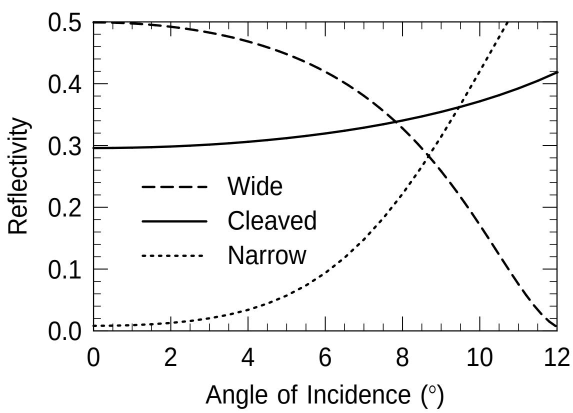

Fig. 4: Facet reflecitvity over the incident angel for a cleaved laser and two different four-layer coatings (s-polarisation).

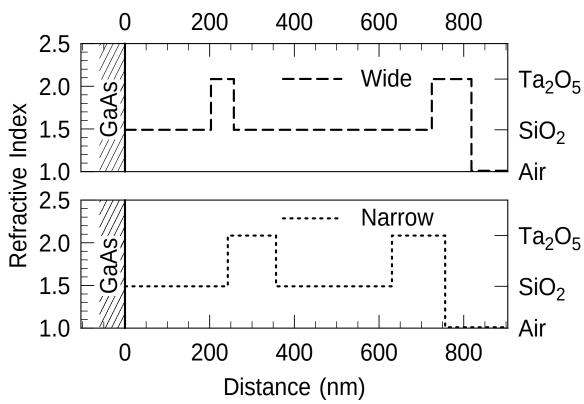

Fig. 5: Refractive index over the distance from the facet for two different far-field manipulating coatings.

To achieve such strong angle-dependent reflecitvities, four-layer coatings with Ta_2O_5 and SiO_2 have been used. In Fig. 5, the refractive index over the distance is depicted. Both coatings have a complete thickness of approximately 800 nm. By the wide coating (decreasing reflectivity with increasing angle) the intensity for higher incident angles will not be reflected as much as the intensity for lower angles. Therefore the transmitted light should have a higher intensity for higher angles compared to cleaved facets. With the narrow coating (increasing reflecitvity with increasing angle), more light with lower angles will be transmitted compared to the light with higher angles. Therefore the light should show a narrow intensity distribution. In Fig. 6, the measured intensities for the different coatings are shown. The intensity of the cleaved laser has a $1/e^2$ width of 68.2° (see also Tab. 2). With the wide coating, the width of the far-field angle has been increased to 84.7°, the narrow coating has decreased the width to 57.8°.

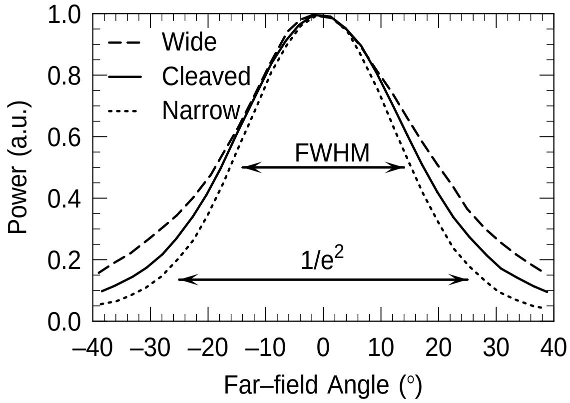

Fig. 6: Far-field distribution of lasers with cleaved facets and two different coatings.

	$1/e^2$ (°)	FWHM (°)
Wide - - - - -	84.7 ± 1.8	39.7 ± 1.7
Cleaved ——	68.2 ± 2.4	35.5 ± 1.3
Narrow ········	57.8 ± 1.5	32.4 ± 1.0

Tab. 2.: Summary of the results of the far-field manipulating coatings.

This results show, that it is possible to significantly influence the fast-axis far-field distribution of a laser beam with coatings. Especially the decrease of the far-field angle is an important application. Due to the broad angular distribution of light of edge-emitting lasers, the focusing is only possible using lenses of high numerical aperture. With such a coating to decrease the far-field angle, the demands made on focusing lens systems can be simpler. It should be also possible to achieve higher far-field angle decreases with the use of coatings with much stronger angle-dependent reflecitvities. For that, more layers than four have to be used.

4. Conclusion

Optical coatings on facets of edge-emitting lasers cannot be used only to adjust the facet reflectivities. One main task is the passivation of the laser facets to prevent the destruction by COMD. With a coating and a pre-cleaning process, the maximum output intensity level can increased by 43 %. It is also possible to influence the intensity distribution of the output power. With coatings having angle-dependent reflectivities, the far-field angle in the fast axis can be increased and decreased. It was possible to decrease the $1/e^2$ width of the far-field angle by 15.2 % which reduces the requirements on the focusing lens system.

References

[1] W.A. Hamel, M. Babeliowsky, J.P. Woerdman, and G.A. Acket, “Diagnostic of asymmetrically coated semiconductor lasers,” *IEEE Photon. Technol. Lett.*, vol. 3, no. 7, pp. 600–602, 1991.

[2] A. Moser, “Thermodynamics of facet damage in cleaved AlGaAs lasers,” *Appl. Phys. Lett.*, vol. 59, no. 5, pp. 522–524, 1991.

[3] L.W. Tu, E.F. Schubert, M. Hong, and G.J. Zydzik, "In-vacuum cleaving and coating of semiconductor laser facets using thin silicon and a dielectric," *J. Appl. Phys.*, vol. 80, no. 11, pp. 6448–6451, 1996.

[4] P.W. Epperlein and G.L. Bona, "Influence of the vertical structure on the mirror facet temperatures of visible GaInP quantum well lasers," *Appl. Phys. Lett.*, vol. 62, no. 24, pp. 3074–3076, 1993.

[5] P. Collot, S. Delalande, and J. Olivier, "Sulphur passivation of dry-etched AlGaAs laser facets," *Electron. Lett.*, vol. 35, no. 6, pp. 506–508, 1999.

[6] A.J. Howard, C.I.H. Ashby, J.A. Lott, R.P. Schneider, and R.F. Corless, "Electrochemical sulfur passivation of visible ($\sim$670 nm) AlGaInP lasers," *J. Vac. Sci. Technol. A*, vol. 12, no. 4, pp. 1063–1067, 1994.

[7] G. Beister, J. Maege, D. Gutsche, G. Erbert, J. Sebastian, K. Vogel, M. Weyers, J. Würfl, and O.P. Daga, "Simple method for examining sulphur passivation of facets in InGaAs–AlGaAs ($\lambda = 0.98\,\mu$m) laser diodes," *Appl. Phys. Lett.*, vol. 68, no. 18, pp. 2467–2468, 1996.

[8] J.S. Yoo, H.H. Lee, and P. Zory, "Enhancement of output intensity limit of semiconductor lasers by chemical passivation of mirror facets," *IEEE Photon. Technol. Lett.*, vol. 3, no. 3, pp. 202–203, 1991.

[9] W.C. Tang, E.H. Altendorf, H.J. Rosen, D.J. Webb, and P. Vettiger, "Lifetime extension of uncoated AlGaAs single quantum well lasers by high power burn-in in inert atmospheres," *Electron. Lett.*, vol. 30, no. 2, pp. 143–145, 1994.

[10] A. Feitisch, "Ion beams enhance optoelectronic durability," *Opto & Laser Europe*, vol. 130, pp. 20–21, 2005.

[11] R.R. Drenten, W. van Es-Spiekman, and C.J. van der Poel, "Semiconductor laser far-field shaping by means of an angle-selective facet coating," *Appl. Optics*, vol. 30, no. 27, pp. 3846–3851, 1991.

[12] A.E. Siegman, "Defining the effective radius of curvature for a nonideal optical beam," *IEEE J. Quantum Electron.*, vol. 27, no. 5, pp. 1146–1148, 1991.

Monolithically Integrated GaAs-Based Transceiver Chips for Bidirectional Optical Data Transmission

Martin Stach and Fernando Rinaldi

We report on the design, fabrication and test results of monolithically integrated transceiver chips consisting of GaAs metal–semiconductor–metal photodiodes and 850 nm wavelength vertical-cavity surface-emitting lasers. These chips are well suited for low-cost and compact bidirectional optical interconnection at Gbit/s data rates in mobile systems and industrial or home networks employing large core size multimode fibers.

1. Introduction

A monolithically integrated transceiver (Tx/Rx) chip which operates at 850 nm wavelength and consists of a vertical-cavity surface-emitting laser (VCSEL) and a directly adjacent metal–semiconductor–metal photodiode (MSM PD) is presented. The chip introduced in [1] for the first time with an extended dynamic characterization in [2] is specifically adapted to 200 µm core diameter step-index polymer-clad silica (PCS) fibers while avoiding any light coupling optics. The fiber overfilled launch bandwidth–length product of $3\,\mathrm{GHz} \cdot \mathrm{m}$ enables Gbit/s data rate connectivity over meter-long distances in half-duplex mode. The steps required to fabricate the transceiver chips are described and back-to-back (BTB) data transmission up to 3 Gbit/s data rate is performed to demonstrate basic dynamic capabilities. Several other concepts involving either the integration of VCSEL and photodetector or bidirectional optical interconnection have been reported in the literature. The work on integrated smart pixels usually targeted free-space unidirectional transmission. For this purpose, spatially separated VCSELs and photodiodes were implemented on the same chip [3, 4]. Half-duplex interconnection using a single VCSEL has been demonstrated [5]. Unfortunately such a solution is not well suited for low-cost links owing to small detection areas and resonant detection which would require temperature control at both fiber ends. In [6] a hybrid solution for bidirectional operation over a PCS fiber is reported, making use of a polymer waveguide platform and 90° beam deflection in the VCSEL path. The present work combines individual advantages of previous approaches, namely monolithic integration, large-area non-resonant detection, and fiber butt-coupling.

2. Chip Processing

A monolithically integrated transceiver chip must contain all layers necessary for signal generation and reception. As illustrated in Fig. 1, the layers for the receiving MSM PD are epitaxially grown (by molecular beam epitaxy) on top of the VCSEL layers.

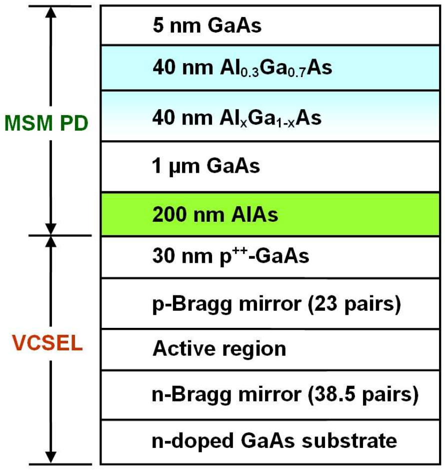

Fig. 1: Layer structure of the transceiver chips.

A 200 nm-thick AlAs layer serves as an etch stop and a barrier for the photo-generated carriers. The generation of the electron–hole pairs takes place in an undoped 1 µm-thick GaAs layer suitable for light detection at 850 nm wavelength. This layer is separated from a dark current-reducing 40 nm $Al_{0.3}Ga_{0.7}As$ Schottky barrier by a 40 nm $Al_xGa_{1-x}As$ layer (linearly graded from $x = 0$ to 0.3) to minimize the energy band discontinuity which could hinder the transport of the light-induced carriers. The top GaAs layer serves as a protection layer to prevent $Al_{0.3}Ga_{0.7}As$ oxidation. The aforementioned layer structure is similar to the one introduced in [7].

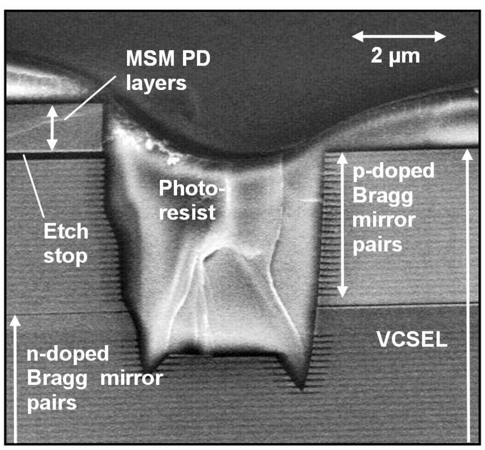

Fig. 2: Scanning electron micrograph showing a cross-sectional view after dry-etching of the VCSEL mesa.

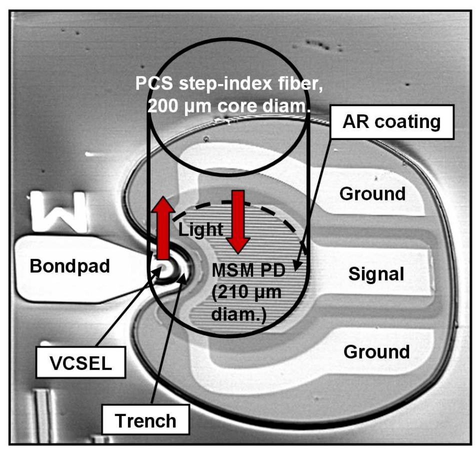

Fig. 3: Scanning electron micrograph of a Tx/Rx chip with a schematic butt-coupled PCS fiber as an application example.

To access the highly p-doped cap layer of the VCSEL, the detector layers surrounding the resist-protected photodiode area are selectively removed by citric acid solutions. The process is terminated at the AlAs etch-stop layer which is subsequently removed by hydrofluoric acid. A dry-etch process is applied to define the VCSEL mesa, during which the photodiode is protected by photoresist. Figure 2 shows a cross-sectional view of the trench region (see also Fig. 3) between VCSEL and MSM PD and illustrates the layer structure. The trench is filled by a high-resolution UV-sensitive photoresist which is employed to realize MSM electrodes with various interdigital spacings down to 2 µm. Subsequently, a single Al_2O_3 quarter-wave antireflection (AR) coating is applied and photolithographic steps are performed to put bondpads on the surface, thus allowing wire bonding for dynamic characterization. The PD diameter equals 210 µm, matching the 200 µm core diameter of the PCS fiber that shall be centered in front of the transceiver chip (Fig. 3). The VCSEL occupies part of the circular-like PD area, where the PD-to-VCSEL offset is a trade-off between coupling efficiency and remaining detector area.

3. Test Results

Small-signal operation shows that Tx/Rx chip photodiodes with a diameter of 210 µm and a finger width-to-spacing ratio of 1-to-2 µm have a 3 dB cut-off frequency of 1.4 GHz at 4 V bias voltage. At the operating wavelength of 850 nm, the responsivity is as high as 0.4 A/W due to the enhancements by light reflection at the VCSEL layers and by the AR coating which also passivates the surface and thus reduces the dark current. The quantum efficiency equals 59 % which is close to the theoretical maximum of 67 % taking shadowing by the given electrode configuration into account. The transmitting part of the Tx/Rx chips consists of a standard top-emitting oxide-confined VCSEL operating at 850 nm. Its n-contact is located at the bottom of the GaAs substrate. The laser 3 dB bandwidth exceeds 5 GHz, as determined with a multimode fiber-pigtailed InGaAs pin-photoreceiver with above 8 GHz bandwidth. Thus the available bandwidth of the transceiver chips is limited by the MSM PDs.

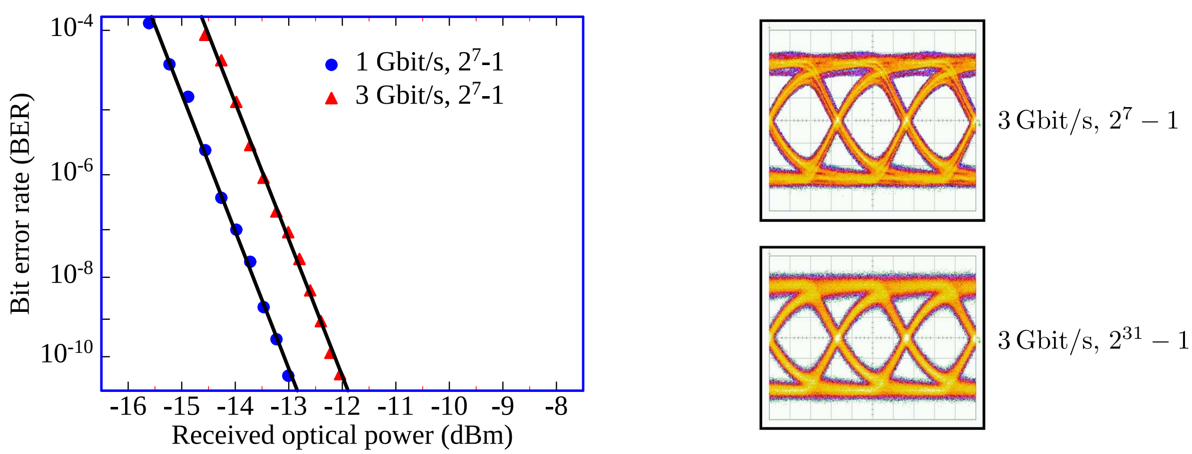

Fig. 4: Back-to-back (BTB) data transmission of NRZ PRBS signals between 210 µm diameter PD and VCSEL as parts of monolithically integrated Tx/Rx chips (left) and comparison of eye diagrams recorded for different word lengths at 3 Gbit/s data rate (right).

In Fig. 4, back-to-back (BTB) data transmission between two Tx/Rx chips without inserting a bandwidth-limiting fiber is demonstrated. One VCSEL is modulated with a non-return-to-zero pseudo-random bit sequence (NRZ PRBS) with $2^7 - 1$ word length and its light is imaged with a magnification of 1.6 onto the opposite PD using two lenses. The received optical power at a bit error rate of 10^{-11} amounts to -12.8 and -11.9 dBm for 1 and 3 Gbit/s data rate, respectively (Fig. 4, left). Figure 4 on the right hand side shows that the eye opening at 3 Gbit/s is only slightly reduced at $2^{31} - 1$ word length compared to $2^7 - 1$.

4. Conclusion

We have fabricated monolithically integrated transceiver chips for high-speed optical interconnection over a butt-coupled 200 µm core diameter PCS fibre at 850 nm wavelength. Quasi error-free data transmission at 3 Gbit/s data rate has been shown in a back-to-back configuration. By reducing the device dimensions, this approach should even allow to use graded-index fibres with smaller core and significantly larger bandwidth–length product which would enable Gbit/s-range data transmission over distances relevant for industrial and home networks.

References

[1] M. Stach, L. Stöferle, F. Rinaldi, and R. Michalzik, "Monolithically integrated optical transceiver chips at 850 nm wavelength consisting of VCSELs and MSM photodiodes" (invited), in Proc. (CD ROM) *Conf. on Lasers and Electro-Optics Europe, CLEO/Europe 2005*, paper CI2-4-THU. Munich, Germany, June 2005.

[2] M. Stach, L. Stöferle, F. Rinaldi, and R. Michalzik, "3 Gbit/s data transmission with monolithically integrated optical transceiver chips for very short reach applications," in Proc. *31st Europ. Conf. on Opt. Commun., ECOC 2005*, vol. 3, pp. 529–530. Glasgow, Scotland, UK, Sept. 2005.

[3] Y. Liu, E.M. Strzelecka, J. Nohava, M.K. Hibbs-Brenner, and E. Towe, "Smart-pixel array technology for free-space optical interconnects," *Proc. IEEE*, vol. 88, no. 6, pp. 764–768, 2000.

[4] K.M. Geib, K.D. Choquette, D.K. Serkland, A.A. Allerman, and T.W. Hargett, "Fabrication and performance of two-dimensional matrix addressable arrays of integrated vertical-cavity lasers and resonant cavity photodetectors," *IEEE J. Select. Topics Quantum Electron.*, vol. 8, no. 4, pp. 943–947, 2002.

[5] M. Dragas, I.H. White, R.V. Penty, J. Rorison, P.J. Heard, and G. Parry, "Dual-purpose VCSELs for short-haul bidirectional communication links," *IEEE Photon. Technol. Lett.*, vol. 11, no. 12, pp. 1548–1550, 1999.

[6] T. Kibler, K. Pregitzer, C. Rief, E. Zeeb, A. Neyer, and O.S. Kaiser, "Optical transceiver module for star networks in cars," in *VCSELs and Optical Interconnects*, H. Thienpont, J. Danckaert (Eds.), Proc. SPIE 4942, pp. 54–62, 2003.

[7] V. Hurm, W. Bronner, W. Benz, K. Köhler, J.-R. Kropp, R. Lösch, M. Ludwig, G. Mann, M. Mikulla, J. Rosenzweig, M. Schlechtweg, M. Walther, and G. Weimann, "Large area MSM photodiode array for 0.85 μm wavelength 10 Gbit/s per channel parallel optical links," *Electron. Lett.*, vol. 38, no. 18, pp. 1051–1052, 2002.

VCSEL Arrays With Redundant Pixel Designs for 10 Gbit/s 2-D Space-Parallel MMF Transmission

Hendrik Roscher

We demonstrate two-dimensional (2-D) flip-bonded 850 nm VCSEL arrays with three close-spaced lasers per channel equally butt-coupled to the same 50 µm core diameter fiber for improved transceiver lifetimes. Quasi error-free 10 Gbit/s signals are transmitted over 500 m of multimode fiber (MMF) under offset launch.

1. Introduction

The direct modulation bandwidth of VCSELs limits serial bit rates to about 20 Gbit/s. Their particular capacity for very high-speed data transmission lies rather in an outstanding integrability making possible the realization of large two-dimensional (2-D) arrays with a large number of simultaneously operated transmit channels, densely packed within a small footprint. As a consequence, the VCSEL count in very high-speed datacom scenarios can be expected to rapidly multiply in the years ahead. VCSEL reliability is thus pivotal for critical applications.

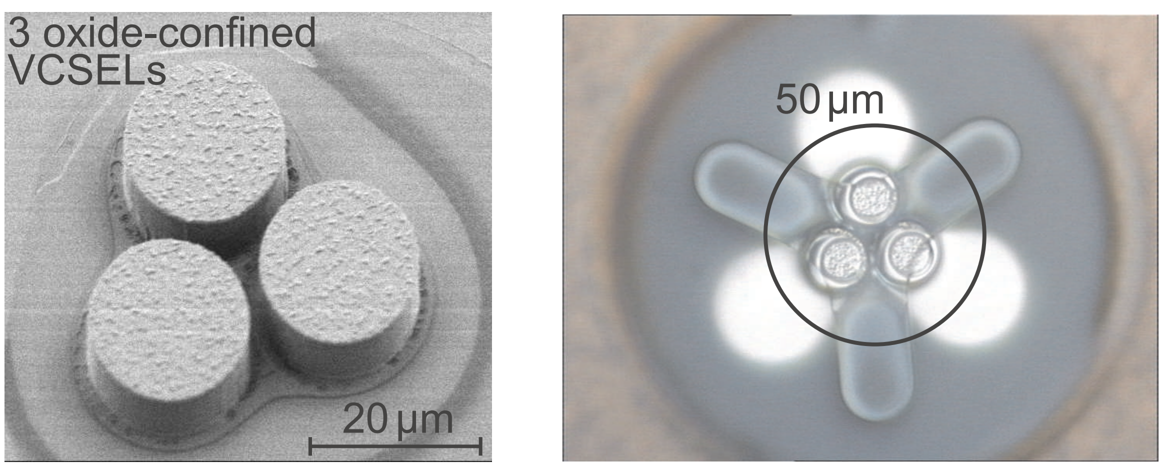

Fig. 1: Epitaxial-side views of three mesa-isolated oxide-confined VCSELs in one channel. Self-aligned p-contacts after mesa dry etching *(left)*. Laser position with respect to the MMF core diameter permits butt coupling with high coupling efficiency *(right)*.

The so-called bathtub curve [1] describes how the probability of failure (or failure rate) develops for a population of devices in the cause of their lifetime. After an initial phase, during which early failures are screened out and the failure rates rapidly drop, a steady state of lowest and nearly constant failure rate is reached. Today's oxide-confined VCSELs possess life spans of around 100 years even at elevated temperatures [2]. However, during this extended period there exists a finite probability for the devices to stop functioning at any point in time. This residual probability of premature failure multiplies with the number of VCSELs in use. It is hence considered a significant constraint for critical applications involving many parallel data channels, each relying on a single VCSEL.

We propose a novel scheme of VCSEL redundancy in each channel where two backup lasers are retained for each multimode fiber to prevent channel outages caused by singular random VCSEL failures. Three direct-mesa flip-bonded VCSELs on record-small VCSEL-to-VCSEL pitches butt-couple to the same 50 µm core diameter graded-index multimode fiber (50MMF) eliminating the need for elaborate beam combining optics, and hence keeping systems simple and cost-effective.

2. Redundant VCSEL Arrays

High-density VCSEL integration was enabled by a dry etch process utilizing the p-contact metallization as the etch mask. In order to test the technological feasibility, the dimensions of the VCSEL triples (see Fig. 1) were varied from channel to channel within the 4×4 channels of each array. The triples of mesa-isolated oxide-confined VCSELs within one array have outer mesa diameters ranging from 19 to 12 µm. Each VCSEL has a self-aligned full-size p-contact which is present during high-temperature wet oxidation. Mesa separations as small as 1.5 µm and oxidation lengths below 3.5 µm enabled, to our knowledge, the highest integration density of oxide-confined VCSELs ever achieved to date with true VCSEL-to-VCSEL pitches that are only 9 µm larger than the active diameters.

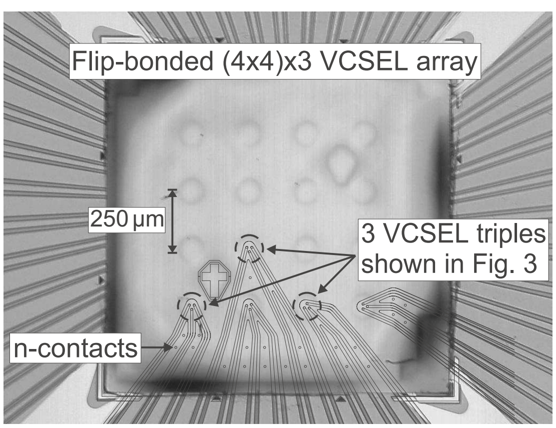

Fig. 2: Photo of flip-bonded $(4 \times 4) \times 3$ array with three close-spaced VCSELs per cell overlaid by schematics showing the routing of some of the coplanar lines.

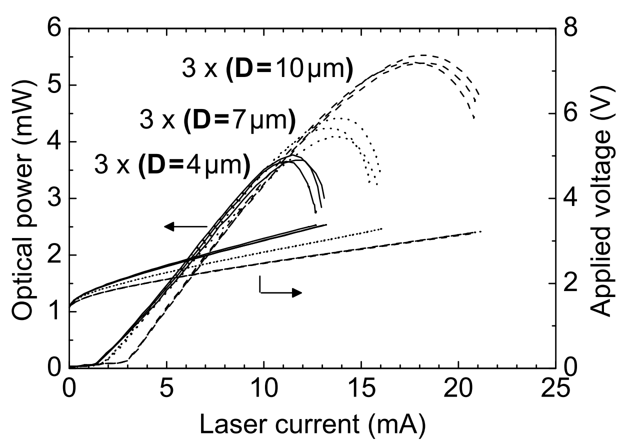

Fig. 3: LIV curves of the three VCSEL triples indicated in Fig. 2 within the direct-mesa flip-bonded 2-D array.

Figure 2 shows one of the bottom-emitting 850 nm VCSEL arrays after flip-bonding to a silicon carrier and removal of the opaque GaAs substrate leaving an epitaxially defined outcoupling facet. The carrier is a demonstration platform with coplanar lines for individual high-frequency electrical input to each of the 48 VCSELs in 16 channels on a 250 µm channel pitch. Only 10 µm high indium solder bumps permit direct-mesa bonding without shortening adjacent devices. Figure 3 gives the light–current–voltage (LIV) curves of the three VCSEL triples indicated in Fig. 2.

Outer mesa diameters and mesa gaps for the 10, 7, and 4 µm active diameter VCSELs are 17 and 3.5 µm, 14 and 2.5 µm, and 12 and 1.5 µm, respectively. The differential quantum efficiencies are between 29 and 31 %. Depending on the VCSEL size, the differential resistances are 77, 95, and 126 Ω with lasing thresholds of 3, 1.8, and 1.3 mA.

3. Data Transmission Experiments

Since within a channel three equivalent VCSELs are coupled into the same 50MMF, there is an inevitable radial VCSEL-to-fiber offset affecting the coupling efficiency. In Fig. 4, measured coupling efficiencies at different radial launch offsets normalized to the maximum coupling achieved for perfect alignment are shown. The built-in radial offsets in the $(4 \times 4) \times 3$ arrays presented are between 12.5 and 7.8 µm leading to acceptable offset coupling penalties below 0.8 dB.

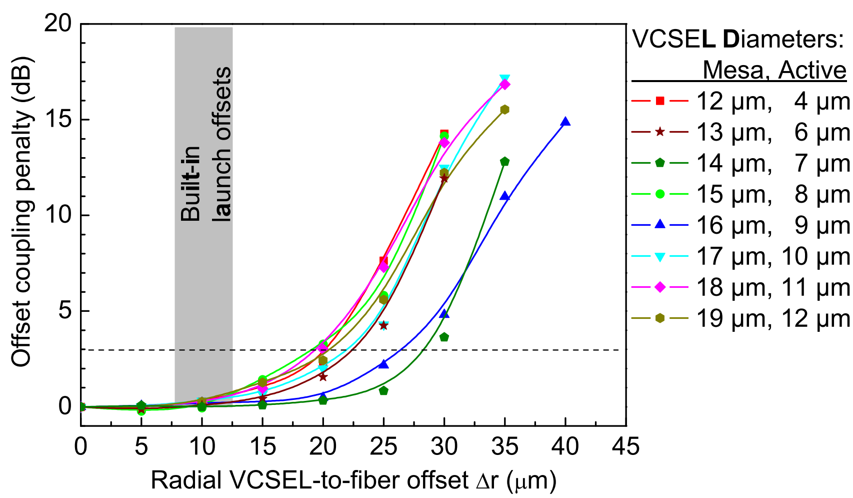

Fig. 4: Coupling efficiency at different radial VCSEL-to-fiber offsets normalized to center launch conditions.

For digital data transmission, the electrical input signals are fed from the perimeter of the silicon carrier via several millimeter-long coplanar lines to individual devices within the flip-bonded VCSEL arrays (see configuration on the left of Fig. 5). Despite the parasitics of those highly dense lines, wide open and symmetric eye patterns as in Fig. 5 were obtained for transmission of $2^{31} - 1$ word-length pseudo-random bit sequence (PRBS) signals at 10 Gbit/s over 500 m of butt-coupled 50MMF. This is well beyond the 300 m specification of the IEEE 10-Gigabit-Ethernet standard [3].

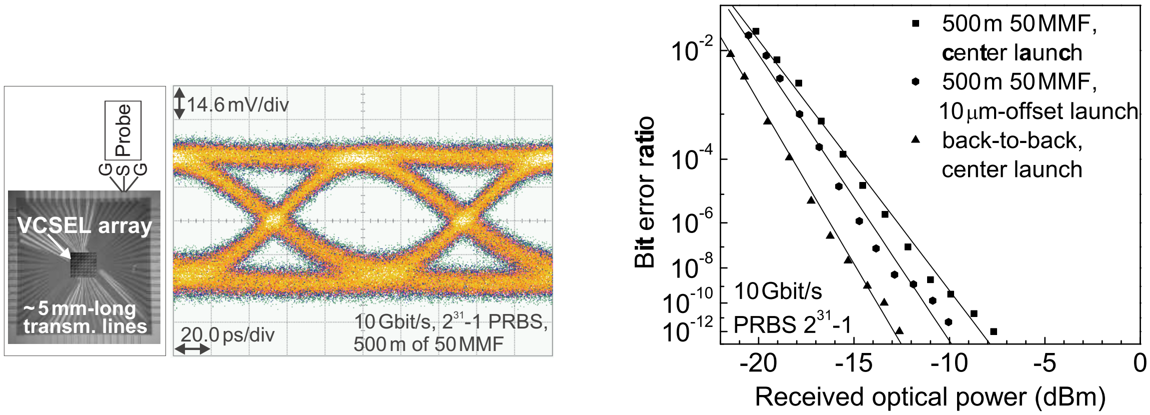

Fig. 5: 10 Gbit/s eye diagram after transmission over 500 m of 50MMF (*left*). The VCSELs are addressed via coplanar lines on the carrier as indicated on the far left. 10 Gbit/s BERs vs. mean received optical power back-to-back and for transmission over 500 m of 50MMF under offset launch and center launch conditions (*right*).

The bit error ratio (BER) curves in Fig. 5 indicate that quasi error-free (10^{-12} BER) data transmission was achieved over 500 m of 50MMF. There is a power penalty of up to 4 dB for transmission over the 50MMF. The 10 μm launch offset even leads to a slight improvement of the BERs as compared to center launch conditions. Such behavior is obtained with fibers of somewhat inferior differential mode delay (DMD) characteristics in the near-axial region.

4. Conclusion

Record-high integration densities of flip-chip bonded oxide-confined VCSELs in 2-D arrays enabled a 3-per-50MMF VCSEL redundancy for potential lifetime improvements of parallel-optic transmitters. Compactness and low module costs are preserved by still permitting butt-coupling to 50MMFs. The concept was proven by successfully transmitting 10 Gbit/s signals over 500 m of multimode fiber even under offset launch conditions as dictated by the redundant pixel designs.

References

[1] "Engineering Statistics: Internet Handbook", http://www.itl.nist.gov/div898/handbook/index.htm

[2] "VCSEL Chip Products Reliability Report", U-L-M photonics GmbH, Oct. 2005. http://www.ulm-photonics.com

[3] IEEE Standard 802.3ae$^{\mathrm{TM}}$, IEEE, Piscataway, NJ, USA, June 2002. http://grouper.ieee.org/groups/802/3/ae/

Fabrication and Characterization of 980 nm Bottom-Emitting VCSELs

Ihab Kardosh and Fernando Rinaldi

In this article we report on the fabrication of 980 nm bottom-emitting vertical-cavity surface-emitting lasers (VCSELs). Devices with different oxide apertures have been fabricated and characterized. After a fabrication overview, measurement results such as light–current–voltage (LIV) curves, spectra, and beam quality will be presented.

1. Introduction

Various applications like pumping of optical amplifiers, pumping of solid-state lasers and frequency doubling for visible laser light generation require high-power laser sources. VCSELs are an attractive light source for such applications, where in addition to high power a good beam quality or even single-mode operation is required. VECSELs [1] which are similar to VCSELs but use an extended cavity can achieve high power in a fundamental spatial mode. Fabrication of such devices requires first an investigation of bottom-emitting VCSELs. In the following we present the properties and characteristics of such devices emitting in the 980 nm spectral region.

2. Device Fabrication

Figure 1 shows a schematic drawing of a typical bottom-emitting VCSEL. The sample consists of InGaAs quantum wells separated by GaAs barrier layers, p- and n-type AlGaAs Bragg mirrors, and an AlAs layer for oxide confinement. After mesa etching, selective oxidation of the AlAs layer is performed to define the current aperture. Metallization layers are then evaporated to form a round p-type contact on top of the mesa. Normally the substrate is thinned to reduce absorption and to ease cleaving in case of device mounting on a heatsink. An anti-reflection (AR) coating layer is then deposited in the opening of the n-type contact on the substrate side.

3. Characterization

Bottom-emitting VCSELs with different oxide apertures have been characterized. The active diameters vary from 5 to 134 μm. On-wafer tested VCSELs with diameters of 5 μm have a maximum output power of about 8 mW and 1 . . . 2 mW in single-mode operation. In Fig. 2, LIV characteristics of a 8 μm device are plotted. The laser is measured on-wafer

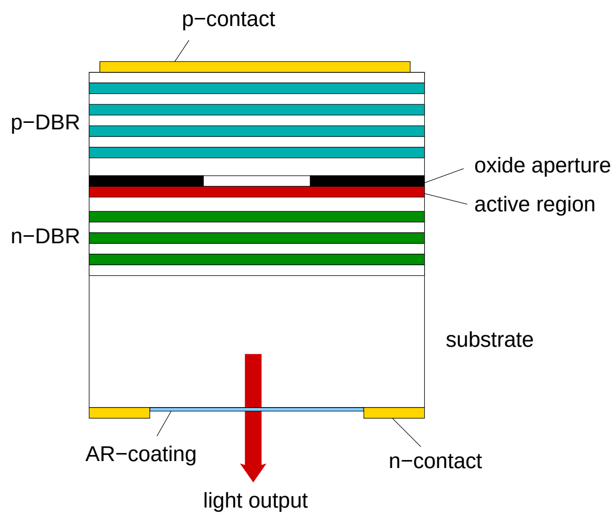

Fig. 1: Schematic cross-section of a bottom-emitting VCSEL.

at different temperatures from 0 to 50°C. The spectra are shown in Fig. 3 for different currents, measured at room temperature. When increasing the temperature, the maximum output power at thermal rollover decreases and shifts towards smaller currents. The ripples in the output power curve arise from the non-perfectly AR-coated substrate side. At room temperature the emission wavelength is about 980 nm, as can be seen in Fig. 3. The lowest threshold current of about 1 mA is measured at 50°C. At this temperature, the gain curve has shifted to longer wavelengths and matches the resonator design wavelength of 980 nm. Figure 4 shows the wavelength as a function of dissipated power. From the slope of the fit line and the known thermal wavelength shift (~ 0.07 nm/K), a thermal resistance of 910 K/W is calculated. Devices with an active diameter of 28 µm have also been characterized (Fig. 5). The maximum output power is 32 mW and the threshold current is about 4 mA. The device has a quantum efficiency of 43 %. The room temperature emission wavelength is about 963 nm. In general with the given quantum well material, at this wavelength we obtain the highest efficiency and the lowest threshold current.

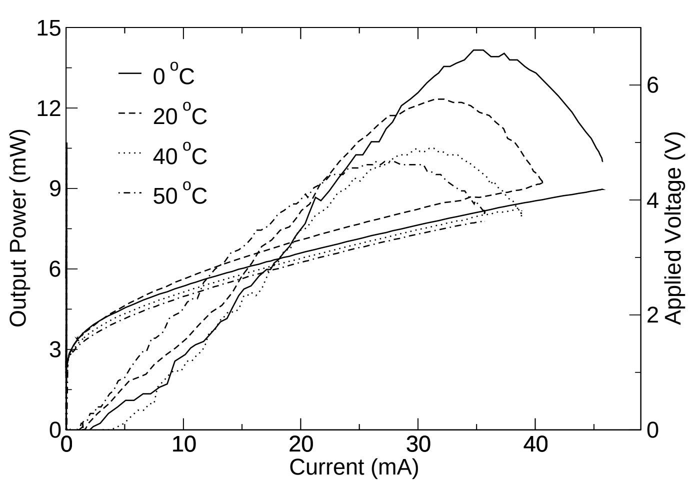

Fig. 2: LIV characteristics of a VCSEL with 8 µm active diameter, measured at different temperatures.

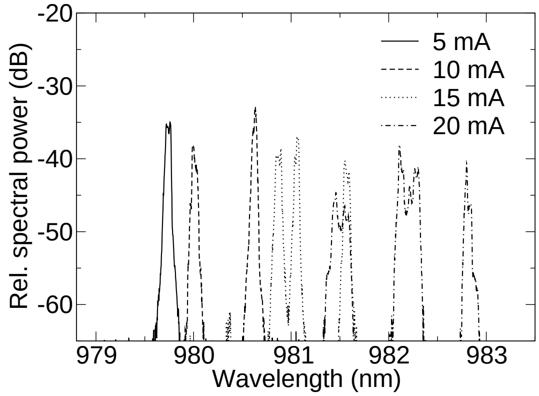

Fig. 3: Spectra at different currents of the measured 8 µm device (20°C).

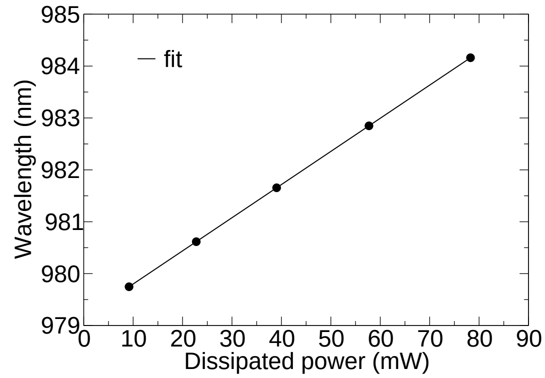

Fig. 4: Wavelength shift versus dissipated power, as determined from Fig. 3.

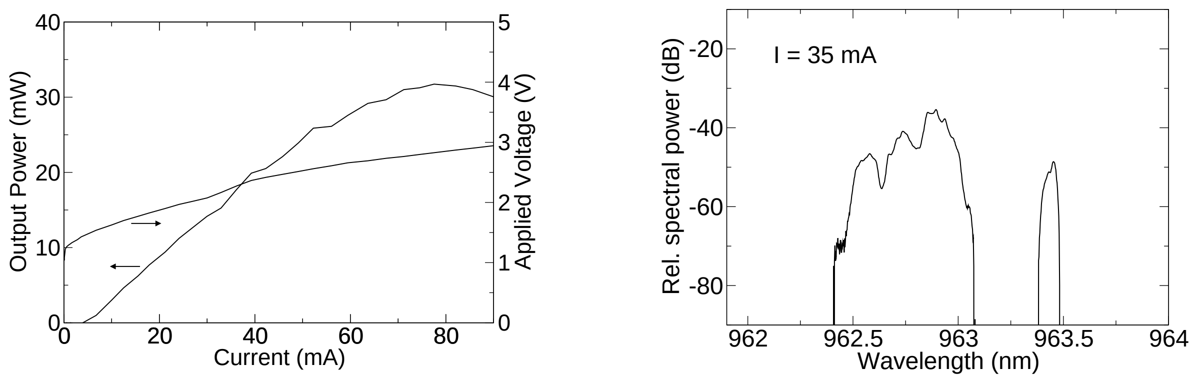

Fig. 5: LIV characteristics (left) and spectra (right) of bottom-emitting VCSELs with 28 µm active diameter.

3.1 High-power VCSELs

To get higher output power, VCSELs with an active diameter of 134 µm have been fabricated. The high-power devices are cleaved and soldered p-side down onto a diamond heatspreader, which is attached to a copper heatsink. On-wafer testing is not possible due to insufficient heat removal. Figure 6 shows the LIV characteristics and the emission spectra of such a laser. The threshold current is 74 mA and the maximum output power at thermal rollover is 275 mW. The emission wavelength is about 963 nm and the differential quantum efficiency is about 40 %. Mounted devices with large active diameters have lower thermal resistances than smaller devices. For the measured high-power laser we obtain about 40 K/W. For beam quality investigations a setup as described in [2] is used. Calculated beam diameters are plotted versus the propagation distance and fitted to obtain the beam parameters, namely the beam quality factor, the far-field angle, and the beam waist (Fig. 7). The VCSEL is driven at 400 mA and a beam waist of 168 µm is calculated. The far-field angle is 24.5°. Due to the large active diameter, multimode emission occurs, which affects the beam quality. For this device a beam quality factor of $M^2 = 57.8$ is determined.

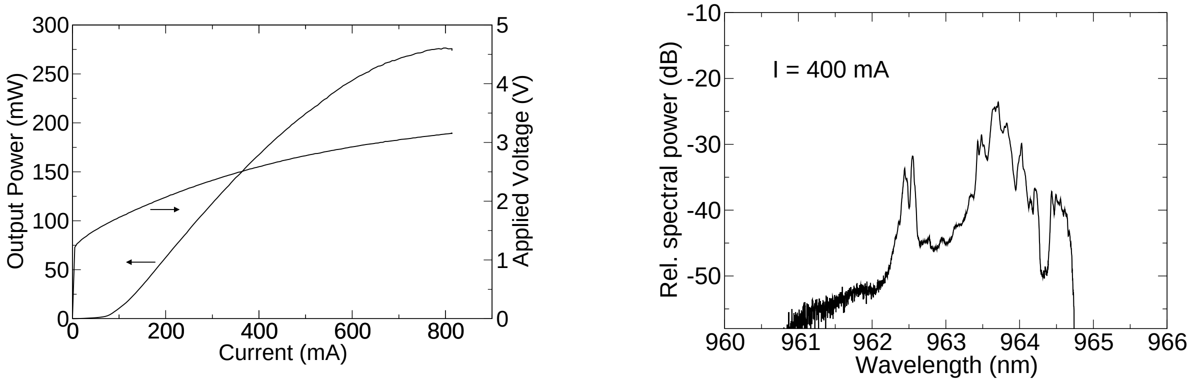

Fig. 6: LIV characteristics (left) and spectra (right) of a VCSEL with 134 µm active diameter.

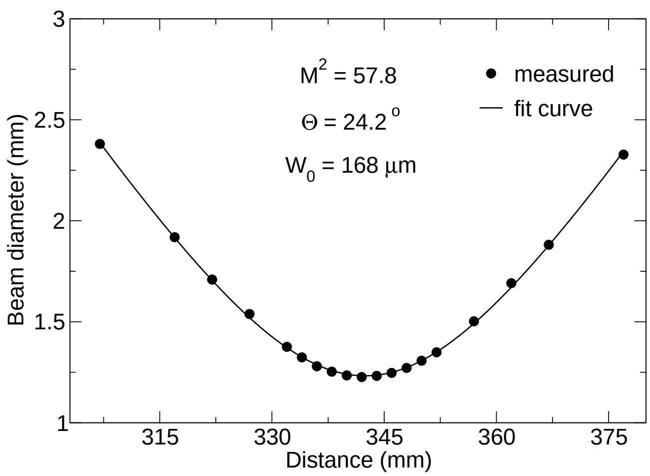

Fig. 7: M^2 plot of the high-power VCSEL from Fig. 6.

4. Conclusion

We have successfully fabricated and characterized 980 nm bottom-emitting VCSELs. Devices with active diameters of a few micrometers have a small threshold current of about 1 mA and can reach a maximum output power of more than 12 mW. Output power of about 32 mW and a threshold current of 4 mA from 28 µm devices have been measured. High-power VCSELs with 134 µm active diameter have an output power of 275 mW and a threshold current of 74 mA. In addition to the LIV characteristics and spectra, thermal properties and beam quality have been analyzed. The high-power device has a thermal resistance of 40 K/W. The M^2 factor increases for VCSELs with larger active diameter and can even exceed 50. The sample shows best efficiency close to 963 nm wavelength.

References

[1] A. Mooradian et al., "High power extended vertical cavity surface emitting diode lasers and arrays and their applications", in Proc. *11th Microoptics Conf., MOC '05*. Tokyo, Japan, Nov. 2005.

[2] I. Kardosh and F. Rinaldi, "Beam properties and M^2 measurements of high-power VCSELs". Annual Report 2004, Ulm University, Optoelectronics Department.

Surface Grating VCSELs With Dynamically Stable Light Output Polarization

Johannes Michael Ostermann and Pierluigi Debernardi†

It has been shown recently that the polarization of single- and multi-mode VCSELs can be defined and stabilized very effectively with a monolithically integrated surface grating. Orthogonal polarization suppression ratios of 20 dB or more have been achieved even for transverse multi-mode devices. On the other hand it has not been investigated in detail yet whether these lasers are also polarization-stable under high-frequency modulation. In this paper we show that surface grating VCSELs remain polarization-stable for digital high-frequency modulation up to 10 Gbit/s, modulation amplitudes of up to 1.5 V_{pp} and different modulation patterns. Under modulation, neither polarization-resolved time traces nor polarization-resolved spectra nor the power ratio of the two polarizations indicate a deterioration of the polarization properties compared to the static case.

1. Introduction

The design and fabrication of vertical-cavity surface-emitting lasers (VCSELs) with a dynamically stable polarization has been a research topic since it has been discovered fourteen years ago that VCSELs do not exhibit a well defined light output polarization [1]. This is due to the isotropic gain, the cylindrical resonator and the polarization-independent reflectivity of the Bragg mirrors of standard VCSELs. In most cases, due to the electro-optic effect [2], the individual transverse modes of VCSELs grown on (100)-oriented GaAs substrates are polarized either along the [011] or the $[0\bar{1}1]$ crystal axis, but they can abruptly change their orientation, which is then called a polarization switch [3]. There have been successful attempts to stabilize the polarization of VCSELs with non-cylindrical resonators, optical feedback, non-isotropic gain and mirrors with a polarization-dependent reflectivity (see [4] and the references therein). But up to now, only VCSELs grown on GaAs (311) B substrates could show a stable polarization under high-speed modulation due to non-isotropic gain. In [5] the orthogonal polarization suppression ratio (OPSR) of such VCSELs remained constant up to 10 Gbit/s modulation in case of multi-mode VCSELs. For single-mode VCSELs on the other hand, the OPSR decreased from 30 dB at static operation to 11 dB for a modulation frequency of 5 GHz.

Because most industrially fabricated VCSELs are realized on (100) substrates, we have been looking for a way to stabilize the polarization of VCSELs grown on these standard substrates. We have first theoretically [6] and then experimentally shown [7] that the

†Pierluigi Debernardi is with the IEIIT-CNR c/o Politecnico di Torino, Torino, Italy

polarization of single- and multi-mode VCSELs grown on (100) substrates can be well controlled with a monolithically integrated surface grating.

In this contribution we investigate the polarization properties of surface grating VCSELs under high-frequency modulation. All VCSELs are fabricated on the same sample and are tested on-wafer for the best possible comparison. The lasers are designed for an emission wavelength of 850 nm. The layer structure consists of three GaAs quantum wells inside a λ-cavity and of 21 and 37 Bragg-pairs for the upper and lower mirror, respectively. For more details on the investigated lasers we would like to refer the reader to [4], where one can find details on the fabrication process and static properties. Since it is in general more difficult to stabilize the polarization of multi-mode VCSELs than that of single-mode devices, in this paper we will mainly concentrate on the former. The polarization control induced by a surface grating works as well for single-mode VCSELs, as will also be shown. A possible application for polarization-stable multi-mode VCSELs is free-space optics employing polarization multiplexing for increased data throughput at high output powers.

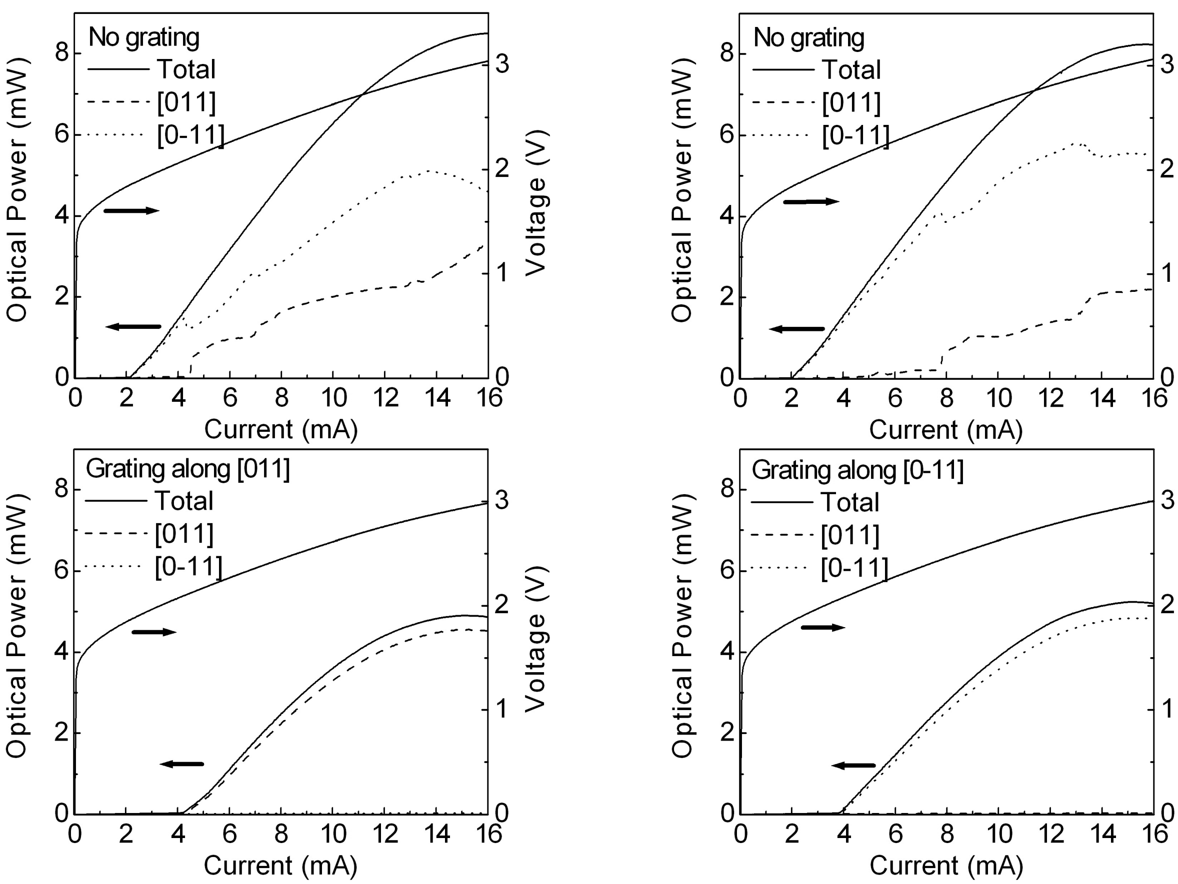

Fig. 1: IV and polarization-resolved LI characteristics of four adjacent lasers with an active diameter of 7 μm. The two VCSELs in the top row are standard lasers without a surface grating, while the two VCSELs in the bottom row have surface gratings with a grating period of 0.7 μm and a grating depth of 36 nm. The grating grooves are oriented along the [011] (bottom left) and [0$\bar{1}$1] (bottom right) crystal axis.

2. Polarization Behavior Under Modulation

Figure 1 shows the light–current–voltage (LIV) characteristics of four adjacent lasers with an active diameter of 7 μm. The lasers are nominally identical except that the two lasers in the upper row are standard VCSELs without a surface grating, while the lasers in the lower row have a monolithically integrated surface grating with a grating period of 0.7 μm and a grating depth of 36 nm. As is the case for the majority of standard multi-mode VCSELs, the output power of the devices is distributed more or less equally between both polarizations, in the present case with a slight preference of the $[0\bar{1}1]$ direction. In contrast to that, the VCSELs with a monolithically integrated surface grating have one dominant polarization for all modes. The orientation of this dominant polarization is parallel to the grating grooves independent of their orientation along the [011] or $[0\bar{1}1]$ crystal axis.

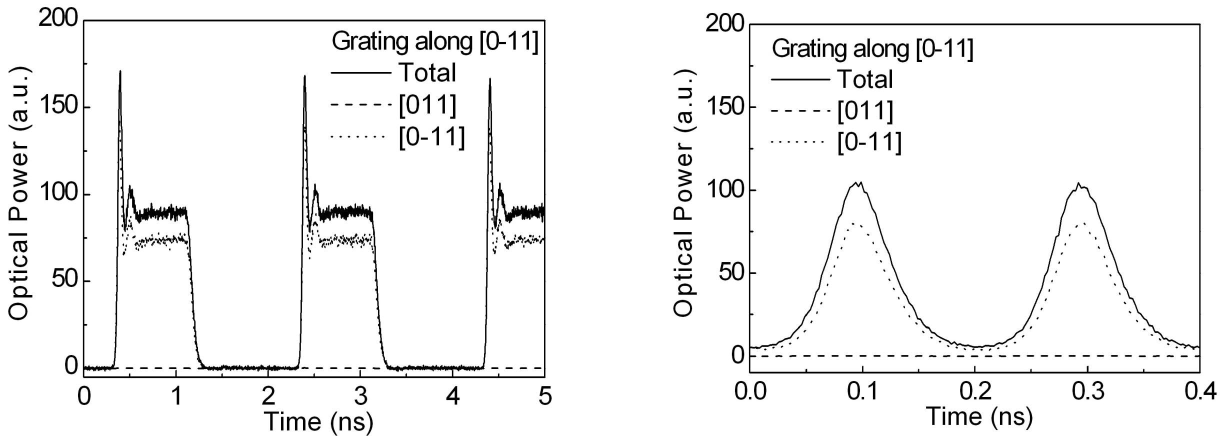

Fig. 2: Polarization-resolved time traces of the bottom-right surface grating VCSEL from Fig. 1. The bias current is 8 mA, the modulation amplitude 1.5 V_{pp}, and the repetition rates of the alternating 1-0 patterns are 500 MHz (left) and 5 GHz (right).

Using an optical sampling oscilloscope we have measured polarization-resolved time traces of the laser from Fig.1 with the surface grating oriented along the $[0\bar{1}1]$ crystal axis for a bias current of 8 mA, an alternating 1-0 pattern and a modulation amplitude of 1.5 V_{pp}. The difference between the total optical power and the power in the polarization along the $[0\bar{1}1]$ crystal axis is due to the insertion loss of the polarization-dependent isolator used as polarizer for these measurements. Applying this large modulation amplitude, the laser is turned completely off and on again for a data rate of 1 Gbit/s (Fig. 2 left). But nevertheless, only the polarization parallel to the surface grating is modulated, while the orthogonal polarization remains clearly suppressed by 25 dB during the on-state. While at a modulation with 10 Gbit/s, due to the limited modulation bandwidth, the laser is no longer switched completely off and on (right side of Fig. 2), the on-off ratio of the modulation nevertheless exceeds 12 dB and the orthogonal polarization is still suppressed by 25 dB.

Under the same modulation conditions as for Fig. 2, we have measured the time-averaged output power in the two orthogonal polarizations with a photodiode under different modulation data rates and modulation patterns for all lasers from Fig. 1. From the data we have calculated the OPSRs which are shown in Fig. 3. The data rate was varied between

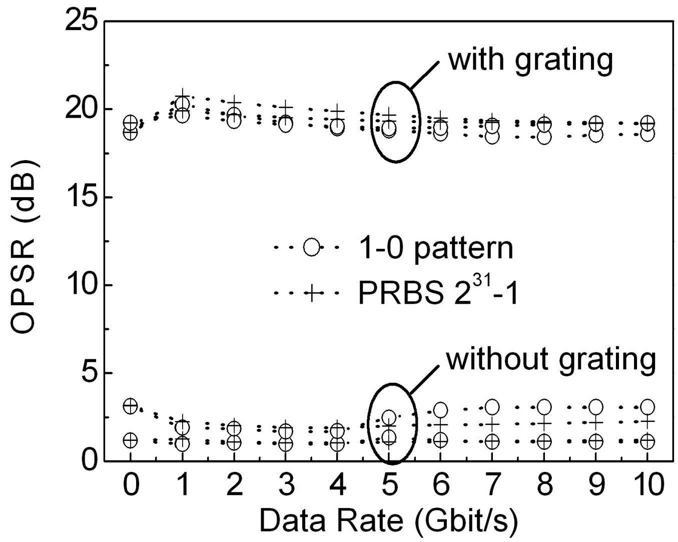

Fig. 3: OPSRs of all lasers from Fig. 1 for different data rates measured at a bias current of 8 mA and with a modulation amplitude of 1.5 V_{pp}.

0 and 10 Gbit/s and we have used a 1-0 pattern as well as a pseudorandom bit sequence (PRBS) with a word length of $2^{31} - 1$. As a result, the OPSRs of the surface grating VCSELs are not decreasing by more than 0.3 dB below their static values for any modulation parameter. Likewise, the OPSRs of the standard VCSELs remain very small, independent of the modulation speed.

As an example, the spectra of a standard VCSEL and a VCSEL with a surface grating from Fig. 1, modulated with a data rate of 3 Gbit/s around a bias current of 8 mA, are shown in Fig. 4. The modulation amplitude is 1.5 V_{pp} and we used a 1-0 pattern. The standard laser (left) has contributions from both polarizations in every individual mode, while in the spectra of the surface grating VCSEL (right) the orthogonal polarization is clearly suppressed for all modes.

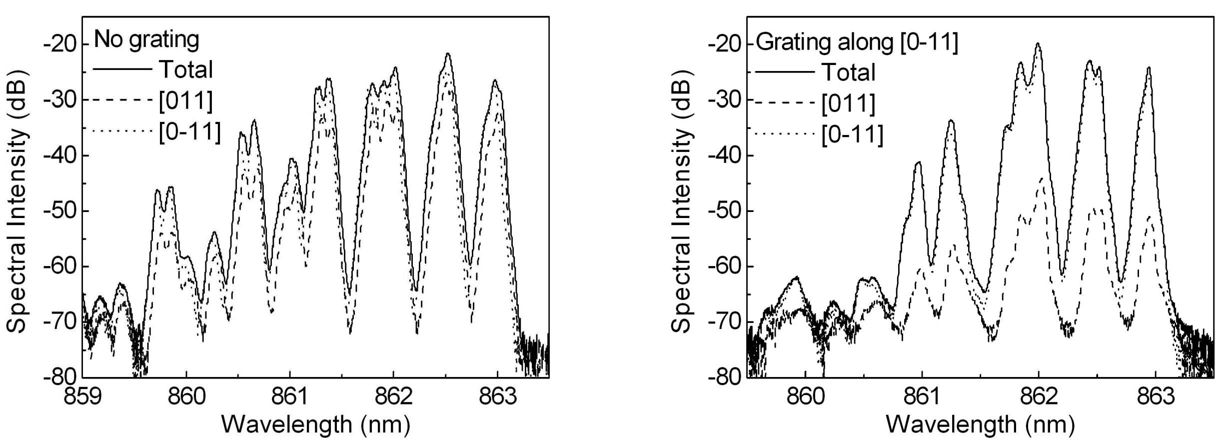

Fig. 4: Polarization-resolved spectra of a standard VCSEL (left) and a VCSEL with a surface grating (right) from Fig. 1 under high-frequency modulation.

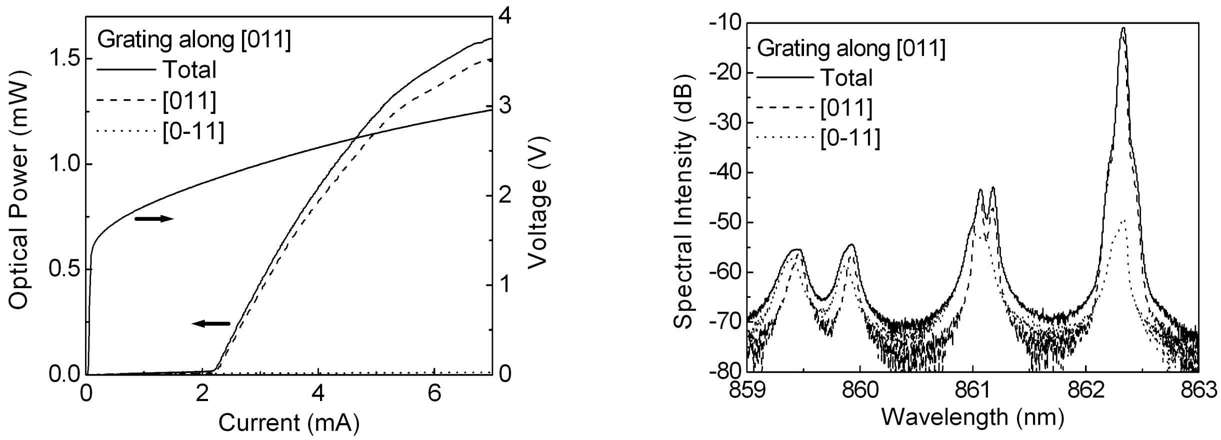

Fig. 5: IV and polarization-resolved LI characteristics of a grating VCSEL with an active diameter of 4 µm (left) as well as its spectra at a bias current of 5 mA under modulation with a 1-0 pattern, 10 Gbit/s data rate and a modulation amplitude of 1.0 V_{pp} (right).

The left side of Fig. 5 displays the LIV characteristics of a surface grating VCSEL having the same grating parameters as the lasers in Fig. 1 but a smaller oxide diameter of 4 µm. The polarization-resolved spectra on the right side of Fig. 5 are taken at a bias current of 5 mA under a modulation with a 1-0 pattern, 10 Gbit/s data rate and a modulation amplitude of 1.0 V_{pp}. While the peak-to-peak difference between the two polarizations is 37 dB in the case of static operation, it does not decrease below 36 dB when the modulation is applied. Therefore also in the case of single-mode emission no significant decrease of the OPSR could be found.

3. Small-Signal Analysis and Eye Diagrams

The polarization-resolved small-signal analysis of a standard VCSEL in Fig. 6 (top left) reveals that both polarizations are modulated. The curves have been smoothened for better clarity. For the investigation of the small-signal frequency response as well as for displaying the eye diagrams we have used a detector with a 3-dB bandwidth of 10 GHz. For frequencies larger than 7 GHz the response in the $[0\bar{1}1]$ polarization seems to be higher than for the total power. But this is just due to a strongly increased noise level, which can be seen from the response in the $[0\bar{1}1]$ polarization at a bias current of 6 mA with the RF signal turned off, which is also included in the graph. If the OPSR of a VCSEL is small for a bias well above threshold, its two polarizations have a strong anticorrelation [8]. Therefore, if only one polarization is selected, the measured noise strongly increases, but the amount of increase depends on which polarization is selected. As a consequence of this anticorrelation between the two polarizations, the optical eye diagrams of both polarizations for 10 Gbit/s, PRBS $2^{31}-1$ modulation with 10 mA bias current and applied 1 V_{pp} modulation amplitude close when a polarizer is inserted in the optical path (Fig. 6, bottom row), while in contrast the eye is clearly open without a polarizer (top right) for the same total received power.

Quite in contrast, a VCSEL with a surface grating shows a response to the small-signal

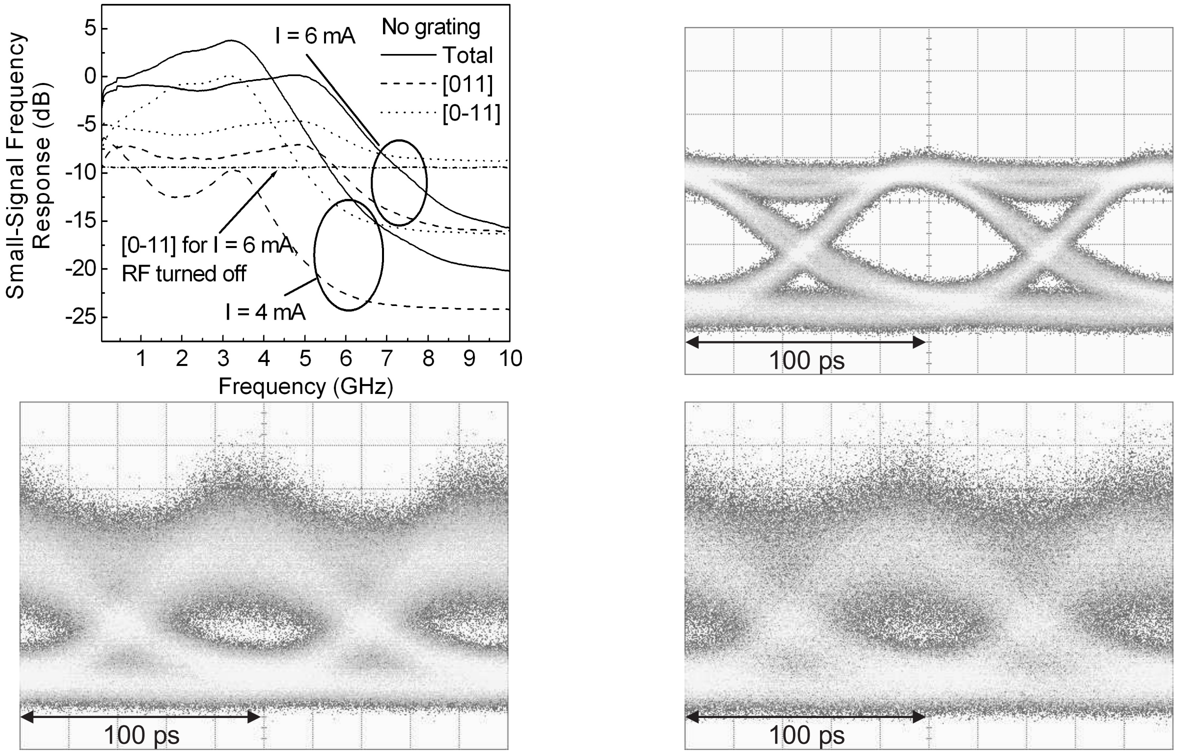

Fig. 6: Small-signal frequency responses (top left) of a standard VCSEL (the top left one in Fig. 1) for bias currents of 4 and 6 mA as well as eye diagrams for 10 Gbit/s, PRBS $2^{31}-1$ modulation without a polarizer in the optical link (top right) and with a polarizer (bottom; left: [011] polarization, right: [0$\bar{1}$1] polarization).

modulation only in one polarization (Fig. 7, top left). When inserting a polarizer in the optical path, which is oriented to transmit the dominant [0$\bar{1}$1] polarization, the quality of the 10 Gbit/s optical eye diagram remains basically unchanged (bottom right) compared to the case without a polarizer (top right), while there is no signal in the orthogonal polarization (bottom left) for 11 mA bias current and applied 1 V_{pp} modulation amplitude.

4. Conclusion

VCSELs with monolithically integrated surface gratings have shown one dynamically stable polarization for all modes and all tested modulation parameters, namely digital modulation speeds up to 10 Gbit/s, modulation amplitudes up to 1.5 V_{pp}, and two different bit patterns (1-0 and PRBS $2^{31}-1$). No significant decrease of the OPSR could be found for any device. Also when switching the laser on and off, the orthogonal polarization remains clearly suppressed, as can be seen from polarization-resolved time traces. Therefore surface grating VCSELs are well suited for high-frequency applications requiring a stable light output polarization.

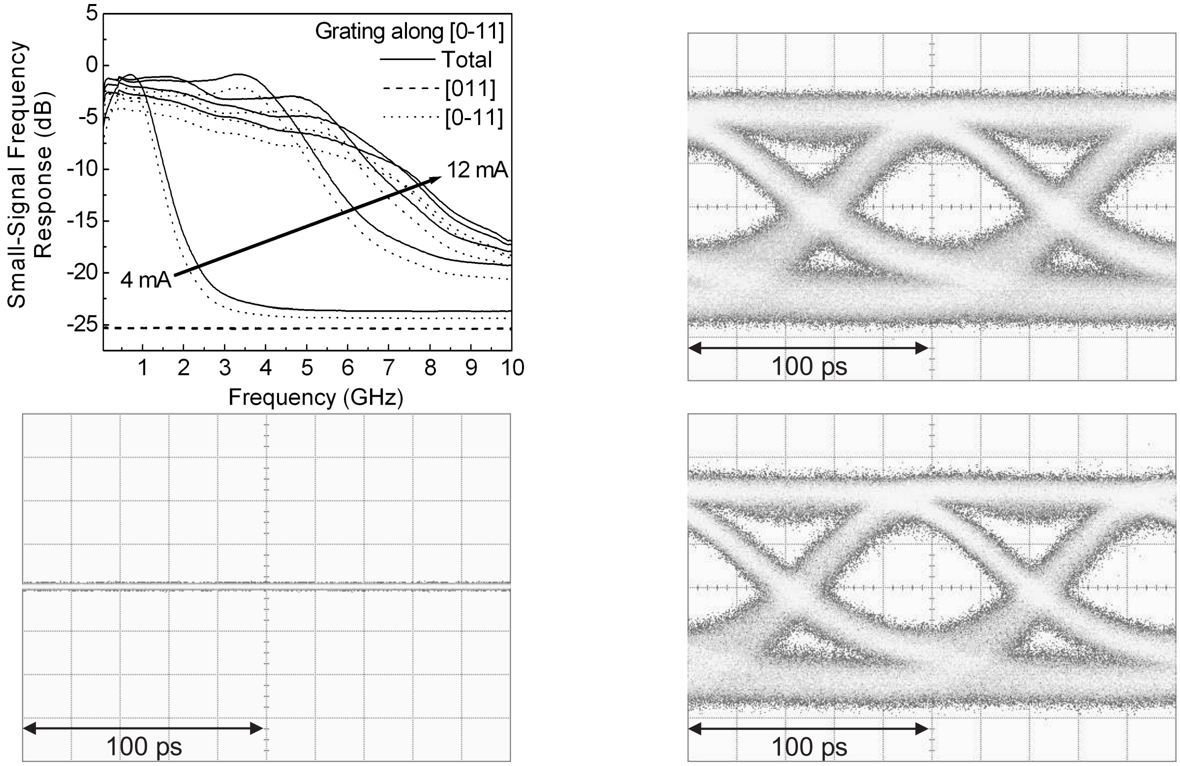

Fig. 7: Small-signal frequency responses (top left) of a grating VCSEL (bottom right in Fig. 1) for bias currents of 4 to 12 mA in steps of 2 mA and 10 Gbit/s eye diagrams as in Fig. 6 (top right: without polarizer, bottom left: polarizer in [011] direction, bottom right: [0$\bar{1}$1]).

Acknowledgment

The authors would like to thank Philipp Gerlach and the former VCSEL group member Felix Mederer for their help in performing and discussing the measurements and U-L-M photonics and Yakiv Men for their processing support. The University of Ulm gratefully acknowledges the partial funding of this work by the German Research Foundation (DFG).

References

[1] C. Chang-Hasnain, J. Harbison, L. Florez, and N. Stoffel, "Polarisation characteristics of quantum well vertical cavity surface emitting lasers," *Electron. Lett.*, vol. 27, no. 2, pp. 163–165, 1991.

[2] M.P. van Exter, A.K. Jansen van Doorn, and J.P. Woerdman, "Electro-optic effect and birefringence in semiconductor vertical-cavity lasers," *Phys. Rev. A*, vol. 56, no. 1, pp. 845–853, 1997.

[3] M. San Miguel, Q. Feng, and J.V. Moloney, "Light-polarization dynamics in surface-emitting semiconductor lasers," *Phys. Rev. A*, vol. 52, no. 2, pp. 1728–1739, 1995.

[4] P. Debernardi, J.M. Ostermann, M. Feneberg, C. Jalics, and R. Michalzik, "Reliable polarization control of VCSELs through a monolithically integrated surface grating: a comparative theoretical and experimental study," *IEEE J. Select. Topics Quantum Electron.*, vol. 11, no. 1, pp. 107–116, 2005.

[5] N. Nishiyama, A. Mizutani, N. Hatori, A. Mizutani, M. Arai, F. Koyama, and K. Iga, "Lasing characteristics of InGaAs-GaAs polarization controlled vertical-cavity surface-emitting laser grown on GaAs (311)A substrates," *IEEE J. Select. Topics Quantum Electron.*, vol. 5, no. 3, pp. 530–536, 1999.

[6] P. Debernardi and G.P. Bava, "Coupled mode theory: a powerful tool for analyzing complex VCSELs and designing advanced device features," *IEEE J. Select. Topics Quantum Electron.*, vol. 9, no. 3, pp. 905–917, 2003.

[7] J.M. Ostermann, P. Debernardi, C. Jalics, A. Kroner, M.C. Riedl, and R. Michalzik, "Surface gratings for polarization control of single- and multi-mode oxide-confined vertical-cavity surface-emitting lasers," *Optics Communications*, vol. 246, no. 4–6, pp. 511–519, 2005.

[8] J.-L. Vey, C. Degen, K. Auen, and W. Elsäßer, "Quantum noise and polarization properties of vertical-cavity surface-emitting lasers," *Phys. Rev. A*, vol. 60, no. 4, pp. 3284–3295, 1999.

VCSELs With Enhanced Single-Mode Power and Stabilized Polarization for Oxygen Sensing

Fernando Rinaldi and Johannes Michael Ostermann

Vertical-cavity surface-emitting lasers (VCSELs) with single-mode, single-polarization emission at a wavelength of approximately 763 nm have become attractive for oxygen sensing. Up to now, VCSELs used for this application are single-mode because of a small active diameter which correspondingly leads to small optical output power. Employing the surface relief technique and in particular the surface grating relief technique, we have increased the single-mode output to more than 2.5 mW averaged over a large device quantity. To the best of our knowledge, this is the highest single-mode power ever reported for VCSELs in this wavelength range. Through the grating relief simultaneously we were able to stabilize the light polarization.

1. Introduction

Over the last years spectroscopy has emerged as a new application area for VCSELs. Especially oxygen sensing with VCSELs is well studied [1], [2]. The emission wavelength of the laser is first fine-tuned to the absorption line of interest by varying the substrate temperature. Then this absorption line is scanned by modulating the laser current. Fitting the measured line shape, the oxygen concentration in the examined gas can be determined. This method allows an in-situ and online monitoring of the oxygen concentration. The advantages of using VCSELs in these systems are their circular output beam with the associated ease of building an optical system, low operating currents, efficient tunability and the potential for low cost. While VCSELs are inherently longitudinal single-mode, they can emit in multiple transverse modes if the active diameter is not small enough. But a small active diameter has the drawback of the single-mode power of such devices to be also rather limited. In the past, a surface relief has been used to achieve a significant increase of the single-mode output power as well as of the active diameter of oxide-confined VCSELs [3], [4].

However, besides single-mode operation with a large side-mode suppression ratio also a stable polarization is required. Due to their isotropic gain, their cylindrical resonator and their mirrors with a polarization-independent reflectivity, VCSELs have a priori no preferred direction of polarization. Due to the electro-optic effect, VCSELs grown on (100)-oriented GaAs substrates are mainly polarized along the [011] and the $[0\bar{1}1]$ crystal axes. But if the current or the temperature is changed, the polarization can abruptly change its orientation from one of these crystal axes to the other. Such a polarization switch is accompanied by a change of the emission wavelength of up to 40 GHz (see [5] and the references therein). Therefore in particular VCSELs used for oxygen sensing need a controlled polarization. In [6] a surface grating monolithically integrated in the top Bragg mirror of a VCSEL was proposed as a method for polarization control. This technique has been successfully demonstrated in [5], [7]. Also in [6] it was shown theoretically that a surface grating combined with a surface relief can simultaneously lead to a stable polarization and to an increased single-mode output power. In this contribution we report on the grating relief technique applied to 760 nm range VCSELs. The fabricated devices show record-high output power and stable polarization.

2. Fabrication

The wafer was grown by solid source molecular beam epitaxy on a n-doped GaAs (100)-substrate. The lower Bragg mirror is composed of 32 AlAs/AlGaAs and 8 AlGaAs/AlGaAs layer pairs. The active layer consists of three AlGaAs quantum wells with 14 % aluminum content. Above the active region there is an AlAs layer for wet chemical oxidation and 26 AlGaAs/AlGaAs layer pairs forming the upper mirror.

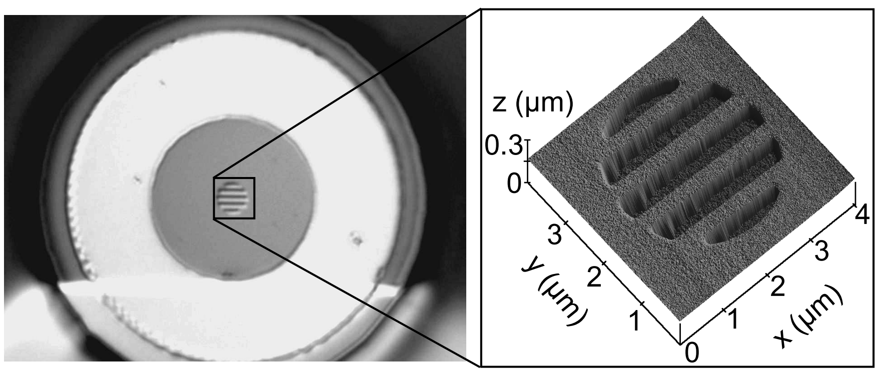

Fig. 1: Photograph of a VCSEL with an integrated surface grating relief (left) and an atomic force microscope (AFM) measurement showing the grating relief in more detail (right).

The structure has an extra topmost $\lambda/(4 \cdot n)$-thick GaAs layer (with n as the refractive index of GaAs) to achieve an anti-phase reflection for all modes. By etching a circular area of 3 µm diameter in the center of this cap-layer, the reflectivity is again increased for the fundamental mode. If instead a grating with the same extension is etched into the cap-layer (see Fig. 1), this leads in addition to different reflectivities for the two polarizations of the fundamental mode.

3. Electro-Optical and Spectral Characteristics

The polarization-resolved light–current–voltage (LIV) characteristics of a typical device are shown in Fig. 2 for substrate temperatures between 10 and 60 °C. This device has an active diameter of approximately 4 µm, a grating relief with a diameter of 3 µm, a grating period of 0.8 µm and a grating depth of 44 nm. The VCSEL is single-mode up to 5 mA current with a side-mode suppression ratio (SMSR) of more than 30 dB. Depending on

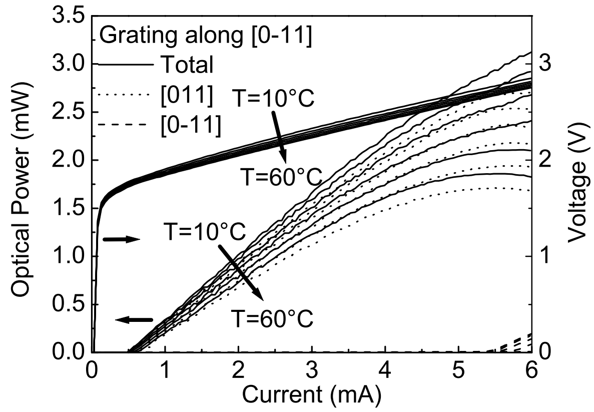

Fig. 2: Polarization-resolved LIV characteristics of a 4 µm VCSEL with a 3 µm diameter grating relief, a grating period of 0.8 µm and a grating depth of 44 nm for substrate temperatures varied between 10 and 60 °C in steps of 10 °C .

the substrate temperature it has a single-mode output power between 1.8 and 2.7 mW, which is to the best of our knowledge the highest single-mode output power ever reported for VCSELs in this wavelength range.

As can be seen in Fig. 2, for the complete current and temperature range the fundamental mode of the VCSEL is polarized strictly along the [011] crystal axis, which is orthogonal to the grating grooves. The power of the orthogonal polarization of the device shown in Fig. 2 stays below 6 µW up to a current of 5 mA, where the first higher order mode starts to lase. The orthogonal polarization suppression ratio (OPSR) is therefore above 26 dB between 2.5 and 5 mA (Fig. 3, left side). The peak-to-peak OPSR measured in the spectra in Fig. 3 (right side) is 33 dB, which corresponds to the limit of the employed polarizer. The OPSR taken from the spectra is larger than the value calculated from the LI characteristics since spontaneous emission is not considered in the peak-to-peak definition of the OPSR.

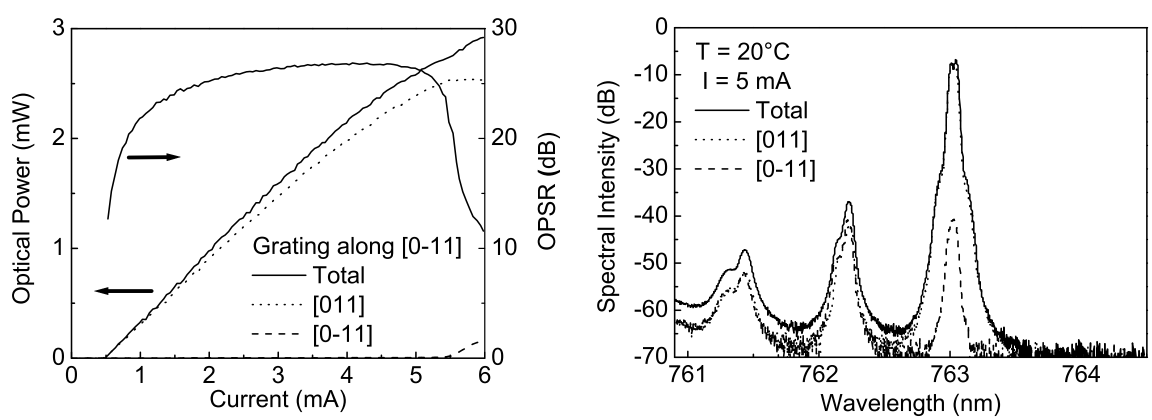

Fig. 3: Polarization-resolved LI characteristics and the orthogonal polarization suppression ratio (OPSR) of the VCSEL from Fig. 2 for a substrate temperature of $T = 20\,°\mathrm{C}$ (left) and a polarization-resolved spectrum of the same VCSEL at $T = 20\,°\mathrm{C}$ and $I = 5\,\mathrm{mA}$ (right).

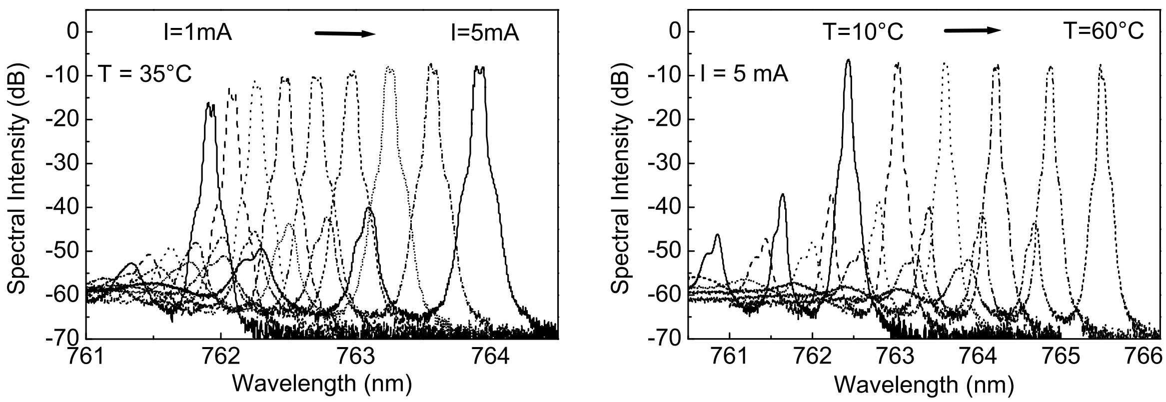

Fig. 4: Spectra of the laser from Fig. 2 at $T = 35\,°\mathrm{C}$ for currents varying from 1 to 5 mA in steps of 0.5 mA (left) and at a current of 5 mA for temperatures between 10 and 60 °C in steps of 10 °C (right).

The laser can be conveniently tuned over the wavelength range of interest by the current and the temperature, as illustrated in Fig. 4. Over the whole tuning range it stays single-mode with a SMSR of 30 dB. The current and temperature tuning coefficients are 0.6 nm/mA and 0.06 nm/K, respectively, which is comparable to the values measured in [2].

4. Emission Far-Field

Gratings can cause diffraction lobes in the far-field in the direction orthogonal to the grating grooves [7], but the present grating relief has almost no influence on the far-field. Hardly some small ripples can be seen in the far-field measured orthogonal to the grating, which is shown in Fig. 5 on the right side. The full width at half maximum far-field angle of 10.1° parallel and 9.4° orthogonal to the grating is comparable to 10.4° for a standard reference devices fabricated on the same sample.

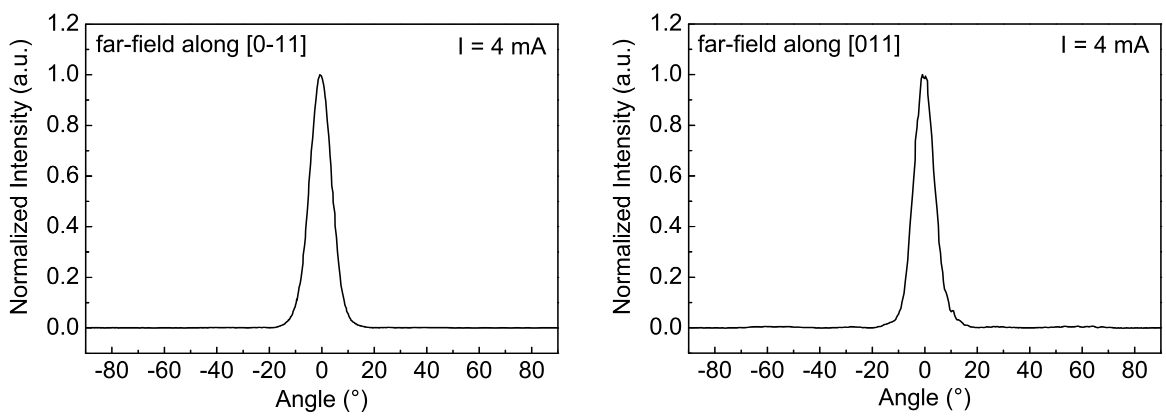

Fig. 5: Far-field of the laser from Fig. 2 measured parallel (left) and orthogonal (right) to the grating grooves.

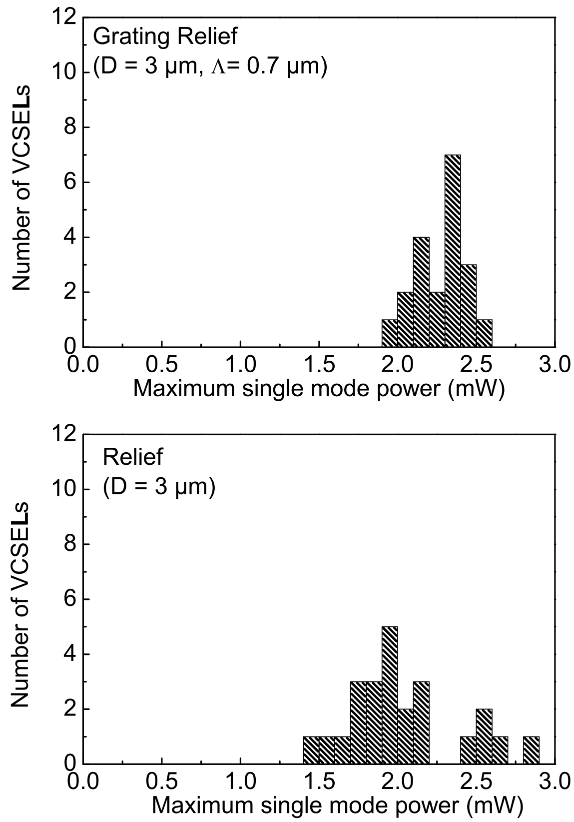

Fig. 6: Distribution of the maximum single-mode output power of 4 μm active diameter VCSELs with a grating relief with 3 μm diameter and a grating period of 0.7 μm (upper left graph), a grating period of 0.8 μm (upper right), a standard relief with 3 μm diameter (lower left) and standard devices as reference (lower right).

5. Increased Single-Mode Output Power

In Fig. 6 we compare four kinds of VCSELs, all on the same sample for best possible comparison, with an oxide diameter of 4 μm. These are 3 μm diameter grating relief devices (34 to 74 nm grating depth and both 0.7 μm and 0.8 μm grating period), 3 μm standard relief VCSELs and reference devices with the cap-layer etched over the whole aperture to the same depth as the grating. We have realized devices with etch depths of 34, 44, 54, 64 and 74 nm, which corresponds roughly to $\lambda/(4 \cdot n) \pm 20$ nm. Since we couldn't find a dependence of the device performance on the etch depth, in the following we will not distinguish between the different etch depths. Due to a layer thickness variation over the wafer, the investigated lasers have emission wavelengths between 750 to 790 nm. Some problems arose on that wafer due to some large defects with a diameter comparable to the mesa diameter of a VCSEL. These defects prevent some lasers from operating properly or even inhibit lasing. Thus we have not taken those lasers into account which have a distance from such a defect of less than 50 μm, i.e. which have a defect within twice the mesa diameter. According to this rule twelve lasers had to be excluded. The statistics shown in Fig. 6 still considers 87 lasers. While the reference devices have an average single-mode output power of 1.08 mW and are therefore comparable to previously published lasers at

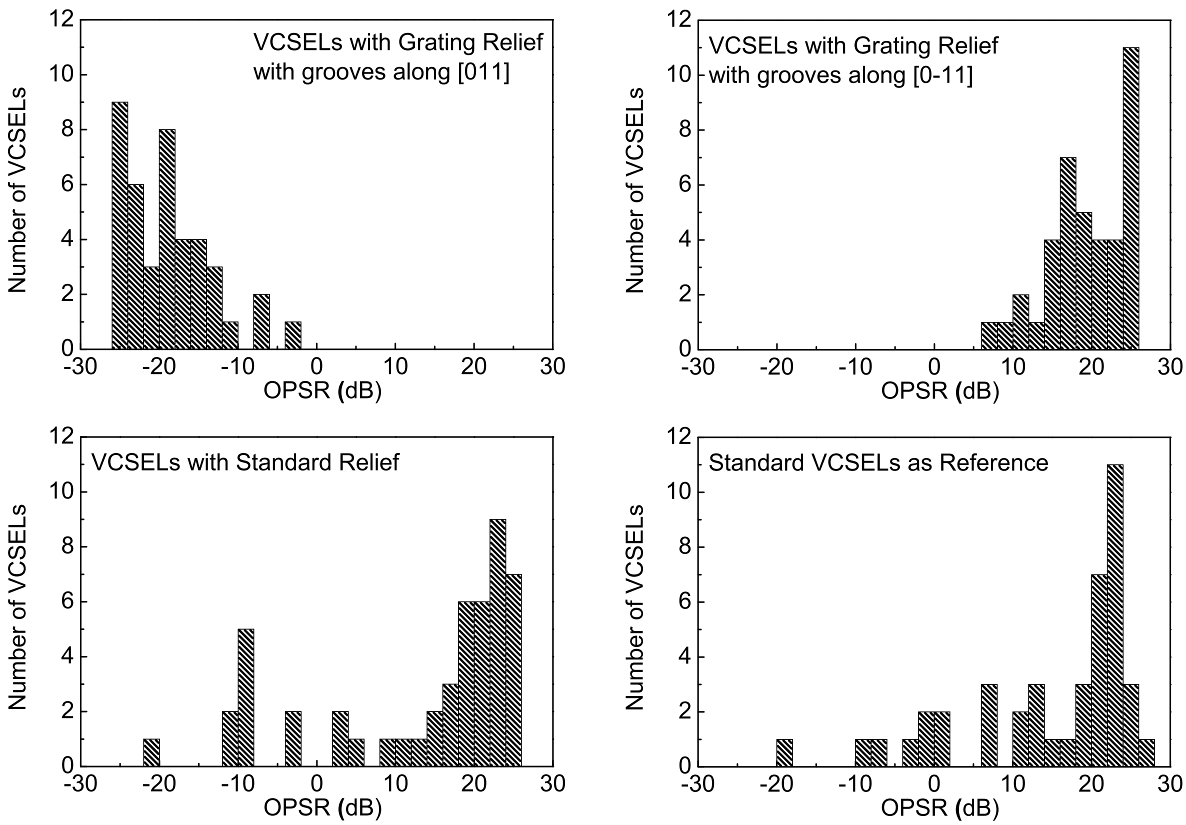

Fig. 7: Distribution of the averaged OPSR of VCSELs with the grating grooves along the [011] crystal axis (upper left graph), along the $[0\bar{1}1]$ crystal axis (upper right), of VCSELs with a standard surface relief (lower left) and of standard VCSELs as reference (lower right).

that wavelength [2], the VCSELs with a standard relief have a single-mode output power of 2.02 mW on average. In contrast, with a grating relief we could achieve an average single-mode output power of 2.29 mW for a grating period of 0.7 µm and even 2.65 mW for a grating period of 0.8 µm. This increase is due to higher outcoupling losses of the grating relief while the threshold current is almost unchanged.

6. Stabilized Polarization

To judge the influence of the grating on the polarization, we have measured the polarization-resolved LI characteristics of the devices shown in Fig. 6, but also of the same amount of devices with same parameters except for an active diameter of 3 µm. In these measurements the polarizer was strictly oriented along the [011] or $[0\bar{1}1]$ crystal axis. The OPSR shown in Fig. 7 is defined as the ratio $P_{[011]}/P_{[0\bar{1}1]}$ between optical powers in the respective crystal directions. The OPSR was calculated for data points in steps of 0.1 mA and then averaged over the current range yielding 10 to 100 % of the maximum single-mode output power. While the lasers without a grating in Fig. 7 show an orientation of the polarization along both crystal axes, the polarization of the devices with a grating relief is defined by the orientation of the grating grooves. If they are oriented along the [011] crystal axis, the lasers are polarized along the $[0\bar{1}1]$ crystal axis. If the grating grooves are turned by 90°, also the polarization of the lasers is turned by 90°. Devices which have a polarization not exactly oriented along one of the crystal axes have a reduced OPSR magnitude. Also strain caused by the defects as well as polarization switches can explain lower OPSRs. The latter have been observed for 15 out of 92 devices without a surface grating, but only for one out of 80 devices with a grating. By eliminating the defects, one should be able to achieve OPSR magnitudes of above 20 dB for all devices with a grating relief.

7. Conclusion

A monolithically integrated grating relief has shown to increase the maximum single-mode output power of VCSELs from 1.08 mW to 2.65 mW on average in the emission wavelength range from 750 to 790 nm. At the same time the orientation of the polarization was defined by the orientation of the grating grooves and polarization switches could be avoided with a yield of 98.75%, which is expected to be increased for a wafer with a lower defect density. The grating relief has shown no negative influence on the overall laser performance. Therefore an integrated grating relief is a very attractive approach for increasing the single-mode output power and stabilizing the polarization at the same time.

Acknowledgment

The authors would like to thank the Ministry of Economics of the State of Baden-Württemberg as well as the German Research Foundation (DFG) for funding this work and Mr. Yakiv Men for performing the electron beam lithography.

References

[1] P. Vogel and V. Ebert, “Near shot noise detection of oxygen in the A-band with vertical-cavity surface-emitting lasers,” *Appl. Phys. B*, vol. 72, no. 1, pp. 127–135, 2001.

[2] H.P. Zappe, M. Hesse, M. Moser, R. Hövel, K. Gulden, H.-P. Gauggel, and F. Monti di Sopra, “Narrow-linewidth vertical-cavity surface-emitting lasers for oxygen detection,” *Appl. Optics*, vol. 39, no. 15, pp. 2475–2479, 2000.

[3] H.J. Unold, S.W.Z. Mahmoud, R. Jäger, M. Grabherr, R. Michalzik, and K.J. Ebeling, “Large-area single-mode VCSELs and the self-aligned surface relief,” *IEEE J. Select. Topics Quantum Electron.*, vol. 7, no. 2, pp. 386–392, 2001.

[4] Å. Haglund, J.S. Gustavsson, J. Vukušić, P. Modh, and A. Larsson, “Single fundamental mode output power exceeding 6 mW from VCSEls with a shallow surface relief,” *IEEE Photon. Technol. Lett.*, vol. 16, no. 2, pp. 386–392, 2004.

[5] J.M. Ostermann, P. Debernardi, C. Jalics, A. Kroner, M.C. Riedl, and R. Michalzik, “Surface gratings for polarization control of single- and multi-mode oxide-confined vertical-cavity surface-emitting lasers,” *Optics Communications*, vol. 246, no. 4–6, pp. 511–519, 2005.

[6] P. Debernardi and G.P. Bava, “Coupled mode theory: a powerful tool for analyzing complex VCSELs and designing advanced device features,” *IEEE J. Select. Topics Quantum Electron.*, vol. 9, no. 3, pp. 905–917, 2003.

[7] P. Debernardi, J.M. Ostermann, M. Feneberg, C. Jalics, and R. Michalzik, “Reliable polarization control of VCSELs through a monolithically integrated surface grating: a comparative theoretical and experimental study,” *IEEE J. Select. Topics Quantum Electron.*, vol. 11, no. 1, pp. 107–116, 2005.

Toward VCSEL-Based Integrated Optical Traps for Biomedical Applications

Andrea Kroner

A new concept to miniaturise optical trapping and manipulation systems is presented. Integrated optical traps based on top-emitting vertical-cavity surface-emitting lasers (VCSELs) with near-infrared emission in combination with photoresist microlenses were fabricated, characterised and demonstrated. Elevation and trapping of 10 μm-sized polystyrene particles in water is achieved at optical output powers as small as 9 mW.

1. Introduction

The possibility to trap and manipulate micrometer-sized particles by a laser beam was demonstrated for the first time in 1970 [1]. The effect is based on the momentum conservation of photons which are reflected and refracted when hitting a transparent spherical object. Considering a parallel laser beam the interaction leads to the so called scattering force, which pushes the particle forward, parallel to the incident beam. However, if the beam shows an additional transverse intensity gradient, also a force component in the transverse direction is present. Figure 1 illustrates the occurrence of this so-called transverse gradient force with a ray-optical model. When a ray is refracted by a sphere, the associated momentum change of the photons results in an outward oriented force on the particle. If the incident intensity is higher on one side of the sphere, the particle experiences a total force toward the intensity maximum. There the particle remains fixed in the transverse direction due to a vanishing net transverse force. A two-dimensional optical trap is thus established. By tightly focussing a laser beam, even three-dimensional optical trapping can be achieved due to the strong longitudinal intensity gradient and the resulting longitudinal gradient force.

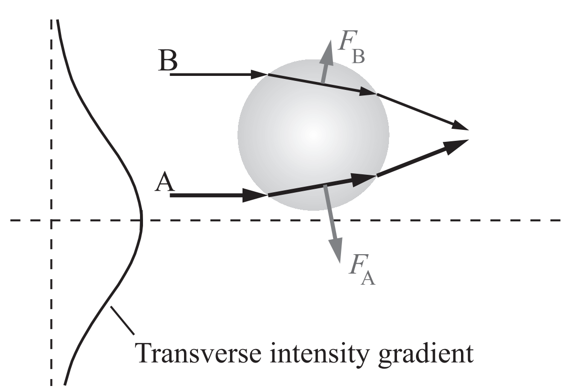

Fig. 1: Origin of the transverse gradient force caused by a parallel laser beam with a transverse intensity gradient. The refraction of the rays A and B leads to the forces F_A and F_B on the particle. Since ray A is stronger than ray B, the net force points toward the intensity maximum.

In recent years, optical trapping has gained increasing attention, especially in the field of biophotonics. Here, the possibility of contact-free optical manipulation of biological material like DNA or cells with forces in the pN range was exploited in mechanical and spectral studies [2] as well as transport and sorting applications [3]. More recently, the use of VCSELs as laser sources in optical trapping systems has attracted particular interest since they are much smaller and less expensive than commonly used Nd:YAG lasers and, unlike edge-emitting laser diodes, require no additional beam corrections. A further advantage of VCSELs is the easy fabrication of monolithic two-dimensional laser arrays, permitting a straightforward implementation of multiple optical traps. VCSEL arrays originally designed for optical communications were used to trap several yeast cells individually at the same time [4], to translate DNA bound to microbeads non-mechanically between traps [5] or to stack polystyrene microspheres [6]. To achieve stable three-dimensional trapping by a tightly focussed laser beam, a high numerical aperture objective was used in all experiments, requiring a comparatively bulky optical setup. In this contribution we present a new concept to reduce the geometrical dimensions by integrating microlenses directly on the laser output facet. With this setup, referred to as integrated optical trap, highly compact two-dimensional optical trapping is achieved.

2. Setup

Figure 2 shows a schematic of the integrated optical trap setup. The system is based on GaAs/AlGaAs top-emitting VCSELs grown by molecular beam epitaxy, with emission wavelengths in the 850 nm range. For current supply a ring contact is placed on top of the upper p-doped Bragg-mirror. The active diameter of the laser is defined by selective oxidation. To focus the VCSEL output beam to a beam waist of some micrometers in diameter, a photoresist microlens is integrated on the output facet, partially covering the contact metallisation. The sample stage, containing the particles to be manipulated, consists of a cover slip and an only 30 µm thick glass substrate, separated by a 50 µm thick polydimethylsiloxane (PDMS) spacer. The stage is placed close to the laser surface at a distance of about 10 µm such that the beam waist of the focussed laser beam is located just above the lower glass substrate.

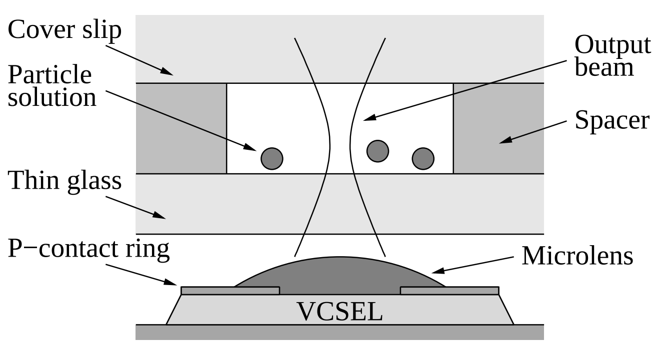

Fig. 2: Schematic of the integrated optical trap setup. The output beam is focussed by a PMGI microlens to manipulate the particles in solution. The liquid is sandwiched between a 30 µm thick glass substrate and a cover slip, which are separated by a 50 µm PMDS spacer.

3. Device Fabrication and Characterisation

After standard VCSEL processing, the microlens consisting of polymethylglutarimide (PMGI) photoresist is fabricated on top of the laser output facet. PMGI is a suitable material for microlenses due to its transparency in the near-infrared spectral region and its high thermal stability compared to other resists. By applying lithographic techniques, small resist islands are placed on top of the lasers, which assume a spherical shape during a thermal reflow process at temperatures above 250 °C. The radius of curvature of the resulting lens is pre-defined by the diameter and thickness of the initial resist island. Depending on the active diameter of the laser, here ranging from 11 to 14 µm, radii of curvature of 20 to 25 µm must be realised in order to achieve the desired beam diameter at the focal point. The inset of Fig. 3 presents an optical microscope image of a completed device, showing the laser mesa with the p-contact ring and the integrated microlens. The lenses were characterised by measuring their surface profile with an atomic force microscope (AFM). The dots in Fig. 3 indicate the AFM data while the solid line shows a spherical fit, revealing a nearly ideal spherical shape with a radius of curvature of about 22 µm.

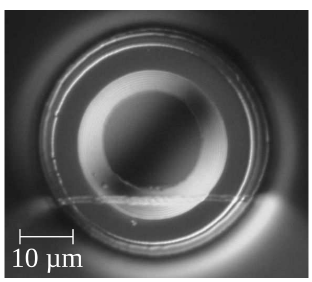

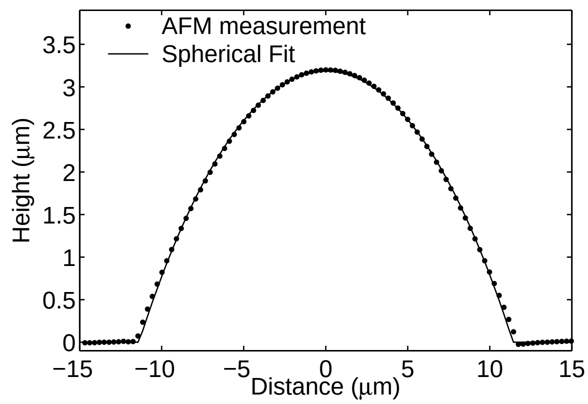

Fig. 3: Microscope image (left) and AFM height profile measurement (right) of a lensed VCSEL. The spherical fit of the AFM data shows a nearly ideal spherical shape of the lens with a radius of curvature of about 22 µm.

In Fig. 4 the operating characteristics of the same device are shown before and after the microlens was placed on its output facet. A small increase of the threshold current as well as of the differential quantum efficiency and the maximum output power is observed, which is caused by the decrease of the upper mirror reflectivity by the microlens material. An optical output power of up to 17 mW is available from this device. The VCSEL has an active diameter of 13.5 µm and shows transverse multimode emission from threshold to thermal rollover with an emission wavelength of about 860 nm.

To confirm the focussing effect of the microlens, the transverse output beam profiles at different distances from the laser surface were measured by scanning the laser beam with a lensed fiber moved by piezo actuators. Figure 5 shows the scanned beam profile at distances from about 0 to 50 µm to the laser surface. A minimum beam diameter of

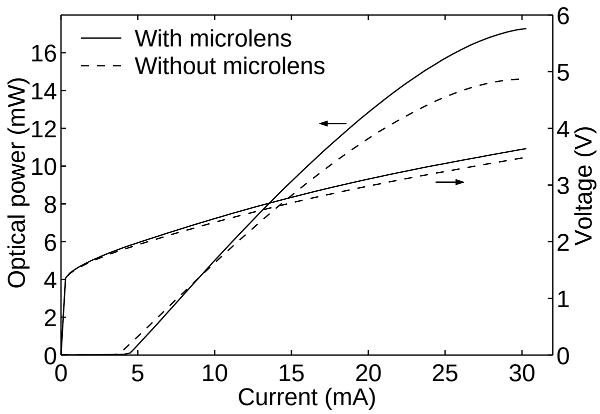

Fig. 4: Light–current–voltage characteristics of a 13.5 µm oxide aperture VCSEL with and without integrated microlens. The increase of threshold current and optical output power is explained by a reduction of the top mirror reflectivity.

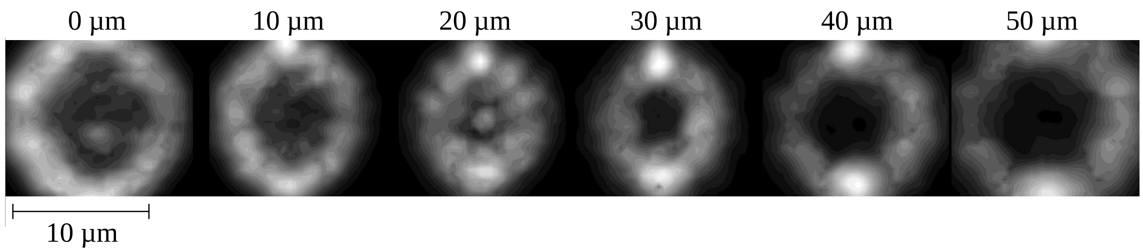

Fig. 5: Measurement of the beam profiles of a lensed device at a current of 6 mA at various distances to the laser surface, ranging from about 0 to 50 µm. The focal point with a beam diameter of about 15 µm and a FWHM of 10 µm is found at a distance of 20 to 30 µm.

about 15 µm and a full-width-at-half-maximum (FWHM) of 10 µm, respectively, at a distance of about 20 to 30 µm (in air) are measured. In contrast, a nominally identical device without lens on the same wafer shows a continuously diverging beam. However, due to multimode emission, both laser types have a doughnut-shaped intensity profile.

4. Results

To examine the suitability of the components in optical trapping applications, the above described device was introduced in the setup shown in Fig. 2. To observe the experiments, an imaging system, mainly consisting of a CCD camera and filters, was placed above the sample stage. The experiments were performed with 10 µm-sized polystyrene particles in water since their physical properties like density and refractive index are comparable with those of biological cells.

Figure 6 shows a typical experimental sequence by means of pictures taken by the CCD camera (top view). For better comparison, corresponding schematic side views are added. Initially the particles are located at the bottom of the sample stage and drift randomly through the liquid (Figs. 6a and 6b). This drift is induced by a constant evaporation of liquid from the sample stage and was not found to be influenced by the emission state of the laser. In the present case the VCSEL emits 9 mW optical output power. When approaching the laser beam, the particle is pulled toward an intensity maximum by the transverse gradient force (Figs. 6c and 6d). Since the laser beam is only mildly focussed, the longitudinal gradient force is not strong enough to overcome the forward scattering force which arises mainly due to reflection of photons at the particle surface. Therefore, the particle is lifted by the laser beam until it reaches the upper cover slip where it remains trapped. The elevation is observable in Figs. 6d and 6e by a blurring of the particle as it moves out of the imaging focus. In Fig. 6f, the focal point of the imaging system is adjusted to show the particle immobilised at the top of the sample stage. When the laser is turned off, it floats back to the bottom. At lower output power deflection and elevation of the particles is still observed while stable trapping at the upper cover slip is no longer achieved. Consistent results for manipulation and trapping were obtained for similar VCSELs. However, a displacement of the trapped particle with respect to the device centre is generally observed, much likely caused by the doughnut-shaped beam profile. To improve the beam quality of the VCSELs, surface relief techniques [7] will be applied as a next step.

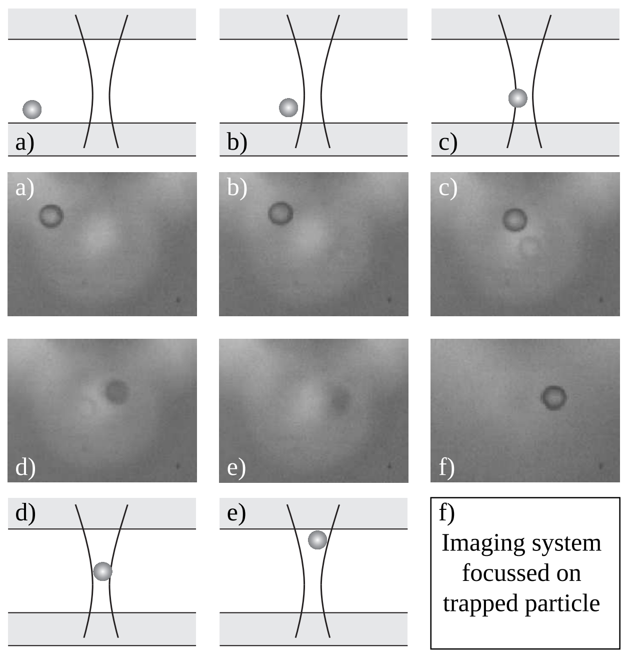

Fig. 6: Sequence of a typical trapping experiment with the integrated optical trap using a 10 μm diameter polystyrene microsphere. For better understanding, top views by the CCD camera as well as associated schematic side views are shown. The approaching particle (a, b) is pulled toward the intensity maximum of the laser beam by the gradient force (c, d) and is pushed upwards by the scattering force (d, e). Finally, it remains trapped at the upper cover slip (f) until the laser is turned of again.

5. Conclusion

We have fabricated photoresist microlenses with nearly ideal spherical shapes on top-emitting GaAs/AlGaAs VCSELs. The good output performance of the devices is not degraded by the lens, while the output beam is focussed to a beam waist of about 10 µm FWHM. With these devices, we have achieved elevation and trapping of 10 µm diameter polystyrene microspheres at output powers as small as 9 mW. Thus, the concept of VCSEL-based integrated optical traps is successfully demonstrated for the first time. By attaching the VCSELs directly to the sample stage and extending the concept to array configurations, miniaturised instruments for cell analysis and sorting appear to be within reach.

References

[1] A. Ashkin, "Acceleration and trapping of particles by radiation pressure," *Phys. Rev. Lett.*, vol. 24, no. 4, pp. 156–159, 1970.

[2] C.M. Creely, G. Volpe, G.P. Singh, M. Soler, and D.V. Petrov, "Raman imaging of floating cells," *Optics Express*, vol. 13, no. 16, pp. 6105–6110, 2005.

[3] K. Ladavac, K. Kasza, and D.G. Grier, "Sorting mesoscopic objects with periodic potential landscapes: optical fractionation," *Phys. Rev. E*, vol. 70, pp. 010901-1–4, 2004.

[4] A.L. Birkbeck, R.A. Flynn, M. Ozkan, D. Song, M. Gross, and S.C. Esener, "VCSEL arrays as micromanipulators in chip-based biosystems," *Biomedical Microdevices*, vol. 5, no. 1, pp. 47–54, 2003.

[5] Y. Ogura, T. Beppu, F. Sumiyama, and J. Tanida, "Toward photonic computing: developing optical techniques for parallel manipulation of DNA," in *Photonics for Space Environments,* E.W. Taylor (Ed.), Proc. SPIE, vol. 5897, pp. 34–43, 2005.

[6] F. Sumiyama, Y. Ogura, and J. Tanida, "Stacking and translation of microscopic particles by means of 2×2 beams emitted from a vertical-cavity surface-emitting laser array," *Appl. Phys. Lett.*, vol. 82, no. 18, pp. 2969–2971, 2003.

[7] H.J. Unold, S.W.Z. Mahmoud, R. Jäger, M. Golling, M. Kicherer, F. Mederer, M.C. Riedl, T. Knödl, M. Miller, R. Michalzik, and K.J. Ebeling, "Single-mode VCSELs," in *Vertical-Cavity Surface-Emitting Lasers VI,* C. Lei, S.P. Kilcoyne (Eds.), Proc. SPIE, vol. 4649, pp. 218–229, 2002.

Complex-Coupled Distributed Feedback Laser Monolithically Integrated With Electroabsorption Modulator and Semiconductor Optical Amplifier

Philipp Gerlach

We report on the design and experimental results of monolithically integrated optoelectronic devices containing distributed feedback (DFB) laser, electroabsorption modulator (EAM), and semiconductor optical amplifier (SOA). Common InGaAlAs multiple quantum well (MQW) layers are used in all device sections. The incorporation of local lateral metal gratings in the DFB section enables device fabrication by single-step epitaxial growth. The emission wavelength is $\lambda = 1.3\,\mu m$. More than $2\,mW$ single-mode fiber-coupled output power as well as $10\,dB/2\,V$ static extinction ratio have been achieved. Modulation experiments clearly show $10\,Gbit/s$ capability.

1. Introduction

EAMs are considered as key components for modern optical telecommunication systems due to very high speed operation capability [1], high extinction at low driving voltage [2], as well as low or even negative chirp [3]. Furthermore, EAMs can be monolithically integrated with other semiconductor components such as DFB lasers and SOAs [4, 5]. The fabrication of DFB laser-integrated electroabsorption modulators (DFB–EAMs) is challenging because both device sections have different requirements on the active material. Therefore, quantum well intermixing or selective epitaxy is commonly used to achieve variable bandgap energies along the longitudinal device direction [4]. In order to eliminate these critical and costly technological steps, the usage of a common active layer in all device sections is a promising alternative approach which requires efficient forward and reverse operation of the active layer [6]. To avoid high residual absorption of the EAMs, the DFB laser wavelength should be positively detuned by a few tens of nanometers with respect to the gain peak [7] which, however, keeps the output power relatively small. DFB–EAMs, additionally integrated with an SOA and using a common active layer, appear to be an optimum solution since they combine the advantages of compactness, modulation speed, and sufficient output power.

2. Device Design

Since steep absorption edges and pronounced excitonic absorption are outstanding features of the InGaAlAs material system, it appears suitable for DFB–EAMs using a common active layer. An extensive study of an adequate active layer design has already

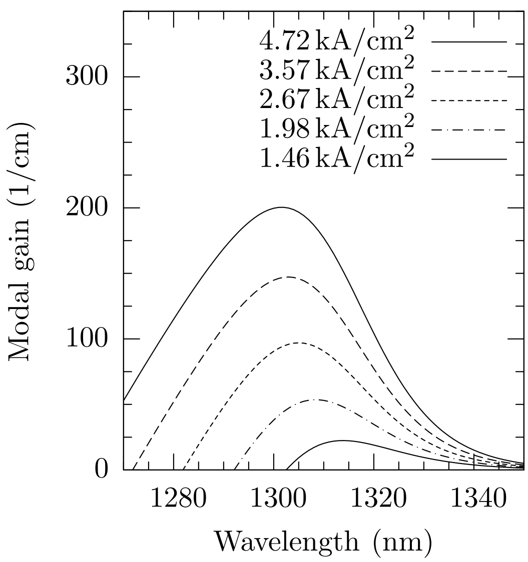

Fig. 1: Simulated modal gain spectra of a 2 µm-wide ridge waveguide structure containing ten 5 nm-thick InGaAlAs QWs at a temperature of $T = 298$ K for several pump current densities.

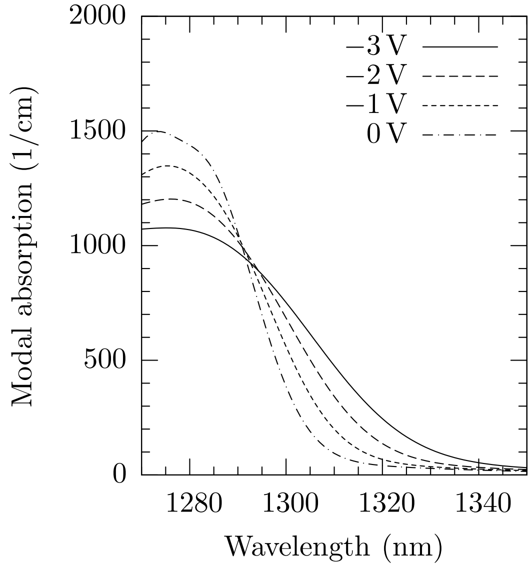

Fig. 2: Simulated modal absorption spectra for several reverse voltages applied to the active region from Fig. 1.

been reported elsewhere [6] and will not be discussed here. We use an epitaxial structure grown on n-doped InP with a 300 nm-thick waveguide layer which contains ten compressively strained AlGaInAs quantum wells (QWs) with a photoluminescence peak at about 1280 nm wavelength. Their two-dimensional confinement factor within a 2 µm-wide ridge waveguide is calculated to be 12 %. The simulated modal gain for several pump current densities is shown in Fig. 1. The corresponding modal absorption characteristic can be seen in Fig. 2. It is clear from these figures that the wavelength of the gain peak at $\lambda \approx 1305$ nm cannot be used as operating wavelength because the modal absorption is too high. An operating wavelength of $\lambda \approx 1320$ nm seems to be a suitable compromise which combines sufficient gain with an appropriate modulation characteristic as well as low residual absorption in the EAM.

2.1 Distributed feedback laser

Stable single-mode operation with narrow linewidth is an important design requirement for DFB lasers. The spectral characteristic of regular index-coupled DFB lasers strongly depends on the facet reflectivities. We use lateral metal gratings in the DFB section to achieve narrow-linewidth complex-coupled DFB lasers with high side-mode suppression ratio. Their fabrication does not require epitaxial regrowth which keeps device fabrication simple. The grating is positioned as indicated in Fig. 3 and interacts with the evanescent field of the guided mode, which is plotted in the same diagram. The calculated imaginary coupling coefficient is $\kappa = \mathrm{i} \cdot 21\,\mathrm{cm}^{-1}$, where $\mathrm{i} = \sqrt{-1}$ is the imaginary unit. Using the transfer-matrix method and neglecting additional facet reflections, the corresponding

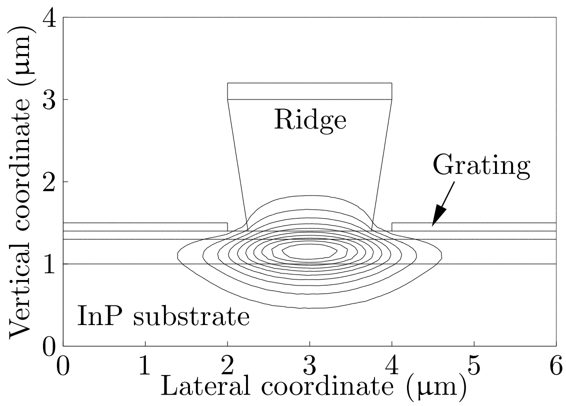

Fig. 3: Simulated transverse mode in the ridge waveguide cross-section including the lateral metal grating.

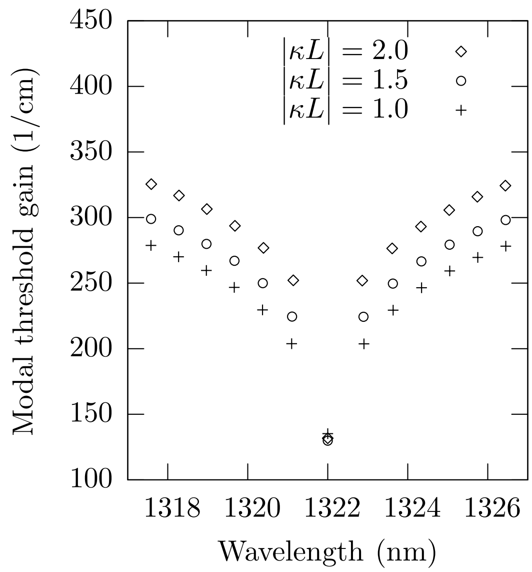

Fig. 4: Longitudinal mode threshold gains of complex-coupled DFB laser with lateral metal grating and negligible facet reflectivities for several coupling strengths $|\kappa L|$.

longitudinal DFB laser modes are calculated [8]. The resulting modes for a DFB laser with different $|\kappa L|$ and a grating period of $\Lambda = 201.3$ nm are indicated in Fig. 4. The mode at the Bragg wavelength of 1322 nm has a modal threshold gain of $130\,\mathrm{cm}^{-1}$ and is expected to lase with a huge side-mode suppression ratio since the modal threshold gain of all other modes is larger by more than $70\,\mathrm{cm}^{-1}$.

2.2 Electroabsorption modulator

Within the EAM section, part of the incident optical power P_{in} is absorbed, while the modal absorption $\tilde{\alpha}$ is controlled by the applied reverse voltage. For a binary signal, the corresponding output power levels are

$$\begin{aligned} P_{\mathrm{out},1} &= P_{\mathrm{in}} \mathrm{e}^{-\tilde{\alpha}_1 l_{\mathrm{EAM}}} \quad , \\ P_{\mathrm{out},0} &= P_{\mathrm{in}} \mathrm{e}^{-\tilde{\alpha}_0 l_{\mathrm{EAM}}} \quad . \end{aligned} \tag{1}$$

Their ratio is defined as extinction ratio

$$\mathrm{ER} = \frac{P_{\mathrm{out},1}}{P_{\mathrm{out},0}} = \mathrm{e}^{-\Delta\tilde{\alpha} l_{\mathrm{EAM}}} \quad . \tag{2}$$

It is obvious from this equation that the modulator length l_{EAM} as well as the modal absorption change $\Delta\tilde{\alpha} = \tilde{\alpha}_1 - \tilde{\alpha}_0$ are important design parameters. Optical transmitter specifications usually demand an extinction ratio of at least ER = 10 dB. Since the modal absorption change $\Delta\tilde{\alpha}$ strongly depends on the operating wavelength, the EAM length l_{EAM} is to be adjusted in such a way that the required ER is reached. For wavelengths in the range of $\lambda = 1302$ nm to $\lambda = 1318$ nm an extinction ratio of at least 10 dB is achieved

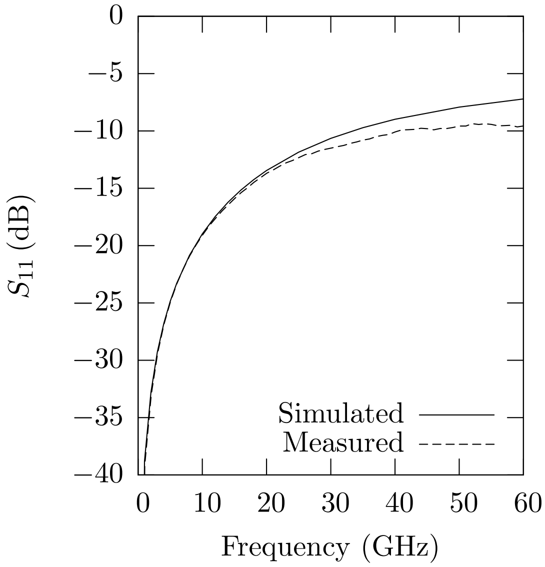

Fig. 5: Simulated and measured electrical reflection coefficient S_{11} for a 100 µm-long EAM as a function of frequency.

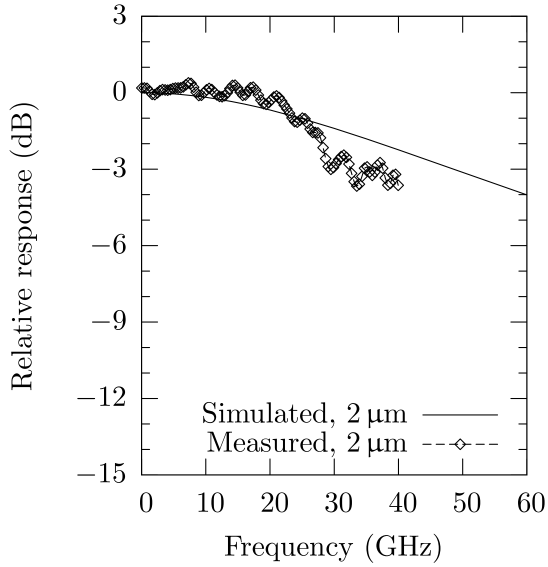

Fig. 6: Simulated and measured electrical–optical response of a 100 µm-long EAM with a 2 µm-wide waveguide as a function of frequency.

by EAMs having a length $l_{\mathrm{EAM}} = 100\,\mu\mathrm{m}$. Longer operating wavelengths require increased EAM lengths to satisfy the demand on extinction due to a decrease of modal absorption change. Even in the on-state, part of the light will be absorbed. Low residual absorption values of approximately $\alpha = 4\,\mathrm{dB}$ are achievable for wavelengths of $\lambda \approx 1322\,\mathrm{nm}$. For this operating wavelength, corresponding to the fundamental mode of the DFB laser discussed in the previous section, an extinction ratio of 10 dB as well as 4 dB residual loss are to be expected.

Not only the static characteristics like extinction ratio and residual loss have to be considered. Since DFB–EAMs are to be used for high-speed optical data transmission, their modulation performance is an important design criterion. Even for operation at modulation frequencies of $f = 40\,\mathrm{GHz}$, EAMs with a length of $l_{\mathrm{EAM}} \approx 100\,\mu\mathrm{m}$ are much shorter than the electrical wavelength of the modulation signal, thus they can be considered as lumped devices. We use a two-dimensional approach to understand the modulation behavior [9, 10]. Unfortunately, the impedance mismatch between the EAM and the commonly used 50 Ω-based microwave system results in a frequency-dependent modulator voltage amplitude. Therefore a parallel 50 Ω resistor is typically used to achieve good impedance matching at least for low frequencies. The calculated and measured electrical reflection coefficients S_{11} of such a configuration are shown in Fig. 5. Simulation and measurement result are in good agreement in the frequency range of interest. The corresponding calculated electrical–optical (EO) response function [9] is depicted in Fig. 6. A measured EO response function of an EAM with the discussed design is contained in the same figure. The small deviations of a few dB at elevated frequencies are explained by the transfer function of the employed photodiode, which could not be included in the calibration of the measurement setup.

2.3 Semiconductor optical amplifier

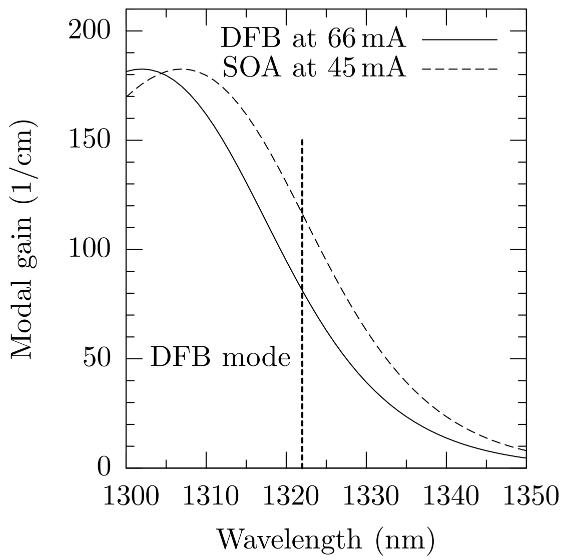

Fig. 7: Simulated modal gain spectra of DFB and SOA sections. Mean section temperatures are found to be $T = 298\,\mathrm{K}$ and $T = 313\,\mathrm{K}$, respectively.

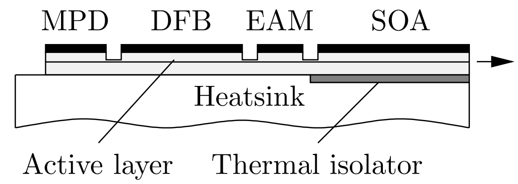

Fig. 8: Schematic of the advanced heatsink design. Due to a decreased thermal conductivity, the mean SOA temperature is increased by $\Delta T = 15\,\mathrm{K}$. MPD indicates a monitor photodiode.

To compensate for the residual losses, a SOA can be integrated in the device as well. Like the DFB section, the SOA section will be forward biased to deliver gain. Unfortunately, the operating wavelength of $\lambda = 1322\,\mathrm{nm}$ does not correspond to the modal gain maximum, as can be seen in Fig. 7. One then expects an increased amplifier noise due to higher spontaneous emission. We try to avoid this by using a specially designed heatsink which is schematically depicted in Fig. 8. It has a spatially varying thermal resistance which is lowest in the DFB and EAM sections. That results in a longitudinally inhomogeneous temperature in the device and particularly in an increased temperature in the SOA section. Therefore the gain spectrum in the SOA is red-shifted, incurring an increased modal gain at the operating wavelength. By measuring the spectral spontaneous emission peak of the SOA, a mean temperature increase of $\Delta T = 15\,\mathrm{K}$ with respect to the gain spectrum of the DFB laser was determined. Both, the gain spectra of the DFB and SOA sections are represented in Fig. 7, considering the difference in mean temperatures.

3. Fabrication

The devices are grown on n-doped InP substrate using metal-organic vapor-phase epitaxy. P-contacts are fabricated first, which later act as mask for ridge etching. Electrical isolation of device sections is realized by small etch trenches, resulting in an electrical separation resistance of $R \approx 25\,\mathrm{k\Omega}$. The employed wet-etch process produces a lateral underetching of approximately 7° (see also Fig. 3) and stops at an etch-stop layer. The

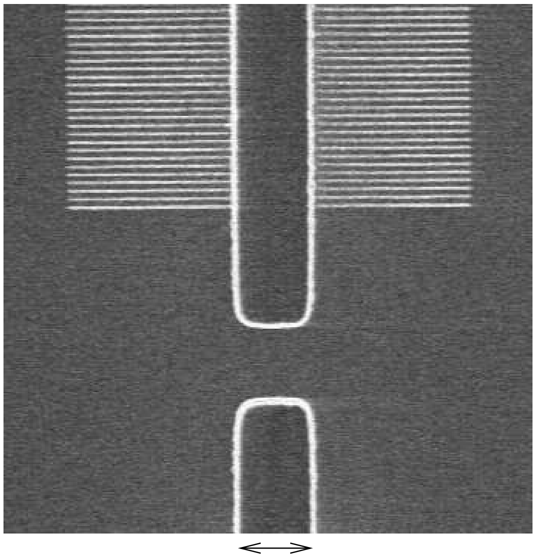

Fig. 9: Scanning electron micrograph of the interface between DFB and EAM sections after ridge etching and lateral grating formation.

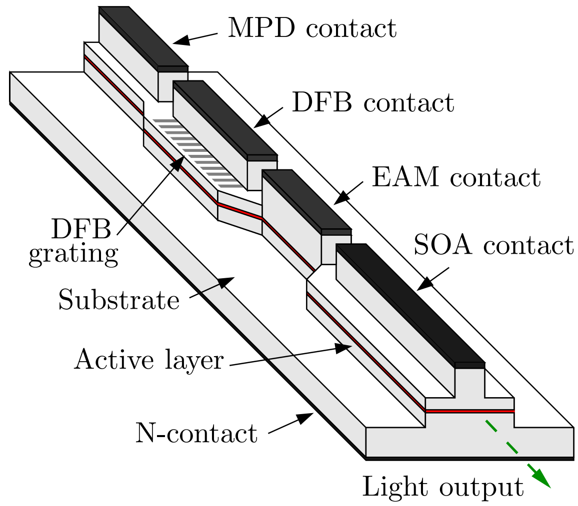

Fig. 10: Schematic of complex-coupled DFB laser integrated with EAM, SOA, and MPD (without passivation and bondpads).

devices consist of a 730 μm-long DFB laser section, a 120 μm-long EAM section, and a 500 μm-long SOA section. Lateral metal gratings are fabricated using electron beam lithography and a lift-off process. We use first-order gratings consisting of 8 nm-thick Ni. Figure 9 shows a scanning electron micrograph of part of a fabricated sample at this stage. A second mesa is etched in order to reduce lateral currents as well as making it feasible to connect the n-doped layers from the top side. After passivation, bond-pad formation, thinning, and cleaving, the samples are mounted on special heatsinks, as discussed in the previous section. A quarter-wave Al_2O_3 antireflection coating is deposited on the front facet in order to avoid back-reflections. Figure 10 shows a schematic of the fabricated devices. In order to reduce the influence of the rear facet on the DFB laser, an additional device section serving as a monitor photodiode (MPD) has been integrated as well. Thus, the light emitted from the DFB laser section to the rear is absorbed instead of being reflected. In addition, the photocurrent is used to verify proper DFB laser operation.

4. Experimental Results

All measurements have been performed at room temperature. Device sections are electrically contacted by probe tips and microwave probes. The optical output power is coupled into a standard single-mode fiber (SSMF) using a lens-integrated isolator. Experimental results show a threshold current of 160 mA, an emission peak at $\lambda = 1322$ nm wavelength, and more than 30 dB side-mode suppression ratio. The measured optical output spectrum for 210 mA laser current, −2 V EAM bias, and 50 mA SOA current is shown in Fig. 11. As can be deduced from the static characteristics in Fig. 12, more than 10 dB/2 V extinction and 2 mW fiber-coupled output power are obtained. Modulation experiments at a data rate of 10 Gbit/s using a pseudorandom bit sequence with a word length of $2^7 - 1$ are

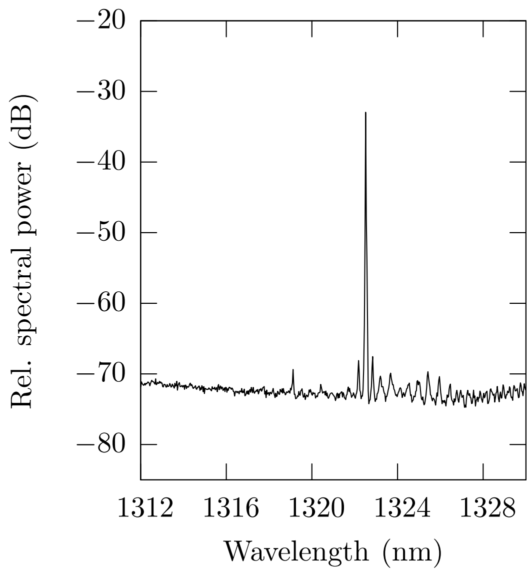

Fig. 11: Measured optical output spectrum for 210 mA laser current, −2 V EAM bias, and 50 mA SOA current.

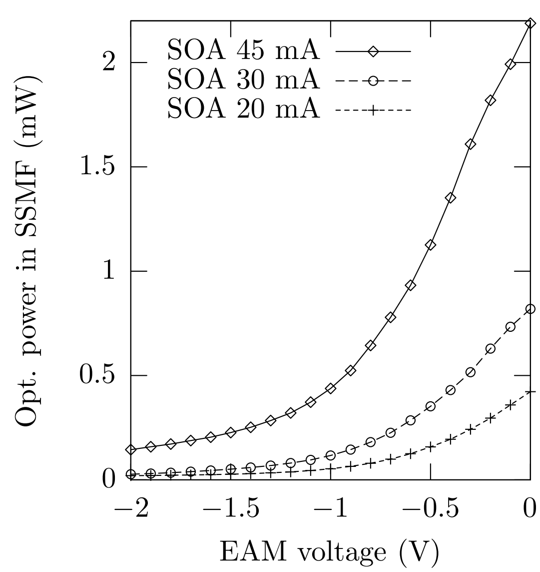

Fig. 12: Measured fiber-coupled optical power versus EAM voltage for 210 mA laser current and several SOA currents.

performed. For 210 mA laser current, −1 V EAM bias, and 50 mA SOA current, the open eye in Fig. 13 is obtained. However, the noise in the on-state limits the signal quality and might be decreased by an improved electrical isolation between the sections as well as a multilayer antireflection coating.

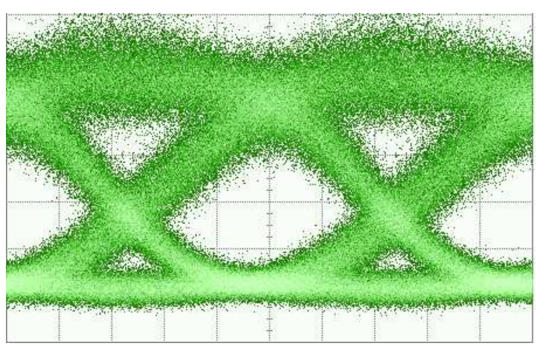

Fig. 13: Filtered eye pattern for 10 Gbit/s modulation with $V_{\mathrm{pp}} = 2\,\mathrm{V}$ amplitude. Laser current is 210 mA, EAM bias is −1 V, and SOA current is 50 mA. The filter bandwidth is 7 GHz.

Acknowledgments

The author would like to thank Josef Rieger for epitaxial growth, Thomas Wenger and Roberto Macaluso for chip technology, Brem Kumar Saravanan for measurement support, and Martin Peschke for simulations, all at Infineon Technologies AG, Munich. Thanks are also due to Steffen Lorch for coating technology and Yakiv Men for electron beam lithography, both at Ulm University.

References

[1] R. Lewen, S. Irmscher, U. Westergren, L. Thylen, and U. Eriksson, "Ultra high-speed segmented traveling-wave electroabsorption modulators", in Proc. *Optical Fiber Communications Conf., OFC 2003*, postdeadline paper PD38. Atlanta, GA, USA, February 2003.

[2] H. Fukano, M. Tamura, T. Yamanaka, Y. Kondo, and T. Saitoh, "Very low driving-voltage 40 Gbit/s electroabsorption modulators", in Proc. *European Conference on Optical Communication, ECOC 2004*, vol. 1, pp. 88–89. Stockholm, Sweden, September 2004.

[3] J.W. Raring, E.J. Skogen, S.P. DenBaars, and L.A. Coldren, "Demonstration of negative chirp characteristics over wide wavelength range using monolithically integrated SG-DBR/electroabsorption modulator", *Electron. Lett.*, vol. 40, pp. 1599–1600, 2004.

[4] Y.H. Kwon, J.S. Choe, J.S. Sim, S.B. Kim, K.S. Choi, and B.S. Choi, "40 Gb/s traveling-wave electroabsorption modulator-integrated DFB lasers by selective area growth", in Proc. *Tenth Optoelectronics and Communications Conference, OECC 2005*, pp. 316–317. Seoul, Korea, July 2005.

[5] B. Xiong, J. Wang, L. Zhang, J. Tian, C. Suan, and Y. Luo, "High-speed ($>$ 40 GHz) integrated electroabsorption modulator based on identical epitaxial layer approach", *IEEE Photon. Technol. Lett.*, vol. 17, no. 2, pp. 327–329, 2005.

[6] M. Peschke, T. Knoedl, and B. Stegmueller, "Simulation and design of an active MQW layer with high static gain and absorption modulation", in Proc. *Numerical Simulation of Semiconductor Devices, NUSOD 2003*, pp. 15–16. Tokyo, Japan, October 2003.

[7] B.K. Saravanan, P. Gerlach, M. Peschke, T. Knoedl, R. Schreiner, C. Hanke, and B. Stegmueller, "Integrated DFB laser electro-absorption modulator based on identical MQW-double-stack active layer for high-speed modulation beyond 10 Gbit/s", in Proc. *16th International Conference on Indium Phosphide and Related Materials, IPRM 2004*, pp. 236–238. Kagoshima, Japan, May 2004.

[8] H. Ghafouri-Shiraz and B.S.K. Lo, *Distributed feedback laser diodes.* New York: J. Wiley & Sons 1996.

[9] P. Gerlach, M. Peschke, C. Hanke, B.K. Saravanan, and R. Michalzik, "High-frequency analysis of laser-integrated lumped electroabsorption modulators", *IEE Proceedings Optoelectronics*, vol. 152, pp. 125–130, 2005.

[10] P. Gerlach, "DFB laser integrated electroabsorption modulators", *Annual Report 2003*, pp. 65–70. Ulm University, Optoelectronics Department.

Wide Temperature Operation of 40 Gbps 1550 nm Electroabsorption Modulated Lasers

Brem Kumar Saravanan and Philipp Gerlach*

Electroabsorption modulated lasers (EMLs) exploiting the quantum confined Stark effect need thermo-electric coolers to achieve stable output power levels and dynamic extinction ratios. Temperature independent operation is reported between 20°C and 70°C for InGaAlAs/InP based monolithically integrated 1550 nm EMLs exploiting a shared active area at 40 Gbps by actively controlling the electroabsorption modulator bias voltage. Dynamic extinction ratios of at least 8 dB and fiber-coupled mean modulated optical power of at least 0.85 mW are obtained over the mentioned temperature range.

1. Introduction

Electroabsorption modulators (EAMs) integrated with distributed feedback (DFB) lasers popularly referred to as electroabsorption modulated lasers (EMLs), have been widely studied for data rates above 10 Gbps. In such EMLs, light modulation in the EAM section is achieved by controlling the optical absorption coefficient by means of an external bias. EAMs employing a quantum well active layer exploit the quantum confined Stark effect (QCSE) [1] to accomplish efficient light modulation close to the EAM band edge. Well designed QCSE based EAMs allow for device lengths in the range of 75–150 μm achieving high-speed operation without compromising extinction ratios. Other salient features include reduced chirp [2] and low drive voltage swings [3]. Wide temperature operation of such EMLs, highly desirable for integrating with low power consumption small form factor modules, has been demonstrated up to 10 Gbps by actively controlling the EAM bias. Demonstrated approaches include vertical power transfer between waveguides [4], selective growth [5] and butt-joint [6] techniques. In contrast to the above approaches, shared active area EMLs, i.e., EMLs exploiting an identical active area for both laser and modulator sections reduce the fabrication complexity considerably [7] and simultaneously boost final yield. In this letter, a 40 Gbps wide temperature operation of EMLs employing a shared active area emitting in the 1550 nm wavelength window is presented.

2. Device Layer Structure

The EMLs employed for the investigations consist of a monolithically integrated DFB laser and an EAM. The EMLs exploit a dual quantum well type active area based on the

*Work performed in collaboration with Infineon Technologies AG, Munich, Germany

InGaAlAs/InP material system. The multiple quantum well (MQW) active layer consists of eight 7.5 nm thick quantum wells whose photoluminescence (PL) wavelength λ_{PL} is around 1510 nm and three 5 nm thick quantum wells with λ_{PL} around 1540 nm. The +0.95 % compressively strained quantum wells are separated by 8 nm thick −0.5 % tensile strained InGaAlAs barriers ($\lambda_{\mathrm{g}} = 1.1\,\mu$m). The intrinsic active layer is embedded between 30 nm thick InGaAlAs ($\lambda_{\mathrm{g}} = 1.05\,\mu$m) separate confinement heterostructures (SCHs) lattice matched to InP. The salient features of using an identical dual multiple quantum well active layer are reported elsewhere [8]. The operation wavelength of the EML is near 1560 nm at room temperature. The wavelength detuning of the EML — defined as wavelength separation between the absorption edge of the EAM and the operation wavelength — is about 55 nm at room temperature. For investigations, the fabricated EMLs were mounted p-side up on copper (Cu) heat sinks. The lengths of DFB laser and EA modulator sections are 380 µm and 115 µm, respectively.

3. Temperature Dependence

Owing to the characteristic steep absorption slope close to the band edge, QCSE based EAMs are inherently sensitive to temperature [9]. With increasing temperature, the transition energy between the electron ground state and heavy hole ground state decreases. This reduction in the transition energy with temperature can be adequately explained by the empirical Varshni relations [10, 11]. The corresponding experimental shift of the EAM absorption spectrum with temperature, in the 1550 nm wavelength window, is ≈ 0.5–0.6 nm/ °C. Simultaneously, with rise in temperature, the modal effective refractive index $\langle n'_{\mathrm{eff}} \rangle$ in the laser section increases by $\approx 2.1 \cdot 10^{-4}$/ °C. This results in a red shift of the operation wavelength, λ_{DFB}, by ≈ 0.1 nm/ °C. The net effect is a decrease of the detuning between the absorption edge of the EAM and the laser emission wavelength by ≈ 0.4–0.5 nm/ °C. This considerably degrades the EML dynamic performance in the absence of any temperature control as illustrated in Fig. 1. A nonreturn-to-zero (NRZ) pseudo-random binary sequence drive signal (Fig. 1a) of word length $2^{11} - 1$ was applied to the input port of the EAM traveling wave electrode with the output port terminated by a

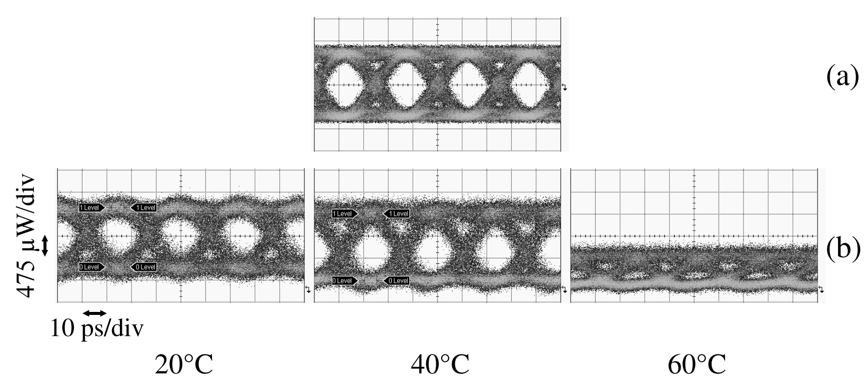

Fig. 1: Electrical drive signal with a peak-to-peak modulation voltage $\mathrm{V_{pp}} = 2.5$ V (a). Experimental 40 Gbps optical eye diagrams with $V_{\mathrm{EAM}} = -2.5$ V and $I_{\mathrm{LD}} = 80$ mA (b). The operating temperature of the EML is indicated below the corresponding eye diagrams.

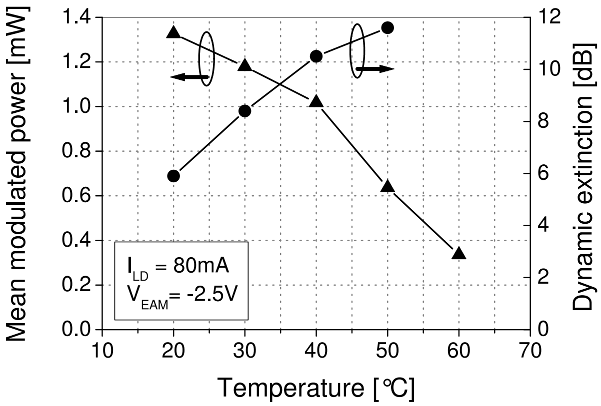

Fig. 2: Mean modulated fiber-coupled optical power and corresponding dynamic extinction ratios as a function of temperature at a constant EAM bias of −2.5 V.

50 Ω resistor. The peak-to-peak modulation swing was $V_{pp} = 2.5\,V$. Fig. 1b shows the recorded optical eye diagrams at 40 Gbps with the EAM biased at −2.5 V for a laser current of 80 mA. Temperature-dependent average power and dynamic extinction of the large-signal results are summarized in Fig. 2. The temperature values correspond to the active layer temperature (or junction temperature) measured with an accuracy of ±0.1 °C. The mean modulated (average) optical power in fiber dropped from 1.3 mW at 20 °C to about 0.36 mW at 60 °C. This drop in optical power is predominantly attributed to the increase of "ON" state insertion loss at the operating wavelength. On the contrary, the dynamic extinction ratio increases from about 6 dB at 20 °C to nearly 12 dB at 50 °C. This is simply the result of increasing absorption swing with decreasing wavelength detuning, which is however obtained at the expense of optical power. The chosen EAM bias voltage delivers an optimum performance at 40 °C with more than 10 dB dynamic extinction and a mean modulated optical power of 1.0 mW in fiber. For temperatures above 50 °C, no reliable estimate of the dynamic extinction was possible due to low available power.

4. Wide Temperature Operation

From the large-signal modulation results presented in the previous section, it is evident that a constant EAM bias voltage does not offer satisfactory performance over a wide temperature range of interest. In order to investigate the possibility of temperature-independent operation, static extinction measurements were performed, by varying the heat sink temperature. The corresponding experimental results are presented in Fig. 3. Static light extinction of at least 20 dB per 3 V was obtained. Most notably, the maximum extinction slope shifts toward low reverse bias voltages with increasing temperature. For instance, the maximum extinction slope occurs near −2.85 V at 20 °C while for the case of 65 °C it occurs near −1.55 V. This shift of the optimum bias point with temperature is empirically fit to yield the relation

$$V_{\mathrm{EAM}} \approx -3.5\,\mathrm{V} + 0.03\,T\,\frac{\mathrm{V}}{^\circ\mathrm{C}}; \quad 20\,^\circ\mathrm{C} \le T \le 70\,^\circ\mathrm{C} \quad . \tag{1}$$

From (1) it is evident that the optimum EAM bias voltage increases by 0.3 V per 10 °C rise in temperature. By actively controlling the EAM bias voltage in accordance with

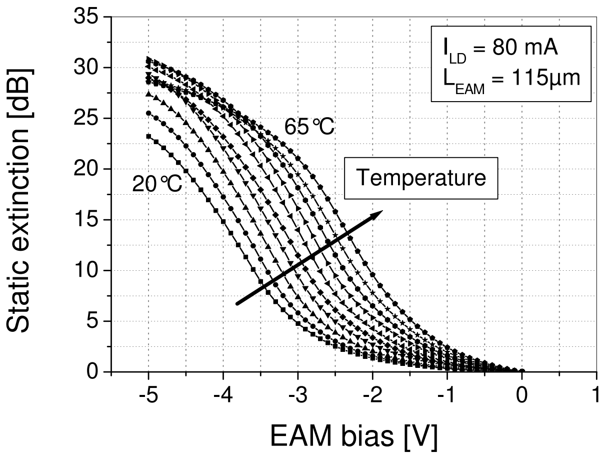

Fig. 3: Static light extinction curves of the 1550 nm EML in steps of 5 °C. Measurements pertain to a laser current of 80 mA.

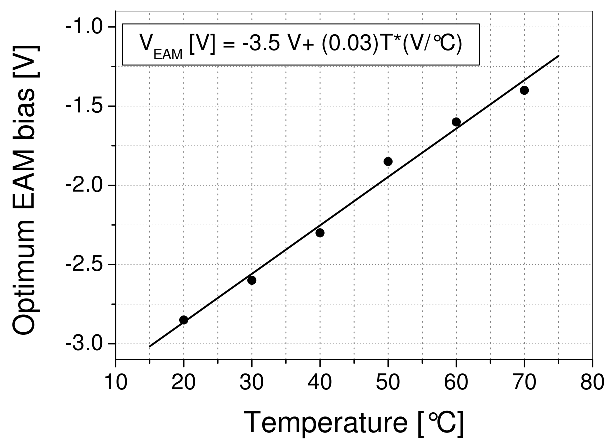

Fig. 4: Linear empirical fit for active EAM bias control to achieve wide temperature operation. The solid circles correspond to the bias voltages used for the measurements.

the temperature, one can expect that average optical power and dynamic extinction remain constant. A plot of the empirical fit is shown in Fig. 4. The solid circles in Fig. 4 correspond to the EAM bias voltages used for subsequent large-signal modulation measurements presented in Fig. 5. The empirical relationship given by (1), is applicable between 20 °C and 70 °C.

The average fiber-coupled optical power and the corresponding dynamic extinction ratios have been summarized in Fig. 6. It is quite evident that the average power and the dynamic extinction remain almost constant from 20 °C to 70 °C. Dynamic extinction ratios of at least 8 dB and an average fiber-coupled optical power of at least 0.85 mW can be observed. The optical eye diagrams obtained in all the measurements were limited by the quality of the electrical drive signal which in part degraded the obtained dynamic extinction. Thus, the dynamic extinction values obtained can be treated as a lower bound. For commercial datacom applications, besides average optical power and dynamic extinction, dispersion penalty of the EMLs has to be fairly constant over the temperature range of interest. Accordingly, the transmission performance of the EMLs shall be addressed after investigations.

5. Conclusion

Temperature-independent operation of monolithically integrated InGaAlAs/InP based electroabsorption modulated lasers employing an identical active layer has been experimentally demonstrated between 20 °C and 70 °C in the 1550 nm wavelength window at a data rate of 40 Gbps. This was achieved by actively controlling the reverse bias voltage applied across the electroabsorption modulator. Average fiber-coupled power of at least 0.85 mW and dynamic extinction ratios of at least 8 dB for a voltage swing of 2.5 V were obtained from 20 °C to 70 °C. The experimental results demonstrate the excellent dy-

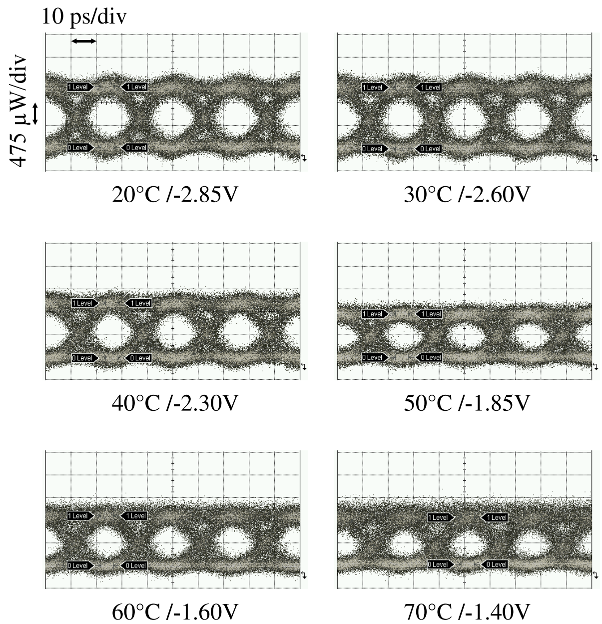

Fig. 5: Experimental 40 Gbps eye diagrams of the 1550 nm EML with active bias control. The peak-to-peak modulation voltage was V_{pp} = 2.5 V with the laser biased at 80 mA. The operating temperature of the EML and the corresponding EAM bias are indicated below the eye diagrams.

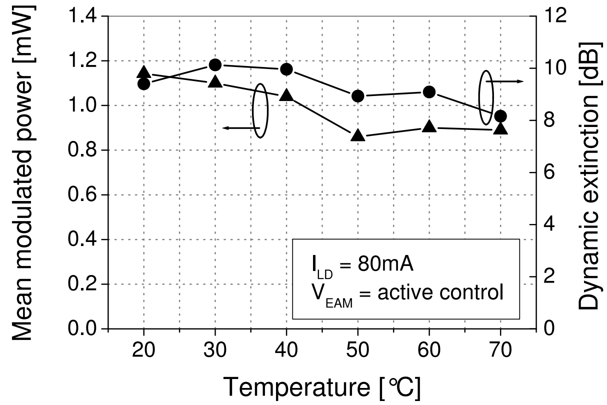

Fig. 6: Mean modulated fiber-coupled optical power and corresponding dynamic extinction ratios of 40 Gbps large-signal modulation results. By actively controlling the EAM bias, dynamic extinction and average fiber power stay reasonably constant from 20 °C to 70 °C.

namic performance of the devices and their potential for next generation high-speed data links.

Acknowledgment

The authors would like to thank Josef Rieger for epitaxial growth and Joerg Adler for grating technology all with Infineon Technologies in Munich, Germany.

References

[1] K.J. Ebeling, *Integrated Optoelectronics*. Berlin: Springer Verlag, 1993.

[2] K. Morito, R. Sahara, K. Sato, and Y. Kotaki, "Penalty-free 10 Gb/s NRZ transmission over 100 km of standard fiber at 1.55 μm with a blue-chirp modulator integrated DFB laser," *IEEE Photon. Technol. Lett.*, vol. 8, no. 3, pp. 431–433, 1996.

[3] B.K. Saravanan, C. Hanke, T. Knoedl, M. Peschke, R. Macaluso, and B. Stegmueller, "Integrated InGaAlAs/InP laser-modulator using an identical multiple quantum well active layer," *Proc. SPIE,* vol. 5729, pp. 160–169, 2005.

[4] M.R. Gokhale, P.V. Studenkov, J. Ueng-McHale, J. Thomson, J. Yao, and J. van Saders, "Uncooled, 10 Gb/s 1310 nm electroabsorption modulated laser," in Proc. *OFC'03*, Atlanta, Georgia, USA, Mar. 2003, postdeadline paper PD42.

[5] H. Chida, K. Yashiki, K. Tsuruoka, R. Kobayashi, S. Sudo, K. Sato, T. Kato, and K. Kudo, "10-Gb/s — 23-km penalty-free operation of 1.3-µm uncooled EML by narrow-stripe selective MOVPE," in Proc. *ECOC'04*, Stockholm, Sweden, Sep. 2004, paper Mo4.4.7.

[6] S. Makino, K. Shinoda, T. Kitatani, T. Tsuchiya, M. Aoki, N. Sasada, K. Uchida, K. Naoe, and K. Uomi, "Wide temperature range (0 to 85°C), 40-km SMF transmission of a 1.55-µm, 10-Gbit/s InGaAlAs electroabsorption modulator integrated DFB laser," in Proc. *OFC'05*, Anaheim, California, USA, Mar 2005, postdeadline paper PDP14.

[7] A. Ramdane, F. Devaux, N. Souli, D. Delprat, and Ougazzaden, "Monolithic integration of multi-quantumwell lasers and modulators for high-speed transmission," *IEEE J. Quantum Electron.*, vol. 2, no. 2, pp. 326–335, 1996.

[8] T. Knoedl, C. Hanke, B.K. Saravanan, M. Peschke, R. Schreiner, and B. Stegmueller, "Integrated 1.3 µm InGaAlAs-InP laser–modulator with double-stack MQW layer structure," *Proc. SPIE,* vol. 5451, pp. 1–7, 2005.

[9] L. Coldren and S. Corzine, *Diode Lasers and Photonic Integrated Circuits*. New York, USA: Wiley, 1995.

[10] I. Vurgaftman, J.R. Meyer, and L.R. Ram-Mohan, "Band parameters for III-V compound semiconductors and their alloys," *J. Appl. Phys.*, vol. 89, no. 11, pp. 5815–5875, 2001.

[11] N.C. Frateschi, J. Zhang, R. Jambunathan, W.J. Choi, C. Ebert, and A.E. Bond, "Uncooled performance of 10-Gb/s laser modules with InGaAlAs-InP and InGaAsP-InP MQW electroabsorption modulators integrated with semiconductor amplifiers," *IEEE Photon. Technol. Lett.*, vol. 17, no. 7, pp. 1378–1380, 2005.

Transmitter Components for THz Applications and a Simple Setup for THz Spectroscopy

Wolfgang Schwarz and Philipp Gerlach

We present a setup for THz time-domain spectroscopy (THz-TDS). It is capable of determining material transmission properties in the electromagnetic spectral range from 100 to 1000 GHz. Microantennas structured on photoconductive low-temperature grown gallium arsenide (LT-GaAs) act as transmitters and receivers. The photoconductive LT-GaAs layer is grown by molecular beam epitaxy.

1. Introduction

During the last two decades, fast pulsed lasers with pulse durations below 1000 fs have prepared the ground for the generation of short electromagnetic pulses. In such femtosecond laser systems a pulse duration of 1000 fs corresponds to a frequency of $f = 1\,\text{THz}$ (10^{12} Hz), that is unattainable with typical electrical microwave circuits. From an optics point of view, THz radiation with wavelengths between 1 mm and 100 µm is often called "far infrared". Not only this term indicates that in optics THz radiation was for a long period out of scope[2]. Hence THz technology is a relatively new and challenging field in research.

One of the first THz transmitters was reported by Auston [3] in the 1970s followed by a vast number of publications on this topic, introducing the THz time-domain spectroscopy. Free electric charge q can be generated by laser irradiation of a semiconductor. An electromagnetic dipole with the dipole moment $\vec{p} = q\vec{l}$ is formed when the electric charge is separated in the distance $l = \left|\vec{l}\right|$. According to Maxwell's theory, accellerated charge is the origin of an electromagnetic wave. The acceleration of the charge can be achieved in an externally applied static electric field, as sketched in Fig. 1. The electric field at a large distance to the irradiation spot is then expressed as

$$\vec{E}(\vec{r},t) \propto \frac{1}{r}\left[\left(\frac{\partial^2 \vec{p}}{\partial t^2} \times \vec{n}\right) \times \vec{n}\right] \; , \tag{1}$$

where $\vec{n} = \vec{r}/r$ represents the unity directional vector from $\vec{p}$ to a point $\vec{r}$ in space.

A THz detector is illustrated in Fig. 2. It relies on the reverse process by utilizing a method called *optical gating*. The incident THz wave excites the microstructured dipole

[2]First experiments were reported one century ago by a group led by Heinrich Rubens and Ernest Fox [1, 2]. However, subsequent intensive investigations were delayed owing to the lack of a bright and coherent light source.

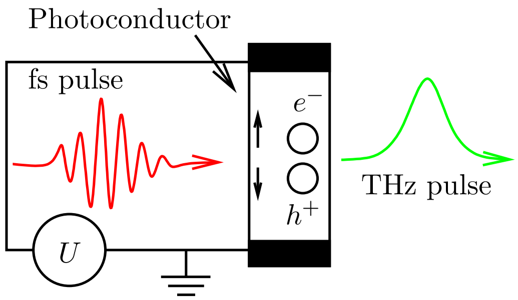

Fig. 1: Simplified THz transmitter irradiated by a fs laser pulse. The generated free carriers are accelerated in the bias field, radiating a THz pulse.

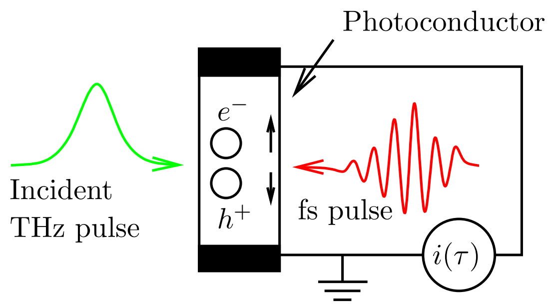

Fig. 2: Schematic drawing of a dipole connected to an ampere meter. Depicted are the incident THz beam and the fs laser pulse which generates free carrier pairs in the irradiated photoconductor.

antenna on the semiconductor surface. A photoconductive gap in the center of the antenna is irradiated by a laser pulse, generating free carriers and thus electrical conductivity. The resulting photocurrent $i(\tau)$ after one THz cycle T is expressed by the convolution

$$i(\tau) \propto \frac{1}{T}\int_0^T E(t)\sigma(\tau - t)\,\mathrm{d}t \tag{2}$$

of the incident THz field $E(t)$ and the electric conductivity $\sigma(t)$ within the photogap. Commonly the laser pulse is shorter (i.e. δ-shaped in the ideal case) than the sampled THz pulse, so temporally fine resolved sampling is in accordance with the Nyquist–Shannon criterion for the minimum sampling frequency [4].

2. Scaling and Design of the Transmitter

Designing the radiative dipole antennas, both simulations and simple analytical approaches were employed. A simple ideally conductive metal stripe dipole with length l and width w is considered, as sketched in Fig. 3. The dipole is sectioned into microstrips labeled “1” and “2”. These are separated by a non-conductive photogap with width $s = 5\,\mu$m, on which the laser beam is focused. The substrate depicted in Fig. 4 consists of $100\,\mu$m-thick GaAs (relative permittivity is $\epsilon_\mathrm{r} = 12.6$, neglecting absorption), the top side metallization is 100 nm thick. Regarding microstrip line and substrate, the effective refractive index of the structure can be approximated by $n_\mathrm{eff} = \sqrt{(1+\epsilon_\mathrm{r})/2}$ [5]. For an angular frequency $\omega = 2\pi f$, the dipole length l should satisfy

$$l = \lambda/(2n_\mathrm{eff}) = (\pi c)/(\omega n_\mathrm{eff}) \tag{3}$$

with c and λ as the vacuum velocity of light and vacuum wavelength, respectively.

For comparison, a numerical simulation was performed with *ADS Momentum Solver* from Agilent. The simulated dipole lengths are 30 and $50\,\mu$m, the width $w = 20\,\mu$m. In Fig. 5 the simulation result within the 0 to 2 THz frequency range is shown in the Smith chart. The longer antenna exhibits a resonance at a frequency of 1.481 THz, whereas the short antenna does not show any resonance in the considered spectral range. Under the assumption that the source impedance of the photogap is 100 kΩ [5], source and antenna are insufficiently impedance matched. When evaluating (3) for the resonance frequency, the calculation yields 1.15 THz for the given 50 μm-long structure. The deviation between analytic and simulated result is explained by stray edge capacitances at each end of a microstrip which are not considered in the analytic formula for the resonance frequency.

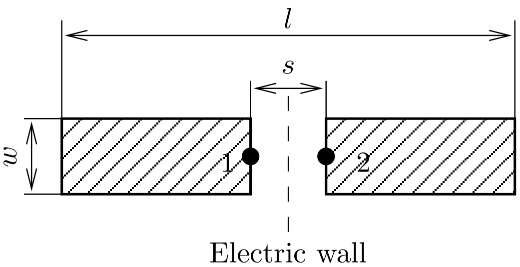

Fig. 3: Sketch of the simulated dipoles. The dimensions of the microstructured metallization are indicated.

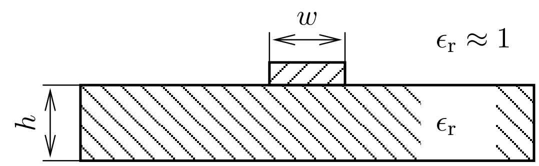

Fig. 4: Sketched cross-section of the simulated dipoles. The structure is surrounded by air with relative permittivity $\epsilon_r \approx 1$.

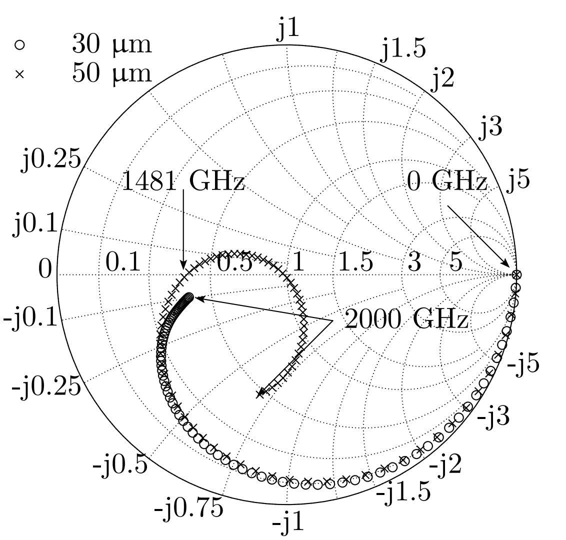

Fig. 5: Simulated amplitude reflection factor of the dipoles for 50 Ω reference impedance. The simulated antennas have lengths of 30 and 50 μm.

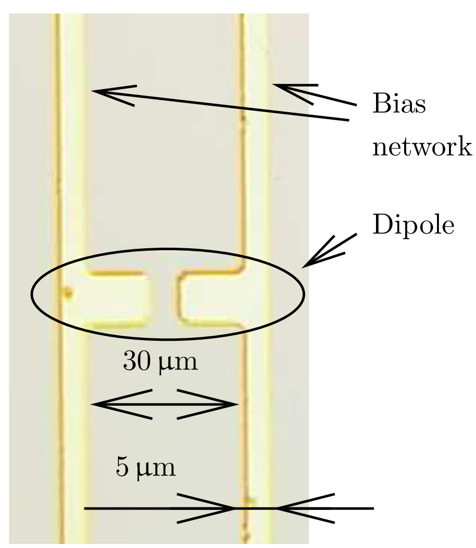

Fig. 6: Photograph of the dipole structure used as a detector.

3. Experimental Approach

3.1 Setup for THz time-domain spectroscopy

In contrast to the commonly applied far-infrared Fourier transform spectroscopy [6], the presented THz-TDS [3, 7] is capable of a transient analysis of material exposed to electromagnetic waves. The simplified setup is shown in Fig. 7. A fs laser pulse is split by beam splitter BS into an emitter and detector beam. The emitter beam is deflected by two mirrors M1 and M2 and is then focused onto the transmitter chip. The transmitter dipole radiates a THz pulse, which is outcoupled through the GaAs substrate and partly collimated by a silicon lens. The beam is deflected by two parabolic mirrors (P1, P2) onto the detector. A second silicon lens focuses the THz beam onto the photoconductive gap in the detector. Moving the retroreflector varies the time delay between the emitter and detector beam. In the detector the laser radiation from the detector beam creates an electric conductivity, which reads out the incident THz field according to (2). For each delay τ, the photocurrent $i(\tau)$ is measured and so the time trace of the THz pulse is determined. To measure the relative transmission of a sample, a reference sweep is performed with the delay line and for each time step the photocurrent is sampled. Subsequently the sample is introduced into the THz beam between the two parabolic mirrors and a second sweep is made. The pulsed laser *Coherent Mira 900 D* is pumped by an argon ion laser (*Coherent Innova 400-15*). The laser source is operated at 830 nm wavelength and delivers pulses with 190 fs autocorrelation length at a repetition rate of about 76 MHz. An optical filter and the combination of a $\lambda/4$ plate and a polarizer attenuates the average laser power to 5 mW incident both onto transmitter and detector. During the experiment the transmitter beam is optically chopped at a frequency of 1.4 kHz and the photocurrent is measured by a lock-in amplifier.

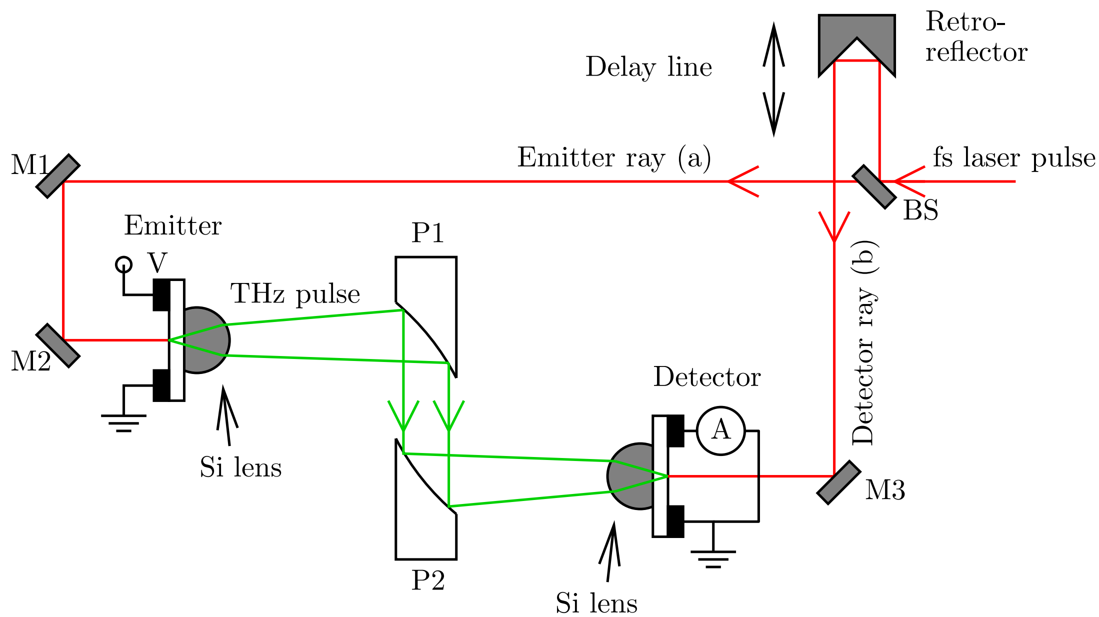

Fig. 7: Schematic setup for THz time-domain spectroscopy.

3.2 Transmitter and detector

We have fabricated a pair of transmitter and detector. The semi-insulating GaAs substrate is 350 μm thick. A 2 μm-thick GaAs layer was grown by molecular beam epitaxy at 200 and 160 °C for the transmitter and detector, respectively. The samples were post-annealed for 10 min. at 600 °C in the growth chamber in order to maintain excess As ambient pressure. Two coplanar striplines microstructured on the LT-GaAs form the emitter dipole. The distance between the striplines is 50 μm. The detector consists of a double-T arrangement as depicted in Fig. 6. The length of the dipole is 30 μm in total. The metallization was vacuum evaporated and annealed for 2 min. at 400 °C in N_2 atmosphere.

4. Experimental Results

We measured the resulting photocurrent in the detector for different positions x_i of the delay line, and calculated a corresponding time delay $\tau_i = 2x_i/c$. The photocurrent burst between 0 and 8 ps in Fig. 8 clearly relates to the applied DC bias voltage at the emitter, which was set to 20 or 45 V. Despite of the poor signal-to-noise ratio we could reproduce the measurements achieving the same characteristic pulse shape. The latter vanished when the THz beam path was blocked. Thus we conclude that the measured photocurrent corresponds to the incident THz wave. The inset in Fig. 8 shows the Fourier-transformed spectrum of the burst. A characteristic plateau between 100 and 500 GHz is visible, which can be distinguished from the noise floor.

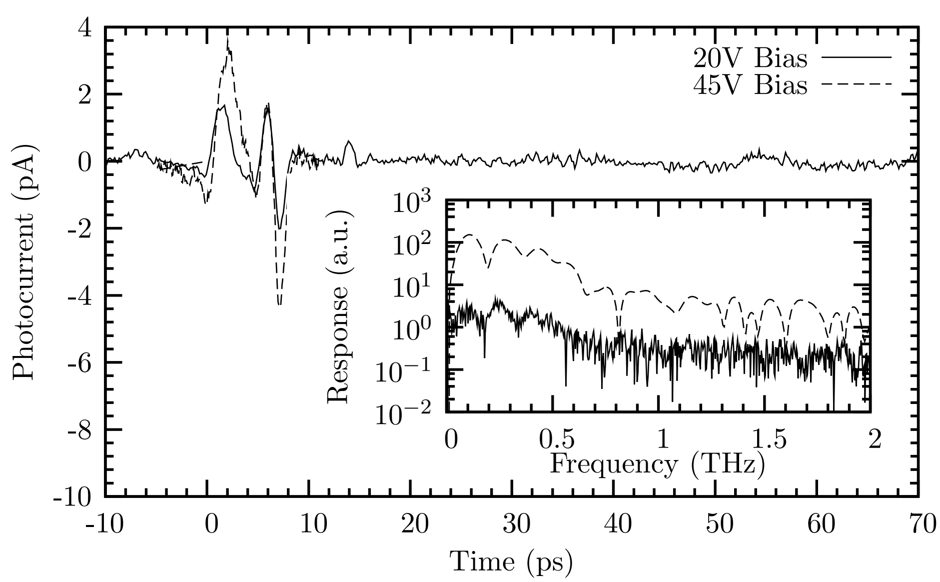

Fig. 8: Measured THz time traces and spectra obtained by Fourier transformation for two different bias voltages driving the emitter.

5. Conclusion

We have successfully established the growth and annealing of LT-GaAs for fast THz photodetectors. The functionality of the fabricated photodetectors has been proven. Further we have successfully implemented an apparatus employing THz-TDS for transmission experiments. The setup is still to be fine-tuned to improve signal-to-noise performance and to enable transmission experiments in highly absorptive samples.

6. Acknowledgements

The authors gratefully acknowledge Michael Riedl for sample growth and Bernd Fischer with the Department of Molecular and Optical Physics, University of Freiburg for discussion and experimental support.

References

[1] H. Rubens and B.W. Snow, “On the refraction of rays of great wavelength in rock salt, sylvine, and fluorite,” *Phil. Mag.*, no. 35, pp. 35–45, 1893.

[2] E.F. Nichols, “A method for energy measurements in the infrared spectrum and the properties of ordinary ray in quartz for waves of great wavelength,” *Phys. Rev.*, vol. 4, pp. 297–313, 1897.

[3] D.H. Auston, “Picosecond photoconduction Hertzian dipoles,” *Appl. Phys. Lett.*, vol. 45, no. 3, pp. 284–286, 1984.

[4] C.E. Shannon, “Communication in the presence of noise,” Proc. *Institute of Radio Engineers*, vol. 37, no. 1, pp. 10–21, 1949.

[5] E.R. Brown, “THz generation by photomixing in ultrafast photoconductors,” *Int. J. High Speed Electron. Sys.*, vol. 13, no. 2, pp. 497–545, 2003.

[6] P.Y. Han, M. Tani, M. Usami, S. Kono, R. Kersting, and X.-C. Zhang, “A direct comparison between terahertz time-domain spectroscopy and far-infrared Fourier transform spectroscopy,” *J. Appl. Phys.*, vol. 89, no. 4, pp. 2357–2359, 2001.

[7] D. Grischkowsky, S. Keiding, M. van Exter, and C. Fattinger, “Far-infrared time-domain spectroscopy with terahertz beams of dielectrics and semiconductors,” *J. Opt. Soc. Am. B*, vol. 7, no. 10, pp. 2006–2015, 1990.

[8] M. van Exter and D. Grischkowsky, “Carrier dynamics of electrons and holes in moderately doped silicon,” *Phys. Rev. B*, vol. 41, no. 17, pp. 12140–12149, 1990.

[9] L. Desplanque, J.F. Lampin, and F. Mollot, “Generation and detection of terahertz pulses using post-process bonding of low-temperature-grown GaAs and AlGaAs,” *Appl. Phys. Lett.*, vol. 84, no. 12, pp. 2049–2051, 2004.

Ph.D. Theses

1. Sven-Silvius Schad,
   Charakterisierung interner optischer Verluste von Leuchtdioden im InGaN-Materialsystem mit Hilfe integrierter Wellenleiter,
   January 2005.

2. Torsten Sven Schaal,
   Kommunikation über Beleuchtungselemente von Kraftfahrzeugen,
   März 2005.

3. Thomas Eduard Kibler,
   Integration von optischen Wellenleitern und optischen Bauelementen in konventionelle und planare Leitungssätze in Kraftfahrzeugen,
   März 2005.

4. Eckart Gerster,
   Optisch gepumpte Halbleiter-Scheibenlaser in den Materialsystemen InGaAs/GaAs und GaAsSb/GaAs,
   September 2005.

5. Manfred Mundbrod-Vangerow,
   Kantenemittierende Halbleiterlaser und Laserverstärker als hochbrillante Strahlquellen,
   December 2005.

6. Christoph Eichler,
   Thermisches Management GaN-basierender Laserdioden,
   December 2005.

Diploma and Master Theses

1. Marwan Bou Sanayeh,
   Fabrication and Characterization of 2-D 850 nm VCSEL Arrays with Built-In Functional Redundancy,
   Master Thesis, Optoelectronics Department, January 2005.

2. Sarad Bahadur Thapa,
   Thermal Improvements to Flip-Chip Bonded 2-D 850 nm VCSEL Arrays for Optical Datacom,
   Master Thesis, Optoelectronics Department, January 2005.

3. Joachim Hertkorn,
   Untersuchungen der Strahlqualität von vertikalemittierenden Laserdioden hoher optischer Ausgangsleistung,
   Diploma Thesis, Optoelectronics Department, July 2005.

4. Manikandan Chandran,
   Processing and Investigation of a Monolithically Integrated Transceiver Module at 850 nm Wavelength,
   Master Thesis, Optoelectronics Department, August 2005.

5. Wolfgang Schwarz,
   Design, Herstellung und Charakterisierung von Terahertz-Emittern,
   Diploma Thesis, Optoelectronics Department, August 2005.

6. Johanna Friederike May,
   Vertical-Cavity Surface-Emitting Laser Diodes as Laser Sources in Optical Tweezers,
   Diploma Thesis, Optoelectronics Department, September 2005.

7. Faisal Nadeem Khan,
   Data Transmission with Fabry-Perot and Distributed Feedback Lasers Operating at 1.3 μm *Wavelength*,
   Master Thesis, Optoelectronics Department, December 2005.

8. Jilwan Giscard,
   Aufbau und Untersuchung eines VCSEL-Transmitters und Photodiode-Receivers für MOST-Systeme im Automotive-Bereich,
   Master Thesis, Optoelectronics Department, 2005.

Semester Projects

1. Christian Fuchs,
   Simulation der optischen Ausgangsleistung
   von Leuchtdioden in Abhängigkeit der Temperatur,
   November 2005.

2. Philipp Karl Gentner,
   Messaufbau für die Charakterisierung
   des Polarisationsverhaltens von VCSELn,
   February 2005.

3. Thomas Gleich,
   Analyse, Vergleich und Verbesserung verschiedener Ansätze
   zum Monitoring von vertikalemittierenden Laserdioden,
   Juni 2005.

4. Kerstin Spöttle,
   Untersuchung von AlGaN/GaN-Übergitterstrukturen,
   September 2005.

5. Alexander Weigl,
   Entwicklung selbstjustierender Prozesse
   zur Herstellung von Vertikallasern mit hoher Packungsdichte,
   November 2005.

Talks

[1] P. Brückner, M. Feneberg, K. Thonke, F. Habel, and F. Scholz, "High quality GaN layers grown on slightly miscut sapphire wafers", *MRS Fall Meeting 2005.* Boston, MA, USA, Dec. 2005.

[2] P. Brückner, M. Feneberg, K. Thonke, F. Habel, and F. Scholz, "Selbstseparation von dicken HVPE-GaN-Schichten", *DGKK-Workshop III-V-Epitaxie*, Duisburg, Germany, Dec. 2005.

[3] P. Gerlach, "Current Research at the Optoelectronics Department, University of Ulm" (in German), *Physikalisches Institut, University of Freiburg*, Freiburg, Germany, Jan. 2005.

[4] P. Gerlach, M. Peschke, T. Knoedl, B.K. Saravanan, C. Hanke, B. Stegmueller, and R. Michalzik, "Complex coupled distributed feedback laser monolithically integrated with electroabsorption modulator at 1.3 µm wavelength", *Conf. on Lasers and Electro-Optics Europe, CLEO/Europe 2005*, Munich, Germany, June 2005.

[5] J. Hertkorn, P. Brückner, K. Spöttle, and F. Scholz, "Laterale Leitfähigkeit der n-Seite bei GaN-Leuchtdioden", *DGKK-Workshop III-V-Epitaxie*, Duisburg, Germany, Dec. 2005.

[6] I. Kardosh, F. Rinaldi, J. Hertkorn, and R. Michalzik. "Beam properties and M^2 measurements of high-power VCSELs", *Semiconductor and Integrated Optoelectronics Conf., SIOE 2005*, Cardiff, Wales, UK, March 2005.

[7] A. Kroner, F. Rinaldi, I. Kardosh, and R. Michalzik, "Towards ultra-compact optical tweezers without external optics", *Conf. on Lasers and Electro-Optics Europe, CLEO/Europe 2005*, Munich, Germany, June 2005.

[8] S. Lorch and P. Unger, "Fabrication, characterization, and applications of optical coatings", *Tyndall National Institute*, Cork, Ireland, April 2005.

[9] R. Michalzik, "High-power semiconductor lasers", *XXV Conf. on Solid State Physics and Materials Science* of the Egyptian Materials Research Society, *Eg-MRS 2005* & Workshop on *Photonic Materials and Optoelectronic Devices (II)*, Luxor, Egypt, March 2005.

[10] R. Michalzik and A. Kroner, "Application scenarios of integrable microlasers in cellular manipulation and sensing", Seminar *Functional Nanoscopy in Life Science*, School of Medicine, University of Ulm, April 2005.

[11] R. Michalzik, "Hot topics in VCSEL research at Ulm University", *Korea Advanced Institute of Science and Technology (KAIST), Department of Physics,* Daejeon, Korea, July 2005.

[12] R. Michalzik, "VCSEL-based optical interconnection work at Ulm University", *Information and Communications University (ICU), School of Engineering,* Daejeon, Korea, July 2005.

[13] R. Michalzik, J.M. Ostermann, M. Riedl, F. Rinaldi, H. Roscher, and M. Stach, "Novel VCSEL designs for optical interconnect applications", *The 10th OptoElectronics and Communications Conf., OECC 2005*, Seoul, Korea, July 2005.

[14] R. Michalzik, "Novel VCSEL designs for optical interconnect technology" (in German), Working Group *Optical Communications* within the Photonics BW Association, Stuttgart, Germany, July 2005.

[15] R. Michalzik, "Vertical-cavity laser diodes: fundamentals and current research topics" (in German), Carl Zeiss, Research and Technology Center, Oberkochen, Germany, Oct. 2005.

[16] R. Michalzik, "Introduction to vertical-cavity microlasers and their use in optical traps", Dept. of Physics, Chonnam National University, Gwangju, Korea, Dec. 2005.

[17] R. Michalzik, "VCSELs for optical interconnection: latest developments", Gwangju Institute of Science and Technology (GIST), Dept. of Information & Communications, Gwangju, Korea, Dec. 2005.

[18] R. Michalzik, M. Stach, H. Roscher, F. Rinaldi, M. Riedl, and J.M. Ostermann, "Advanced short-wavelength vertical-cavity lasers and arrays for optical interconnection", *The Fourth International Conf. on Optical Communications and Networks, ICOCN 2005*, Bangkok, Thailand, Dec. 2005.

[19] B. Neubert, F. Habel, P. Brückner, F. Scholz, M. Schirra, M. Feneberg, K. Thonke, T. Riemann, J. Christen, M. Beer, J. Zweck, G. Moutchnik, and M. Jetter, "Investigations on local Ga and In incorporation of GaInN quantum wells on facets of selectively grown GaN stripes", *International Conference on Nitride Semiconductors ICNS 2005*, Bremen, Germany, Aug./Sept. 2005. Accepted for publication in *phys. stat. sol.* (4 pages).

[20] J.M. Ostermann, "Diffractive optics for polarization control of vertical-cavity surface-emitting lasers," Politecnico di Torino, Seminar of the Electronics Department, Torino, Italy, May 2005.

[21] J.M. Ostermann, "Diffractive optics for polarization control of vertical-cavity surface-emitting lasers", *ETH Zürich, Seminar of the Ultrafast Laser Physics Group*, Zurich, Switzerland, Nov. 2005.

[22] M.C. Riedl, F. Rinaldi, S. Menzel, F. Demaria, E. Gerster, and P. Unger, "Spannungskompensierte Halbleiter-Scheibenlaser", *Deutscher MBE Workshop 2005*, Stuttgart, Germany, Oct. 2005.

[23] F. Rinaldi, J.M. Ostermann, P. Debernardi, and R. Michalzik, "Single-mode and polarisation-stable inverted grating relief VCSELs for 760 nm oxygen sensing", *Semiconductor and Integrated Optoelectronics Conf., SIOE 2005*, Cardiff, Wales, UK, March 2005.

[24] F. Rinaldi, M.C. Riedl, J.M. Ostermann, A. Kroner, and R. Michalzik "Wachstum und Charakterisierung von 760 nm VCSELs", *Deutscher MBE Workshop 2005*, Stuttgart, Germany, Oct. 2005.

[25] H. Roscher and R. Michalzik, "Small pitch flip-chip bonded 850 nm high-speed VCSELs in 2-D arrays with multiple sources per channel", *European Semiconductor Laser Workshop*, Glasgow, Scotland, UK, Sept. 2005.

[26] F. Scholz, "Moderne Halbleiterleuchtdioden für die Automobiltechnik: Herausforderungen und Chancen", *Workshop "Laser, OLEDs, LEDs", Bayerisches Laserzentrum*, Erlangen, Germany, Feb. 2005.

[27] F. Scholz, "Interface related electric fields in semiconductors: basics and device challenges", *Workshop of Graduiertenkolleg "Interfaces in Crystalline Materials" (Uni Stuttgart)*, Irsee, Germany, Oct. 2005.

[28] M. Stach, L. Stöferle, F. Rinaldi, and R. Michalzik, "Monolithically integrated optical transceiver chips at 850 nm wavelength consisting of VCSELs and MSM photodiodes", *Conf. on Lasers and Electro-Optics Europe, CLEO/Europe 2005*, Munich, Germany, June 2005.

[29] S.B. Thapa, C. Kirchner, F. Scholz, D. Hofstetter, A. Minkow, G. Prinz, and K. Thonke, "Structural properties of AlN grown by MOVPE", *DGKK-Workshop III-V-Epitaxie*, Duisburg, Germany, Dec. 2005.

[30] P. Unger, "Halbleiter-Scheibenlaser", Seminar "Faser, Scheibe, Slab", *Bayerisches Laserzentrum*, Erlangen, Germany, April 2005.

[31] P. Unger, "Semiconductor laser with dry-etched mirrors", *III/V Workshop on Dry Etching, Plasma Deposition, Sputtering, MBE, and Ion-Beam Processing*, FIRST Lab and OPT, ETH Zurich, Switzerland, Sept. 2005.

[32] P. Unger, "Semiconductor disk lasers", *Nano Conference, NanoEurope 2005*, St. Gallen, Switzerland, Sept. 2005.

[33] P. Unger, "Optically pumped semiconductor disk lasers", *Sino-German Workshop GZ 313*, "Advances in Diodes and Diode Pumped Lasers", Beijing, China, Sept. 2005.

[34] T. Wunderer, B. Neubert, P. Brückner, and F. Scholz, "Elektrolumineszenz von GaInN-Facetten-Quantenfilmen", *DGKK-Workshop III-V-Epitaxie*, Duisburg, Germany, Dec. 2005.

Publications and Conference Contributions

[1] P. Brückner, F. Habel, and F. Scholz, "HVPE growth of high quality GaN layers", *International Conference on Nitride Semiconductors ICNS 2005.* Bremen, Germany, Aug./Sept. 2005. Accepted for publication in *phys. stat. sol.*, 4 pages.

[2] C. Eichler, S.-S. Schad, F. Scholz, D. Hofstetter, S. Miller, A. Weimar, A. Lell, and V. Härle, "Observation of temperature-independent longitudinal-mode patterns in violet-blue InGaN-based laser diodes", *IEEE Photon. Technol. Lett.,* vol. 17, pp. 1782–1784, 2005.

[3] P. Gerlach, M. Peschke, C. Hanke, B.K. Saravanan, and R. Michalzik, "High-frequency analysis of laser-integrated lumped electroabsorption modulators", *IEE Proc.-Optoelectron.*, vol. 152, pp. 125–130, 2005.

[4] P. Gerlach, M. Peschke, B.K. Saravanan, T. Knoedl, C. Hanke, B. Stegmueller, and R. Michalzik, "40 Gbit/s operation of laser-integrated electroabsorption modulators using identical InGaAlAs quantum wells", in Proc. (CD ROM) *17th Int.'l Conf. on Indium Phosphide and Related Materials, IPRM 05*, 4 pages. Glasgow, UK, May 2005.

[5] P. Gerlach, M. Peschke, T. Knoedl, B.K. Saravanan, C. Hanke, B. Stegmueller, and R. Michalzik, "Complex coupled distributed feedback laser monolithically integrated with electroabsorption modulator at 1.3 μm wavelength", in Proc. (CD ROM) *Conf. on Lasers and Electro-Optics Europe, CLEO/Europe 2005*, paper CB4-3-TUE, one page. Munich, Germany, June 2005.

[6] F. Habel, P. Brückner, J-D. Tsay, W.-Y. Liu, F. Scholz, D. Schmitz, and M. Heuken, "Hydride vapor phase epitaxial growth of thick GaN layers with improved surface flatnes", Proc. *IWN 2004, phys. stat. sol. (c)*, vol. 2, no. 7, pp. 2049–2052, 2005.

[7] I. Kardosh, F. Rinaldi, J. Hertkorn, and R. Michalzik, "Beam properties and M^2 measurements of high-power VCSELs", in Proc. *Semiconductor and Integrated Opto-electronics Conf., SIOE 2005*, paper 33. Cardiff, Wales, UK, March 2005.

[8] C. Kirchner, P. Brückner, F. Scholz, G. Prinz, K. Thonke, and D. Hofstetter, "MOVPE growth of high aluminum containing AlGaN and AlN epitaxial layers", in Extended Abstract Booklet *European Workshop for Metalorganic Vapor Phase Epitaxy, EWMOVPE XI*, pp. 439–441. Lausanne, Switzerland, June 2005.

[9] A. Kroner, F. Rinaldi, I. Kardosh, and R. Michalzik, "Towards ultra-compact optical tweezers without external optics", in Proc. (CD ROM) *Conf. on Lasers and Electro-Optics Europe, CLEO/Europe 2005*, paper CL4-2-FRI, one page. Munich, Germany, June 2005.

[10] R. Michalzik, M. Stach, H. Roscher, F. Rinaldi, M. Riedl, and J.M. Ostermann, "Advanced short-wavelength vertical-cavity lasers and arrays for optical interconnection" (invited), in Proc. *The Fourth International Conf. on Optical Communications and Networks, ICOCN 2005*, pp. 116–119. Bangkok, Thailand, Dec. 2005.

[11] R. Michalzik, J.M. Ostermann, M. Riedl, F. Rinaldi, H. Roscher, and M. Stach, “Novel VCSEL designs for optical interconnect applications” (invited), in Proc. *The 10th OptoElectronics and Communications Conf., OECC 2005*, pp. 328–329. Seoul, Korea, July 2005.

[12] R. Michalzik, “High-power semiconductor lasers” (invited), in Proc. *XXV Conf. on Solid State Physics and Materials Science* of the Egyptian Materials Research Society, *Eg-MRS 2005* & Workshop on *Photonic Materials and Optoelectronic Devices (II)*, pp. 55–56. Luxor, Egypt, March 2005.

[13] B. Neubert, F. Habel, P. Brückner, F. Scholz, T. Riemann, and J. Christen “Electroluminescence from GaInN quantum wells grown on non-(0001) facets of selectively grown GaN stripes” in Proc. *MRS Fall Meeting*. Boston, MA, USA, Dec. 2004; em Mat. Res. Soc. Symp. Proc., vol. 831, pp. E11.32.1–5, 2005.

[14] B. Neubert, F. Habel, P. Brückner, F. Scholz, M. Schirra, M. Feneberg, K. Thonke, J. Christen, T. Riemann, M. Beer, J. Zweck, G. Moutchnik, and M. Jetter, “Characteristics of GaInN quantum wells grown on non-(0001) facets of selectively grown GaN stripes”, in Extended Abstract Booklet *European Workshop for Metalorganic Vapor Phase Epitaxy, EWMOVPE XI*, pp. 375–377. Lausanne, Switzerland, June 2005.

[15] B. Neubert, P. Brückner, F. Habel, F. Scholz, T. Riemann, J. Christen, M. Beer, and J. Zweck, “GaInN quantum wells grown on facets of selectively grown GaN stripes”, *Appl. Phys. Lett.*, vol. 87, pp. 182111-1–3, 2005.

[16] J.M. Ostermann, P. Debernardi, C. Jalics, A. Kroner, M.C. Riedl, and R. Michalzik, “Surface gratings for polarization control of single- and multi-mode oxide-confined vertical-cavity surface-emitting lasers”, *Optics Communications*, vol. 246, pp. 511–519, 2005.

[17] J.M. Ostermann, P. Debernardi, and R. Michalzik, “Shallow surface gratings for high-power VCSELs with one preferred polarization for all modes”, *IEEE Photon. Technol. Lett.*, vol. 17, pp. 1593–1595, 2005.

[18] J.M. Ostermann, P. Debernardi, C. Jalics, and R. Michalzik, “Polarization-stable oxide-confined VCSELs with enhanced single-mode output power via monolithically integrated inverted grating reliefs”, *IEEE J. Select. Topics Quantum Electron.*, vol. 11, pp. 982–989, 2005.

[19] J.M. Ostermann, F. Rinaldi, P. Debernardi, and R. Michalzik, “VCSELs with enhanced single-mode power and stabilized polarization for oxygen sensing”, *IEEE Photon. Technol. Lett.*, vol. 17, pp. 2256–2258, 2005.

[20] J.M. Ostermann, P. Debernardi, and R. Michalzik, “Surface-grating VCSELs with dynamically stable light output polarization”, *IEEE Photon. Technol. Lett.*, vol. 17, pp. 2505–2507, 2005.

[21] J.M. Ostermann, P. Debernardi, C. Jalics, A. Kroner, M.C. Riedl, and R. Michalzik, "Surface gratings for polarization control of single- and multi-mode oxide-confined vertical-cavity surface-emitting lasers", *Optics Communications*, vol. 246, no. 4–6, pp. 511–519, 2005.

[22] F. Rinaldi, J.M. Ostermann, P. Debernardi, and R. Michalzik, "Single-mode and polarisation-stable inverted grating relief VCSELs for 760 nm oxygen sensing", in Proc. *Semiconductor and Integrated Optoelectronics Conf., SIOE 2005*, paper 14. Cardiff, Wales, UK, March 2005.

[23] H. Roscher, M. Bou Sanayeh, S.B. Thapa, and R. Michalzik, "VCSEL arrays with redundant pixel designs for 10 Gbit/s 2-D space-parallel multimode fiber transmission", in Proc. *31st Europ. Conf. on Opt. Commun., ECOC 2005*, vol. 3, pp. 687–688. Glasgow, Scotland, UK, Sept. 2005.

[24] F. Scholz, P. Brückner, F. Habel, M. Peter, and K. Köhler, "Improved GaN layer morphology by hydride vapor phase epitaxy on misoriented Al_2O_3 wafers", *Appl. Phys. Lett.*, vol. 87, pp. 181902-1–3, 2005.

[25] M. Stach, L. Stöferle, F. Rinaldi, and R. Michalzik, "Monolithically integrated optical transceiver chips at 850 nm wavelength consisting of VCSELs and MSM photodiodes" (invited), in Proc. (CD ROM) *Conf. on Lasers and Electro-Optics Europe, CLEO/Europe 2005*, paper CI2-4-THU, one page. Munich, Germany, June 2005.

[26] M. Stach, L. Stöferle, F. Rinaldi, and R. Michalzik, "3 Gbit/s data transmission with monolithically integrated optical transceiver chips for very short reach applications", in Proc. *31st Europ. Conf. on Opt. Commun., ECOC 2005*, vol. 3, pp. 529–530. Glasgow, Scotland, UK, Sept. 2005.

[27] M.A. Artega, M. Valencia, H. Thienpont, K. Panajotov, H. Unold, J. Ostermann, and R. Michalzik, "Study of polarization properties of VCSELs subject to optical feedback from an extremely short external cavity", in Proc. (CD ROM) *Conf. on Lasers and Electro-Optics Europe, CLEO/Europe 2005*, paper CB-18-MON, one page. Munich, Germany, June 2005.

[28] S.-S. Beyertt, T. Kübler, U. Brauch, A. Giesen, E. Gerster, F. Rinaldi, and P. Unger, "Semiconductor thin-disk laser — Comparison of spacer and quantum-well pumping", *20th Anniversary Meeting Advances Solid-State Photonics*. Vienna, Austria, Febr. 2005. Published in *OSA Trends in Optics and Photonics* vol. 98, *Advanced Solid-State Lasers* ed. by C. Denman and I. T. Sorokina (Optical Society of America, Washington, DC 2005), pp. 294–298, 2005.

[29] O. Casel, D. Woll, M.A. Tremont, H. Fuchs, R. Wallenstein, E. Gerster, P. Unger, M. Weyers, and M. Zorn, "Blue 489 nm picosecond pulsed generated by intracavity frequency doubling in a passively mode-locked optically pumped semiconductor disc laser", *Appl. Phys. B*, vol. 81, pp. 443–446, 2005.

[30] P. Debernardi, J.M. Ostermann, M. Feneberg, C. Jalics, and R. Michalzik, "Reliable polarization control of VCSELs through monolithically integrated surface gratings: a comparative theoretical and experimental study", *IEEE J. Select. Topics Quantum Electron.*, vol. 11, pp. 107–116, 2005.

[31] P. Debernardi, J.M. Ostermann, M. Sondermann, G.P. Bava, T. Ackemann, and R. Michalzik, "Dichroism and birefringence in VCSELs with an integrated surface grating", in Proc. *International Workshop on Physics & Applications of Semiconductor Lasers, PHASE 2005*, p. 12. Supélec, Campus de Metz, Metz, France, March 2005.

[32] P. Debernardi, J.M. Ostermann, and R. Michalzik, "Controlling VCSEL polarization by monolithically integrated surface gratings: a survey of modelling and experimental activities" (invited), in Proc. *Second International Conf. on Advanced Optoelectronics and Lasers, CAOL 2005*, pp. 22–30. Yalta, Crimea, Ukraine, Sept. 2005.

[33] M. Feneberg, M. Schirra, K. Thonke, R. Sauer, B. Neubert, P. Brückner, and F. Scholz, "Spatially resolved cathodoluminescence, photoluminescence, electroluminescence, and reflectance study of GaInN quantum wells on non-(0001) GaN facets", *International Conference on Nitride Semiconductors ICNS 2005*. Bremen, Aug./Sept. 2005. Accepted for publication in *phys. stat. sol.*, 6 pages.

[34] S.W.Z. Mahmoud, M.F. Ahmed, and R. Michalzik, "Influence of fiber-facet reflectivity on operation characteristics of vertical-cavity surface-emitting lasers", in Proc. *XXV Conf. on Solid State Physics and Materials Science* of the Egyptian Materials Research Society, *Eg-MRS 2005* & Workshop on *Photonic Materials and Optoelectronic Devices (II)*, p. 151. Luxor, Egypt, March 2005.

[35] E. Richter, Ch. Hennig, M. Weyers, F. Habel, J.-D. Tsay, W.-Y. Liu, P. Brückner, F. Scholz, Yu. Makarov, A. Segal, and J. Kaeppeler, "Reactor and growth process optimization for growth of thick GaN layers on sapphire substrates by HVPE", *J. Crystal Growth*, vol. 277, pp. 6–12, 2005.

[36] U.T. Schwarz, M. Pindl, W. Wegscheider, C. Eichler, F. Scholz, M. Furitsch, A. Leber, S. Miller, A. Lell, and V. Härle, "Near-field and far-field dynamics of AlInGaN laser diodes", *Appl. Phys. Lett.*, vol. 86, pp. 161112-1–3, 2005.

[37] J. Wöllenstein, M. Braun, S. Hartwig, A. Peter, A. Lambrecht, J.M. Ostermann, F. Rinaldi, and R. Michalzik, "Oxygen measurements by using a novel vertical-cavity surface-emitting laser" (in German: "Industrielle Sauerstoffmessung mit einem neuartigen oberflächenemittierenden Laser"), *tm – Technisches Messen*, vol. 72, pp. 440–448, 2005.